isvr Institute of Sound and Vibration Research

The Design of an Adaptive Tuned Vibration Absorber with a Variable Shape Stiffness Element

P.Bonello, M.J. Brennan and S.J. Elliott

ISVR Technical Memorandum No 941

August 2004

University of Southampton

SCIENTIFIC PUBLICATIONS BY THE ISVR

Technical Reports are published to promote timely dissemination of research results by ISVR personnel. This medium permits more detailed presentation than is usually acceptable for scientific journals. Responsibility for both the content and any opinions expressed rests entirely with the author(s).

Technical Memoranda are produced to enable the early or preliminary release of information by ISVR personnel where such release is deemed to the appropriate. Information contained in these memoranda may be incomplete, or form part of a continuing programme; this should be borne in mind when using or quoting from these documents.

Contract Reports are produced to record the results of scientific work carried out for sponsors, under contract. The ISVR treats these reports as confidential to sponsors and does not make them available for general circulation. Individual sponsors may, however, authorize subsequent release of the material.

UNIVERSITY OF SOUTHAMPTON

INSTITUTE OF SOUND AND VIBRATION RESEARCH

DYNAMICS GROUP

The Design of an Adaptive Tuned Vibration Absorber with a Variable Shape Stiffness Element

by

P. Bonello, M.J. Brennan and S.J. Elliott

ISVR Technical Memorandum No: 941

August 2004

Authorised for issue by
Professor M.J. Brennan
Group Chairman

ABSTRACT

A tunable vibration absorber (TVA) with a smart variable stiffness element is capable of retuning itself in response to a time-varying excitation frequency, enabling effective vibration control over a range of frequencies. This report presents research into novel methods of achieving variable stiffness in an adaptive tuned vibration absorber (ATVA) by changing shape. It is shown that considerable variation in the tuned frequency can be achieved by actuating a shape change, provided that this is within the limits of the actuator. A feasible design for such an ATVA is one in which the device offers low resistance to the required shape change actuation while not being restricted to low values of the effective stiffness of the vibration absorber. Three such original designs are identified: (i) A pinned-pinned arch beam with fixed profile of slight curvature and variable preload through an adjustable natural curvature; (ii) A vibration absorber with a variable geometry linkage as stiffness element; (iii) A vibration absorber with a stiffness element formed from parallel curved beams of adjustable curvature vibrating longitudinally. The effectiveness of the latter two designs is limited to frequencies for which inertia effects of the components forming the stiffness element are not significant. The performances of a demonstrator and a prototype ATVA based on designs (ii) and (iii) respectively are analysed and good correlation is achieved between theoretical and experimental results. The tests on the prototype ATVA with piezo-actuated parallel curved beams demonstrate the efficacy of this design in vibration control, particularly with respect to its agility in tracking rapidly varying forcing frequencies.

CONTENTS

1 INTRODUCTION

A tuned or tunable vibration absorber (TVA) is an auxiliary system that is tuned to suppress the vibration at its point of attachment to a host structure. The tuned frequency f_t of the TVA is its undamped natural frequency with its base (point of attachment) blocked. The TVA can be used in two distinct ways [1]:

(i) It can be tuned to suppress ("dampen") the modal contribution to the vibration of a troublesome natural frequency f_n of the host structure over a wide band of excitation frequencies. In this case the TVA is referred to as a "tuned mass damper". f_t is optimally tuned to a value slightly lower than f_n and an optimal level of damping is implemented in the stiffness element of the absorber [1].

(ii) Alternatively, the TVA can be tuned to suppress ("neutralise") the vibration at a troublesome forcing frequency f. In this case the TVA is sometimes referred to as a tuned vibration neutraliser [2], although the generic term "tuned vibration absorber" is often used to refer specifically to this variant of the TVA [1, 2]. The optimal tuning condition is $f_t = f$ and the TVA acts like a notch filter, suppressing the vibration over a very narrow bandwidth centred at the tuned frequency. Total suppression of the vibration at this frequency is achieved when there is no damping in the stiffness element.

Deviation from the tuned condition (mistuning) degrades the performance of either variant of the TVA [1] and it was shown in [3] that a mistuned vibration neutraliser could actually increase the vibration of its host structure. To avoid mistuning, smart or adaptive tunable vibration absorbers (ATVAs) have been developed. Such devices are capable of retuning themselves in real time and an overview of some of these is given in references [1, 4]. Adaptive technology is especially important in the case of the vibration neutraliser since the low damping requirement in the spring element can raise the host structure vibration to dangerous levels in the mistuned condition. In this case, mistuning can occur either due to a drift in the forcing frequency or due to a drift in tuned frequency caused by environmental factors (e.g. temperature change). Hence, a vibration neutraliser needs to be adaptive to have any practical use. This report will focus exclusively on TVAs used as vibration neutralisers.

At the heart of a smart TVA is a stiffness element whose stiffness can be adjusted in real time. To maximise vibration attenuation, the stiffness element should have low structural damping and any mechanism used for stiffness adjustment should add as little as possible to the redundant mass of the device [2, 3]. Of course, the stiffness element should also be tunable over an adequate range of frequencies, and the adjustment should be rapid and with minimum power requirement,

and the device must be cheap and easy to manufacture. The technical challenge is to design a stiffness element with such attributes.

Various designs for variable stiffness elements have been proposed e.g. references [5-8]. Work at the Institute of Sound and Vibration Research (ISVR) has focused on two strategies for achieving variable stiffness. One strategy involves using a shape memory alloy, as in the device developed by Rustighi et al. [9]. The Young's Modulus (and hence stiffness) of a stiffness element made of such an alloy changes with temperature and can therefore be controlled by adjusting the electrical current through it. Such a device is easy to manufacture, requiring no actuating mechanism for stiffness adjustment. The maximum variability of the tuned frequency of such a device is typically found to be around 17.5 % and, for the device in reference [9], it took 2 minutes with a 9A current to achieve this change. Hence, such a device is only suitable for applications where any potential detuning is gradual. The other strategy for stiffness adjustment involves controlling the shape of the stiffness element. One such device is described in reference [4] and is illustrated in Figure 1.1. The mechanism at the centre adjusts the gap between the beams, thereby varying the flexural stiffness. Such a device was built and tested in reference [10] where the mechanism used was a stepper motor driving a screw thread and a maximum adjustment of 35% in tuned frequency was achieved. The response was much more rapid than that obtained in reference [9] although there is room for improvement. Moreover, the mechanism in Figure 1.1 does not form part of the effective mass of the absorber (i.e. it is a redundant mass) thereby degrading the vibration attenuation.

This report presents research into novel methods of achieving variable stiffness by changing shape. Following this introduction, the basic theory concerning the ATVA is presented, together with a study on the feasibility of the shape change concept in such a device. Various novel designs are considered. The performances of a demonstrator and a prototype ATVA based on two of these designs are analysed theoretically and experimentally.

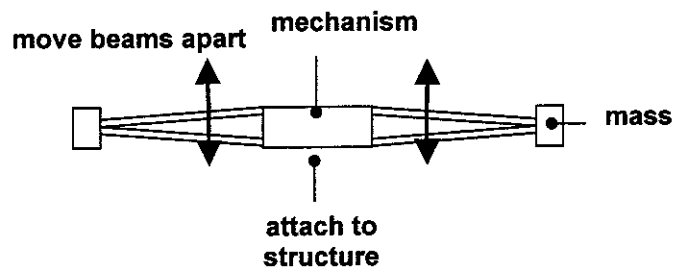

Figure 1.1: Stiffness control of a cantilever ATVA by varying second moment of area [4, 10]

2 FEASIBILITY OF SHAPE CHANGE FOR VARIABLE STIFFNESS

This chapter starts with a summary of elementary theory of the adaptive tuned vibration absorber (ATVA) and goes on to investigate the feasibility of the shape change concept for a variable stiffness ATVA. As mentioned in the Introduction, this report focuses exclusively on ATVAs used as vibration neutralisers.

2.1 Elementary Theory

For excitation frequencies below its first natural frequency as a free body, any auxiliary system used as a tuned vibration absorber (TVA) can always be reduced to an equivalent two degree of freedom system as shown in Figure 2.1(a). When the device is attached to its host structure, only the upper mass is effective (Figure 2.1(b)), the lower mass adds on to that of the host structure. The tuned frequency f_t of the TVA is its undamped natural frequency with its point of attachment to the structure blocked i.e.

$$f_t = \frac{1}{2\pi}\sqrt{\frac{K}{m_e}} \tag{2.1}$$

Optimal tuning is achieved when $f_t = f$ where f is the excitation frequency. In this condition, the TVA exerts a high impedance at its point of attachment, suppressing the vibration there. The vibration attenuation A is defined as the ratio:

$$A = \left|\underline{a}_{1,free}\right| / \left|\underline{a}_1\right| \tag{2.2}$$

where $\left|\underline{a}_1\right|$, $\left|\underline{a}_{1,free}\right|$ are the harmonic vibration amplitudes at the point of attachment respectively with and without the TVA attached. In the tuned condition, $A \to \infty$, i.e. $\left|\underline{a}_1\right| \to 0$, as the damping loss factor in the stiffness element $\eta \to 0$. The tuned condition is conveniently located by noting that $\cos\phi \approx 0$ when $f = f_t$ where ϕ is the phase shift between the harmonic vibrations $a_1(t)$, $a_2(t)$ at the point of attachment and absorber mass respectively. It can be shown [11] that $\cos\phi$ is exactly zero when $f = f_t\sqrt{1+\eta^2}$ and the reduction in attenuation incurred when using the condition $\cos\phi = 0$ for tuning (instead of the condition $f = f_t$) is negligible for $\eta \le 0.5$.

Since the excitation is harmonic, $a_r(t) = \mathrm{Re}\{\underline{a}_r e^{j\omega t}\}$, $r = 1, 2$, and $\cos\phi$ is given by the expression [11]:

$$\cos\phi = \frac{(2/T_c)\int_0^{T_c} a_1(\tau)a_2(\tau)\,d\tau}{\left|\underline{a}_1\right|\left|\underline{a}_2\right|} \tag{2.3}$$

where $T_c = k2\pi/\omega$ (k any positive integer). Since the amplitudes

$$|\underline{a}_r| = \left(\sqrt{2}/T_c\right)\int_0^{T_c} a_r^2(\tau)\,d\tau\,, \quad r = 1, 2 \tag{2.4}$$

$\cos\phi$ can be expressed in terms of a_1, a_2 as

$$\cos\phi = \frac{\int_0^{T_c} a_1(\tau)a_2(\tau)\,d\tau}{\int_0^{T_c} a_1^2(\tau)\,d\tau \int_0^{T_c} a_2^2(\tau)\,d\tau} \tag{2.5}$$

If it is assumed that the host structure is mass-like (e.g. a rigid machine on soft isolators), then the variation of attenuation with frequency is typically as shown in Figure 2.2 and the attenuation at the tuned condition is [3]

$$A = \mu/\eta \tag{2.6}$$

where $\mu = m_e/M$ is the ratio of effective absorber mass to host structure mass. Figure 2.2 shows how a mistuned TVA can increase the vibration of its host structure as a result of the additional natural frequency it introduces into the system.

A smart or adaptive tuned vibration absorber (ATVA) having adjustable stiffness is capable of tracking changes in f or f_t and adjusting its stiffness in real time so as to maintain the tuned condition (see Figure 2.3). The error signal e whose magnitude is to be minimised is $\cos\phi$. In order to take into account the variation of $\cos\phi$ with time, equation (2.5) is modified thus:

$$e(t) = \cos\phi(t) = \frac{\int_{t-T_c}^{t} a_1(\tau)a_2(\tau)\,d\tau}{\int_{t-T_c}^{t} a_1^2(\tau)\,d\tau \int_{t-T_c}^{t} a_2^2(\tau)\,d\tau}, \quad t \geq T_c \tag{2.7}$$

where T_c is a fixed interval covering several periods of the lowest excitation frequency.

2.2 Shape Change for Variable Stiffness

The aim of this section is to consider some designs for ATVAs using the shape control concept and to discuss how this could be realised.

2.2.1 Shallow pinned arch in lateral vibration

Consider the shallow arch of homogeneous material with boundary conditions as shown in Figure 2.4(a) where K_S is the stiffness of the longitudinal end restraints. The system is shown unstressed in Figure 2.4(a) and the beam profile is given by

$$w_i = H\sin(\pi x/L) \tag{2.8}$$

In Figure 2.4(b) the beam is preloaded with an axial load P_0 ($P_0 > 0$ for compression). Since the beam is pivoted at its ends, it is reasonably assumed that the entire deformation is due to bending i.e. there is negligible strain along the beam neutral surface. The deformed profile is then given by [12]:

$$w_{P_0} = H_{P_0} \sin(\pi x/L) \tag{2.9}$$

where

$$H_{P_0} = H/(1 - P_0/P_{EL}) \tag{2.10}$$

and

$$P_{EL} = \pi^2 EI/L^2 \tag{2.11}$$

is the Euler critical load. Eqs. (2.9), (2.10) and the subsequent analysis assumes the arch is shallow i.e.

$$(w_i')^2, (w_{P_0}')^2 << 1 \tag{2.12}$$

where $(\ )' = d(\ )/dx$. For small vibrations v about the preloaded configuration $w = w_{P_0}(x)$ (Figure 2.4(c)), the neutral surface of the beam is strained by an amount depending on the stiffness K_S of the longitudinal end restraints. In Appendix 1 it is shown that, for vibrations symmetrical about the mid-section, the equation of motion is given by:

$$EIv^{iv} + v''P_0 - w_{P_0}'' \frac{\int_0^L w_{P_0}' v' dx}{2\{1/(2K_B) + 1/K_S\}} + \gamma \ddot{v} = 0 \tag{2.13}$$

where E, I, A, γ are the Young modulus, second moment of area of cross-section about neutral axis, cross-sectional area, and mass per unit length respectively of the curved beam and $K_B = EA/L$ is the axial stiffness of the straightened beam. Eq. (2.13) neglects inertia effects in the longitudinal direction. This equation is a generalisation of the case considered in [13] of a pinned-pinned shallow arch with full end longitudinal restraint and no preload. In that work it was shown that the longitudinal inertia was negligible by an order of magnitude consideration. Eq. (2.13) also applies for vibration that is not symmetric about the mid-section, provided that $K_S = \infty$. If vibration in the first symmetric mode is considered, the mode shape is given approximately by

$$v = C \sin(\pi x/L) \sin \omega_1 t \tag{2.14}$$

Substituting eqs. (2.14) and (2.9) in eq. (2.13) yields the fundamental frequency of the first symmetric mode of vibration:

$$\omega_1^2 = \omega_s^2 \left[1 - \frac{P_0}{P_{EL}} + \frac{1}{2} \left(\frac{H_{P_0}}{r} \right)^2 \Big/ \{1 + 2K_B/K_S\} \right] \tag{2.15}$$

where ω_s rad/s is the fundamental frequency of lateral vibrations of the straightened beam:

$$\omega_s = (\pi/L)^2 \sqrt{(EI/\gamma)} \tag{2.16}$$

and r is the radius of gyration of cross-section about the neutral axis. All examples in this section refer to a rectangular section of thickness $2h$ for which $r = h/\sqrt{3}$.

For $H_{P_0} = 0$, eq. (2.15) reduces to

$$\omega_1^2\big|_{H_{P_0}=0} = \omega_s^2\left[1 - P_0/P_{EL}\right] \tag{2.17}$$

which is the expression for the fundamental frequency of a straight beam under a compressive load P_0, given in reference [14], for which ω_1 decreases with compression ($0 < P_0 < P_{EL}$) and increases with tension ($P_0 < 0$).

For $P_0 = 0$, $H_{P_0} = H$ and eq. (2.15) reduces to:

$$\omega_1^2\big|_{P_0=0} = \omega_s^2\left[1 + \frac{1}{2}\left(\frac{H}{r}\right)^2 \Big/ \{1 + 2K_B/K_S\}\right] \tag{2.18}$$

It is noted from eq. (2.18) that, if $K_S = 0$ (no end longitudinal restraint):

$$\omega_1^2\big|_{P_0=0,\,K_S=0} \approx \omega_s^2 \tag{2.19}$$

i.e. the dependency of ω_1^2 on curvature disappears. If $K_S = \infty$ (full end longitudinal restraint), eq. (2.18) reduces to

$$\omega_1^2\big|_{P_0=0,\,K_S\to\infty} = \omega_s^2\left[1 + \frac{1}{2}\left(\frac{H}{r}\right)^2\right] \tag{2.20}$$

which agrees with the expression derived in [13] for the first symmetrical mode of a pinned-pinned shallow arch with full end restraint and no preload. Figure 2.5 shows the percentage increase in ω_1 with curvature under such conditions for a rectangular section beam of thickness $2h$. In Figure 2.5, the theoretical result given by eq. (2.20) is compared with the result obtained by Finite Element (FE) analysis of the arch using shell elements (ANSYS® with SHELL 93 elements [15]). For the FE analysis, the Young modulus and density of the material are 70GPa and 2700kg/m^3 respectively, $2h = 0.75\times10^{-3}$m, the width (normal to plane of paper) is 15mm, and $L = 0.15$m. It is seen that excellent agreement exists up to at least $H/h = 3.5$. Since $w_{P_0} = w_i = H\sin\pi x/L$, the integral term in eq. (2.13) vanishes for the first anti-symmetric mode, as noted in [13]. Hence, this mode's natural frequency is unaffected by curvature, remaining equal to $4\omega_s$ rad/s. From eq. (2.20), the

first symmetric mode is then seen to overtake the first anti-symmetric mode when $H/r = \sqrt{30}$ i.e. $H/h = \sqrt{10} \approx 3.16$ for a rectangular section [13].

While the variation of frequency with curvature in eq. (2.20) has been shown to be considerable, it has little practical use for an adaptive tuned vibration absorber since it applies only for $P_0 = 0$ and it would be impossible to adjust the curvature H of the pinned-pinned beam in real time without loading it axially. The effect of the preload will henceforth be considered.

Substituting for $1 - P_0/P_{EL}$ from eq. (2.10) into eq. (2.15) gives the equation governing the tuned frequency of a potential TVA consisting of a preloaded pinned shallow arch:

$$\omega_t^2 = \omega_s^2 \left[\frac{H}{H_{P_0}} + \frac{1}{2}\left(\frac{H_{P_0}}{r} \right)^2 \Big/ \{1 + 2K_B/K_S\} \right] \tag{2.21}$$

where H_{P_0}, H are the crown heights with and without preloads respectively. Eq. (2.21) gives two methods for varying ω_t in the ATVA: (a) for fixed H, vary H_{P_0}; (b) for fixed H_{P_0}, vary H. In either of these cases it is preferable to have full longitudinal end restraint in vibration ($K_S = \infty$) so that the relevant equation to consider is:

$$\omega_t^2 = \omega_s^2 \left[\frac{H}{H_{P_0}} + \frac{1}{2}\left(\frac{H_{P_0}}{r} \right)^2 \right] \tag{2.22}$$

It is assumed that the vibration of the TVA is symmetrical about the mid-section of the arch. However, in practice, due to inherent slight asymmetry in conditions, an anti-symmetric mode of vibration will also be excited, becoming significant when the frequency given by eq. (2.22) catches up with the frequency ω_2 rad/s of the first anti-symmetric mode of the pinned-pinned beam. In this case the TVA will not reduce to the simple model of Figure 2.1 and will cease to function effectively. By substituting $v = C\sin(2\pi x/L)\sin\omega_2 t$ in eq. (2.13) with $K_S = \infty$, along with the expression for the deformed profile about which vibration occurs (eq. (2.9)), it is seen that:

$$\omega_2^2 = \omega_s^2 (16 - 4P_0/P_{EL}) = \omega_s^2 (12 + 4H/H_{P_0}) \tag{2.23}$$

(by substituting for P_0/P_{EL} from eq. (2.10)). The condition $\omega_t^2 < \omega_2^2$ limits the variation of H and H_{P_0} in the ATVA since, from eqs. (2.22) and (2.23):

$$(H_{P_0}/r)^3 - 24(H_{P_0}/r) - 6(H/r) < 0 \quad \text{for} \quad \omega_t^2 < \omega_2^2 \tag{2.24}$$

The methods (a) and (b) for varying ω_t are now considered in turn.

(a) ***Changing deformed shape*** – For a given natural (undeformed) curvature (fixed H) vary H_{P_0} by moving end supports inwards or outwards (Figure 2.6(a)). In this case, a finite stiffness K_S in eq.

(2.21) would reduce the variability in ω_t. Hence, full longitudinal restraint in vibration is required. An example of an actuator that fulfils this requirement is a motor driven screw. Figure 2.7(a) shows the variation obtained in ω_t with variation in H_{P_0}/h for three different values of the undeformed condition H/h. Figure 2.7(b) shows the corresponding force requirement of the actuator. The *upper* limit on H_{P_0}/h for a range of H/h (see eq. (2.24)) is given by the solid line in Figure 2.7(c). The dashed line in Figure 2.7(c) defines the undeformed condition and intersects with the solid line at $H_{P_0}/h = H/h = \sqrt{10}$, which was the limiting condition for the no-preload case considered earlier. Figures 2.7 show that while considerable variability in ω_t is possible, considerable amount of force is required of the actuator due to the high longitudinal (span-wise) stiffness of the curved beam. Moreover, the actuator will be a redundant mass that degrades the vibration attenuation. It is also evident from Figure 2.7(c) that there are problems of anti-symmetric mode interference.

(b) ***Changing natural curvature*** – For a given curvature about which vibration occurs (fixed H_{P_0}), vary the undeformed curvature (vary H). This can be achieved in practice by bonding a layer of piezo-ceramic (Figure 2.6(b)) and applying different levels of voltage to the piezo. If there is full longitudinal end restraint ($K_S = \infty$), H_{P_0} will remain approximately the same but the preload P_0 will be altered, thereby adjusting the tuned frequency. It is understood that a piezo-actuated beam is composite, however it is reasonably assumed that the above equations, developed for a homogeneous section, give a fair description of the behaviour of the practical application. Figure 2.8(a) shows the variation obtained in ω_t with variation in H/h for three different values of the deformed condition H_{P_0}/h, and Figure 2.8(b) shows the corresponding variation in preload. The *lower* limit on H/h over a range of H_{P_0}/h (see eq. (2.24)) is given by the solid line in Figure 2.8(c), where the dashed line represents the undeformed condition and intersects with the solid one at $H_{P_0}/h = H/h = \sqrt{10}$ as before. It is seen from Figure 2.8(a) that this technique works very well for slight curvatures H_{P_0}/h. Moreover, for such slight curvatures, there are no limits on the variation of H/h, as far as anti-symmetric mode interference is concerned, since the lower limit on H/h is negative in Figure 2.8(c). Unlike the technique in the previous method (a), the preload P_0 is provided by the support reaction i.e. the actuation has been uncoupled from the high longitudinal (span-wise) stiffness of the beam. Moreover, the actuation would be incorporated into the beam making the design simple, cheap and efficient.

2.2.2 Anticlastic curvature control

Another design considered was a cantilever beam vibration neutraliser whose tuned frequency was to be controlled by varying the curvature of its cross-section, thereby varying its flexural rigidity (see Figure 2.9). With reference to Figure 2.9(b), which shows the cross-section of a composite cantilever beam, assuming that the cross-section geometry does not vary significantly due to the vibration, the fractional increase in tuned frequency from the flat cross-section condition (subtended angle $\alpha = 0$) is estimated as

$$\frac{f_t - f_t|_{\alpha=0}}{f_t|_{\alpha=0}} = \sqrt{\frac{I}{I|_{\alpha=0}}} - 1 \tag{2.25}$$

where I is the equivalent second moment of area of the composite section about the neutral axis G*G* [12]:

$$I = (I_{G^*G^*})_1 + C(I_{G^*G^*})_2 \tag{2.26}$$

$$(I_{G^*G^*})_1 = (Sh^3/8)\left[U^3F_1 + UF_2 + U^{-1}F_3 + U^{-1}(1-D)^2F_4\right] \tag{2.27a}$$

$$(I_{G^*G^*})_2 = (Sh^3/8)\left[V^3F_1 + VF_2 + V^{-1}F_3 + V^{-1}(1+D)^2F_4\right] \tag{2.27b}$$

$$C = E_2/E_1, \quad D = (1-C)/(1+C) \tag{2.28a,b}$$

$$F_1 = (1/2)(h/S)\left[\alpha + \sin\alpha - (8/\alpha)\sin^2(\alpha/2)\right] \tag{2.29a}$$

$$F_2 = (1/2)(h/S)\left[\alpha + \sin\alpha - (16/3)(1/\alpha)\sin^2(\alpha/2)\right], \quad F_3 = -(4/9)(h/S)(1/\alpha)\sin^2(\alpha/2) \tag{2.29b,c}$$

$$F_4 = (128/9)(h/S)(1/\alpha)\left[\frac{9}{\alpha^4}\left(\frac{S}{h}\right)^4 - \frac{6}{\alpha^2}\left(\frac{S}{h}\right)^2 + 1\right]\left[\frac{2}{\alpha}\left(\frac{S}{h}\right) - D\right]^{-2}\sin^2(\alpha/2) \tag{2.29d}$$

$$U = (2/\alpha)(S/h) - 1, \quad V = (2/\alpha)(S/h) + 1 \tag{2.29e,f}$$

$$I|_{\alpha=0} = \frac{S|_{\alpha=0}h^3}{24}\left[2(1+C) + 6(1-D)^2 + 6C(1+D)^2\right] \tag{2.30}$$

$(I_{G^*G^*})_1$, $(I_{G^*G^*})_2$ are second moments of area of the individual layer cross-sections about the neutral axis G*G* and the derivation of their expressions in eqs. (2.27a,b) is given in Appendix 2. Eq. (2.30), can be derived using elementary theory e.g. [12].

Three methods of changing the cross-section curvature that were considered are:

(a) Temperature change – as in a bimetallic strip. While considerable changes of curvature can be achieved in this way, the response time would be too long for many applications.

(b) Using the stretch-bend effect of cross-ply laminates [16] - with reference to Figure 2.10, if the cross-section is a cross-ply laminate consisting of two orthotropic layers of the same composite material that are oriented such that their fibres are at 90° to each other, then a

tensile force N_x per unit length along an edge will produce curvature K_x in a plane normal to the edge according to the equations:

$$\begin{bmatrix} N_x \\ N_y \end{bmatrix} = \begin{bmatrix} A_{11} & A_{12} \\ A_{12} & A_{22} \end{bmatrix} \begin{bmatrix} \varepsilon_{0x} \\ \varepsilon_{0y} \end{bmatrix} + \begin{bmatrix} B_{11} & 0 \\ 0 & B_{22} \end{bmatrix} \begin{bmatrix} K_x \\ K_y \end{bmatrix} \qquad \begin{bmatrix} M_x \\ M_y \end{bmatrix} = \begin{bmatrix} B_{11} & 0 \\ 0 & B_{22} \end{bmatrix} \begin{bmatrix} \varepsilon_{0x} \\ \varepsilon_{0y} \end{bmatrix} + \begin{bmatrix} D_{11} & D_{12} \\ D_{12} & D_{22} \end{bmatrix} \begin{bmatrix} K_x \\ K_y \end{bmatrix} \tag{2.31a,b}$$

where the axes x and y are aligned with the axes of symmetry of material properties, ε_{0x}, ε_{0y} are the longitudinal strains in the mid-surface and K_x, K_y the curvatures and the matrix terms are defined in reference [16]. It is shown in [16] that the coupling coefficients between stretching and bending are maximum for given material properties when the two layers are of equal thickness h.

(c) Using piezoactuation.

Consider, as an example, approach (b) applied to a composite section cantilever (Figure 2.9) with section 2 mm × 50 mm, length $2L = 0.24$ m, density $\rho = 1600$ kg/m^3 and orthotropic material properties E_1, $E_2 = 130, 10$ GPa (Young Moduli), $\upsilon_{12} = 0.3$ (Poisson ratio [16]). Figure 2.11 shows the percentage increase in tuned frequency from the flat section condition, computed using eq. (2.25). The solid line assumes S to be invariant, while the dashed line takes into account the deformation of S. The main assumption with eq. (2.25) is that the cross-section geometry is taken to be invariant during vibration. This assumption was tested using FE analysis with shell elements (ANSYS® with SHELL 99 layered composite shell elements [15]), in which the beam mid-section was constrained only at its point of attachment A to the structure (see Figure 2.9(a)) (zero displacements and rotations at A). The analytical estimates of 99.4, 193.3 Hz compare favourably with the FE estimates 99.5, 183.5 Hz. Figure 2.11 shows that significant changes in tuned frequency are possible, provided that the actuator can provide the necessary changes to the subtended angle α. Figure 2.12 shows the tension force requirement, computed by eq. (2.31) and verified at two points by FE. The slope of the graph in Figure 2.12 is seen to be enormous, indicating that this is not a practical way of varying the cross-section. It is also seen in the following section that piezoactuation cannot yield the curvature changes required for this application.

The main drawback with the design in Figure 2.9 is that the curvature changes required are very high since significant variations in the subtended angle α are required over a short length S (the curvature $K = \alpha / S$), making the actuator force or moment requirement beyond practical limits. Indeed, the only way of achieving such curvatures would be by using temperature effects ((a) above).

Hence, for the above reasons the concept of anticlastic curvature control for variable stiffness in Figure 2.9 was not pursued any further.

2.2.3 Effective TVA designs

In previous sections it was shown that, while considerable variation in tuning frequency can be achieved by actuating a shape change, this will be limited by the maximum force that can be provided by the actuator. A feasible design for a TVA is one in which the device offers low resistance to the required shape change actuation. Of course, this should not restrict the device to low values of TVA effective stiffness (i.e. the stiffness of the equivalent model in Figure 2.1). Hence, the best designs are those in which the actuator force is uncoupled as much as possible from the effective stiffness of the TVA. For example, the device in Figure 2.6(b) is effective since, although the effective stiffness of the TVA can be considerably high, this stiffness is controlled by merely altering the natural (undeformed) shape, which is equivalent to the piezo-actuator acting against the relatively low flexural stiffness of a free-free beam. Two other designs that are similarly effective are shown in Figures 2.13(a,b). In Figure 2.13(a) the effective stiffness of the device is controlled by adjusting the distance between the cantilevers and the (hinged) linkage stiffness element offers no resistance to this adjustment. In Figure 2.13(b) the effective stiffness of the device is controlled by changing the curvature of the beams. While the controlled stiffness can be quite high, the curvature of each beam is relatively easy to adjust by flexure since it is pivoted at the ends and one end is free to move. It should be noted that in eq. (2.19) it was shown that the natural frequency of lateral vibrations of a curved beam would be insensitive to curvature if there are no longitudinal end restraints. However, its static stiffness in the longitudinal ("span-wise") direction does alter with curvature, and the addition of significant longitudinal inertia (in the form of the absorber mass in Figure 2.13(b)) would clearly make the modal parameters of the resulting system sensitive to curvature.

2.2.4 Methods of changing curvature

This section discusses the use of composites and piezoactuators for curvature change.

2.2.4.1 *Composites*

One way of implementing the stretch-bend effect in composites is to use hydraulic pressure to generate the required tension force along the edge. Figure 2.14 shows an initially straight clamped-free beam in which the upper and lower surfaces are orthotropic laminae of the same composite material and are oriented such that their fibres are at 90° to each other. The two laminae are separated by a fluid filled cavity. Fibre reinforcements joining the upper and lower surfaces prevent them from bulging. Figure 2.14 shows the FE model of the deformation resulting from the

application of a 1 bar pressure. For the dimensions shown, and a Poisson ratio $\upsilon_{12} = 0.3$, the tip deflections are 0.13mm, 0.145mm, 0.274mm respectively for major and minor Young Moduli (E_1, E_2) of $(130\,\text{GPa}, 10\,\text{GPa})$, $(10\,\text{GPa}, 5\,\text{GPa})$, $(100\,\text{GPa}, 5\,\text{GPa})$.

The beam in Figure 2.14 is somewhat analogous to the stem of a plant [17]. As in the present case, the turgor pressure was uniform throughout the stem but the bending of the stem was due to the variation of cell wall thickness along the cross-section radius resulting in differential cell wall expansion.

2.2.4.2 *Piezo-actuation*

A piezo-actuator bends a beam to which it is bonded by applying a moment. The piezo-patch(es) can be placed on both parallel surfaces of the beam with opposing polarities or one surface only. With one-sided piezo-actuation there is a tensile force on the beam mid-surface as well. Hence, it is worthwhile investigating whether the use of a composite beam with a piezo-actuator on one surface would have any advantage with respect to curvature generation.

If ε_p is the longitudinal expansion coefficient ("free strain") of the actuator under a voltage V:

$$\varepsilon_p = d_{31} V / t_a \tag{2.32}$$

where d_{31} is the piezo-electric constant [18]. With reference to Figure 2.15, following an analysis broadly similar to that in [18], it can be shown that the piezo will cause the initially straight beam to bend to a radius R (measured from the beam mid-surface), with the ratio r of non-dimensional curvature to actuator free strain ratio being given by:

$$r = \frac{h/R}{\varepsilon_P} = \frac{-6B(1+6C+9C^2)\psi^2 - 6B(1+C)(1+3C)\psi^2 T + 6B^2(1+C)\psi T^2 + 6B^2(1+3C)\psi T}{[(1+3C)\psi - BT]\left[(1+14C+C^2)\psi^2 + 4B(1+C)T^2\psi + 6B(1+3C)T\psi + 4B(1+7C)\psi + B^2T^2\right]} \tag{2.33}$$

where

$$B = E_a/E_1\,,\; C = E_2/E_1\,,\; T = t_a/h\,,\; \psi = b_b h/(b_a t_a) \tag{2.34a-d}$$

and b_b, b_s are the beam and actuator widths normal to plane of paper. The formula applies for a composite beam with two layers of equal thickness h. This was done to simplify the analysis. Moreover, it was thought that the use of equal layer thickness might maximise the stretch-bend effect induced by the piezo, as in a cross-ply laminate with two equal thickness layers under tension, although it is understood that the present case is different due to the addition of the extra layer due to the piezo. Figure 2.16 shows the variation of $|r|$ with $T/2$ for $b_a = b_b$ and various C

for PZT material with $E_a = 59.5\,\text{GPa}$ and $d_{31} = 212\times10^{-12}\,\text{V/m}$ [19]. From Figure 2.16 it appears that there is some advantage in using a composite beam with the piezo-actuator. The curves in Figure 2.16 show that there is normally optimum value of T, T_{opt}, which minimises the electric field requirement for a given curvature in a beam of given geometry. Hence, there is the possibility of choosing the materials of a composite beam to reduce this value of T_{opt}. Substituting $r = r(T_{opt})$, $t_a = T_{opt}h$ and $1/R = \alpha/S$ in eqs. (2.32) and (2.33) and eliminating ε_p gives the minimum voltage required to generate a subtended angle of α by piezo actuation in a beam of given thickness $2h$ and length S:

$$V_{\min} = \frac{T_{opt}}{r(T_{opt})}\frac{h^2\alpha}{d_{31}S} \tag{2.35}$$

Figure 2.17 show $V_{\min}$ *vs* α characteristics for $S = 0.05\,\text{m}$ and $2h = 0.5\times10^{-3}\,\text{m}$ and various material properties. It is again evident that high voltages are necessary to actuate significant changes to the subtended angle α over a short length S (very high curvature requirement), making piezo-actuation not feasible for anticlastic curvature control (section 2.2.2, Figure 2.9). However, piezo-actuation is extremely useful for those designs of ATVA where the curvature variation requirement is low to moderately high, as in the proposed designs of Figure 2.6(b) and Figure 2.13(b).

2.3 Conclusions

The basic theory of the adaptive tuned vibration absorber (ATVA) has been presented, together with a study of the feasibility of the shape change concept for use in a variable stiffness ATVA. The latter study consisted of an analysis of the dynamics of the lateral vibrations of a preloaded pinned shallow arch beam, the dynamics of a cantilever beam with anticlastic curvature control for variable stiffness, and a discussion on the use of composites and piezo-actuators to achieve shape change. It is concluded that considerable variation in the tuned frequency can be achieved by actuating a shape change, provided that this is within the limits of the actuator. A feasible design for such an ATVA is one in which the device offers low resistance to the required shape change actuation while not being restricted to low values of the effective stiffness of the vibration absorber. Hence, the best designs are those in which the actuator force is uncoupled as much as possible from the effective stiffness of the absorber. Three such designs have been identified: (i) A pinned-pinned arch beam with fixed profile of slight curvature and variable preload through an adjustable natural curvature; (ii) A vibration absorber with a variable geometry linkage as stiffness element; (iii) A vibration absorber with a stiffness element formed from curved beams of adjustable curvature in

parallel vibrating longitudinally. The latter two designs are considered in greater detail in the subsequent chapters.

Figures

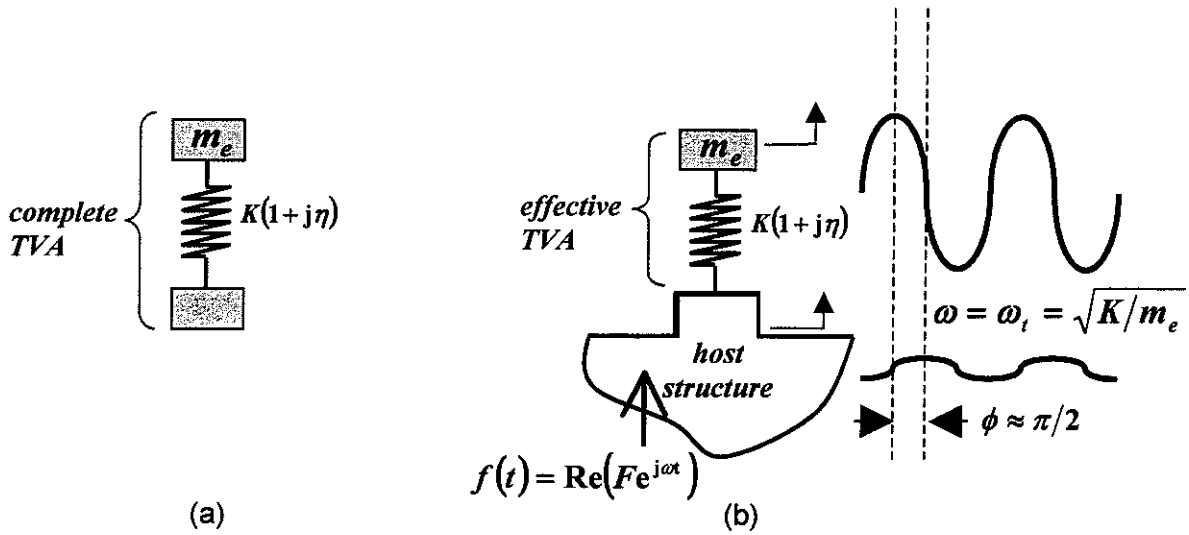

Figure 2.1: Tuned vibration absorber used as a vibration neutraliser

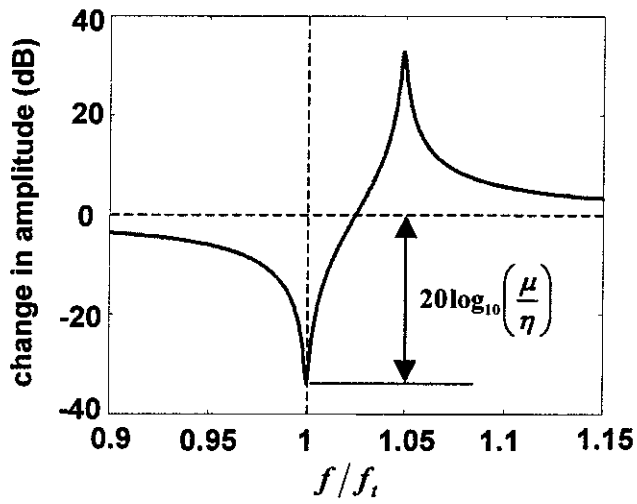

Figure 2.2: Change in amplitude ($|\underline{a}_1|/|\underline{a}_{1,free}|$) for $\mu = 0.1$ and $\eta = 0.005$

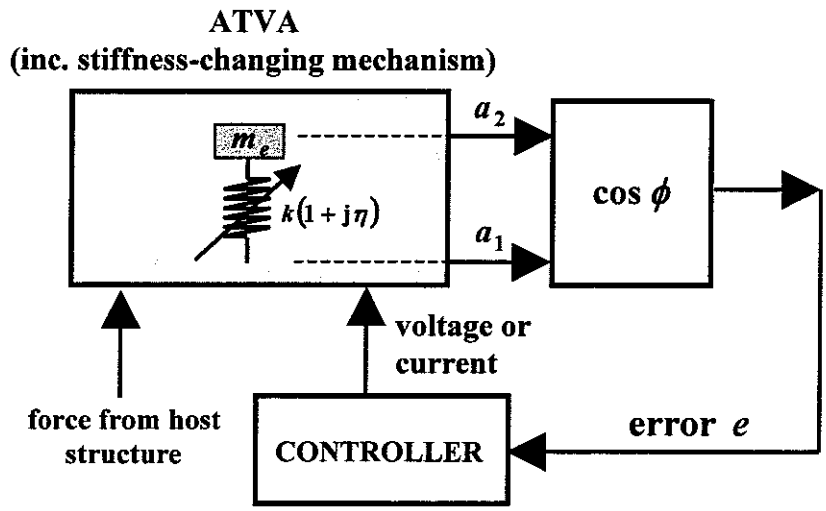

Figure 2.3: Schematic of a generic ATVA with control system

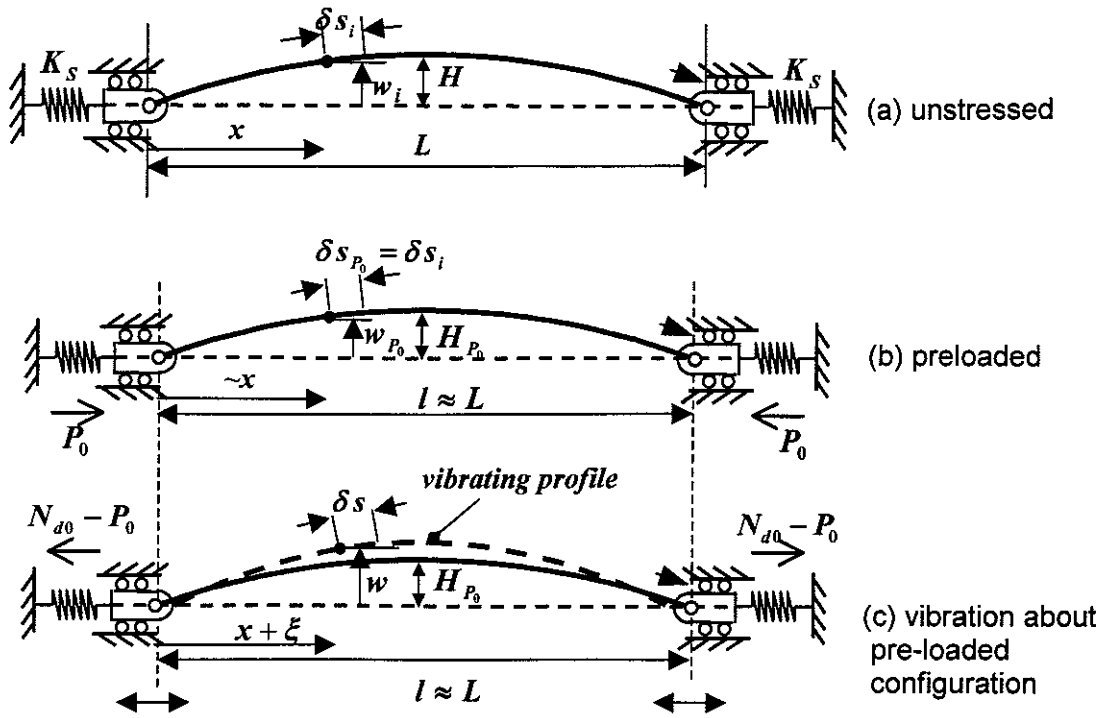

Figure 2.4: Dynamics of pinned shallow arch with end longitudinal restraints of finite stiffness

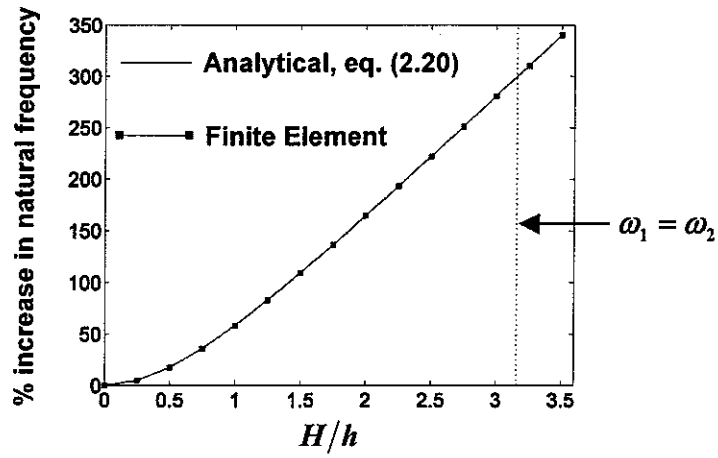

Figure 2.5: Variation of natural frequency with curvature of a shallow pinned arch of rectangular section $2h$ with no preload and $K_S = \infty$.

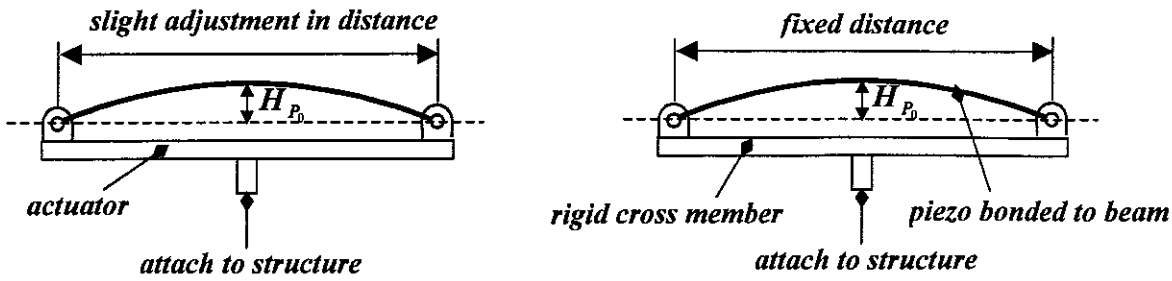

(a) fixed H, variable H_{P_0} (b) fixed H_{P_0}, variable H

Figure 2.6: Two alternative designs for a shallow arch ATVA

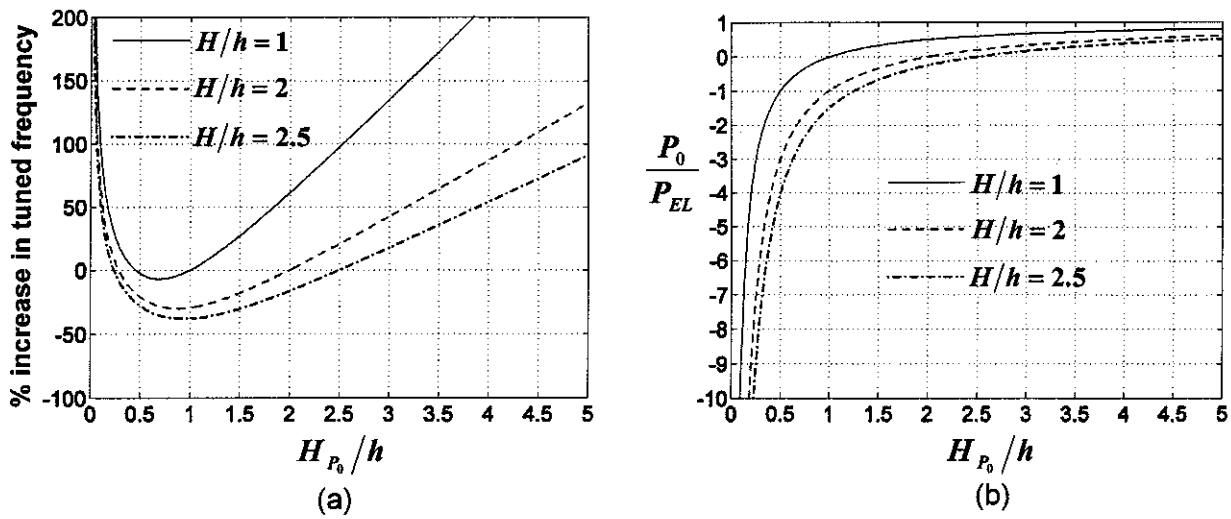

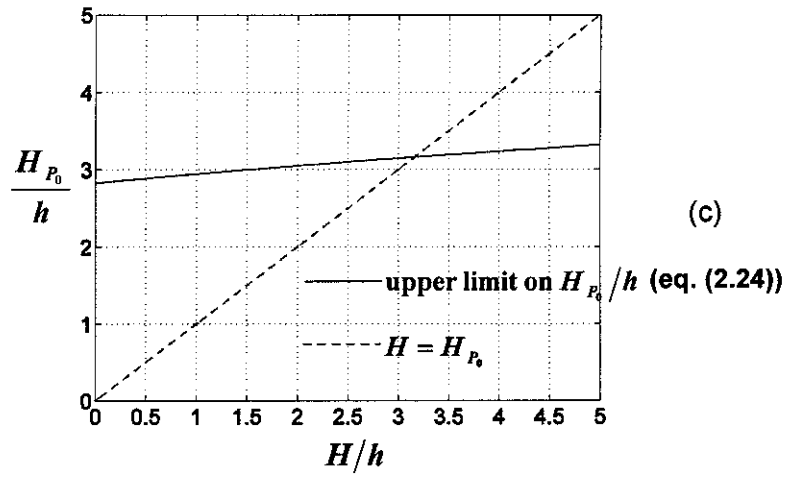

Figure 2.7: Performance curves for shallow arch ATVA with fixed H, variable H_{P_0} (Figure 2.6(a))

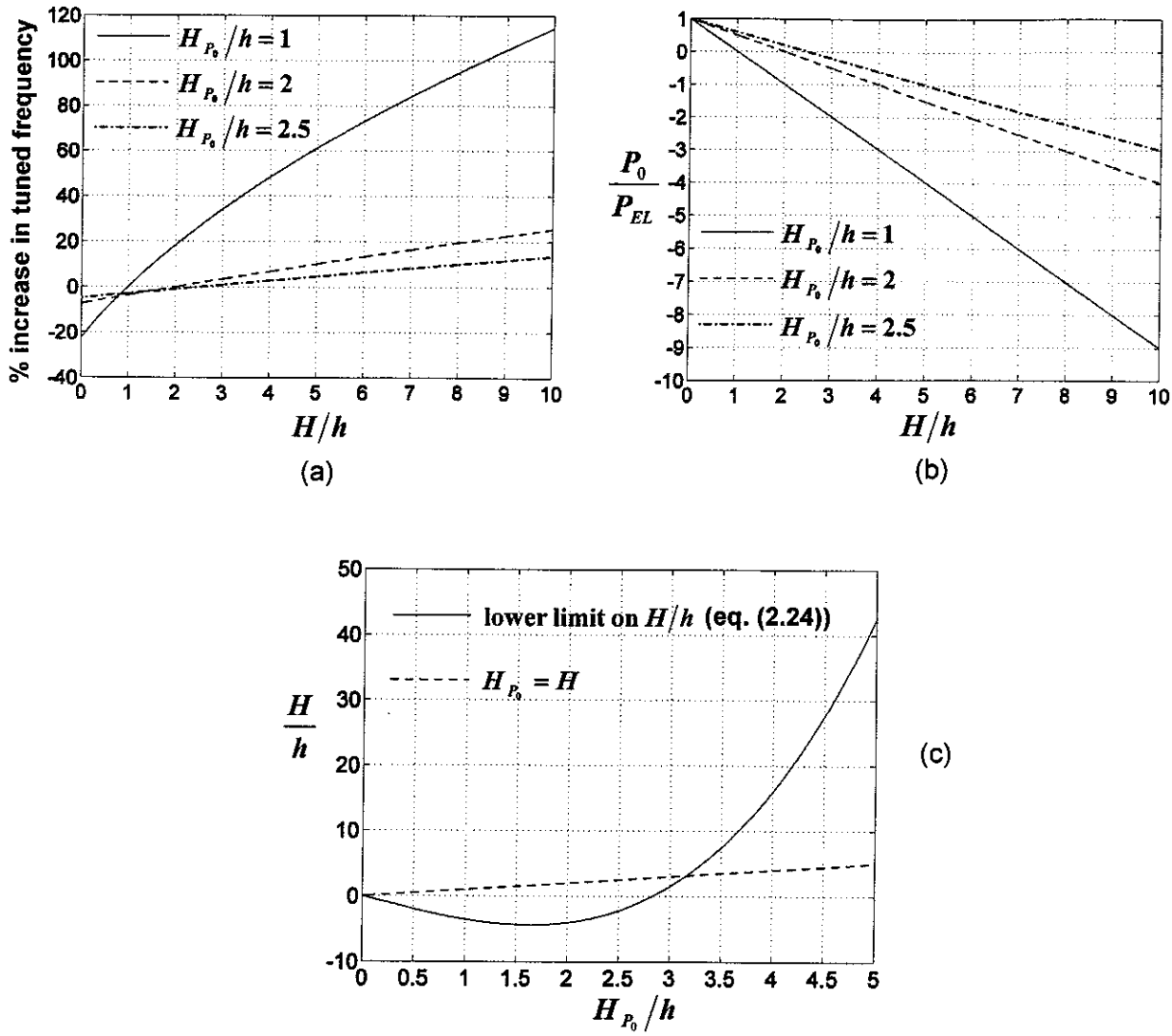

Figure 2.8: Performance curves for shallow arch ATVA with fixed H_{P_0}, variable H (Figure 2.6(b))

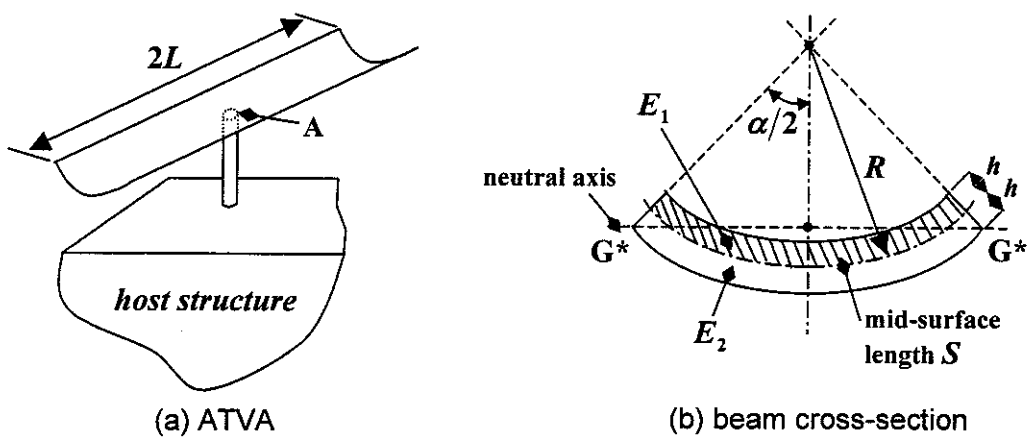

Figure 2.9: Cantilever-type ATVA with anticlastic curvature control

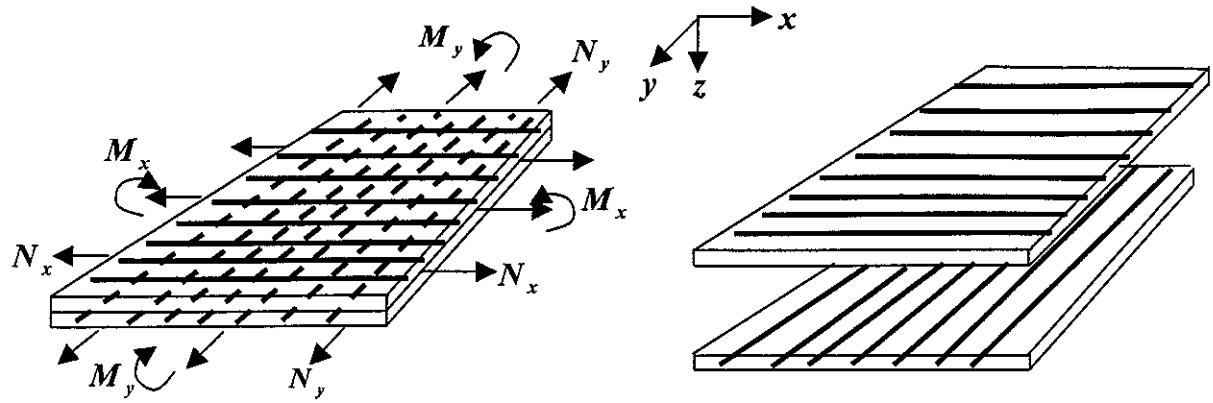

(a) laminate (b) exploded view of laminate

Figure 2.10: Two-layer cross-ply laminate

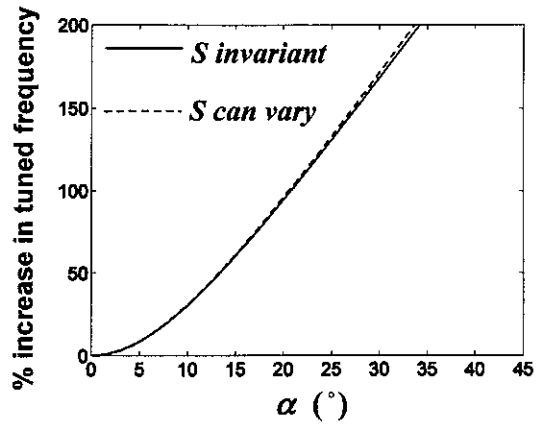

Figure 2.11: Tuning characteristic for cantilever type TVA in Figure 2.9 estimated from eq. (2.25) for a 2-layer cross-ply cross-section with $E_1, E_2 = 130, 10\,\text{GPa}$, $\upsilon_{12} = 0.3$, $2h = 2\times10^{-3}\,\text{m}$, $2L = 0.24\,\text{m}$.

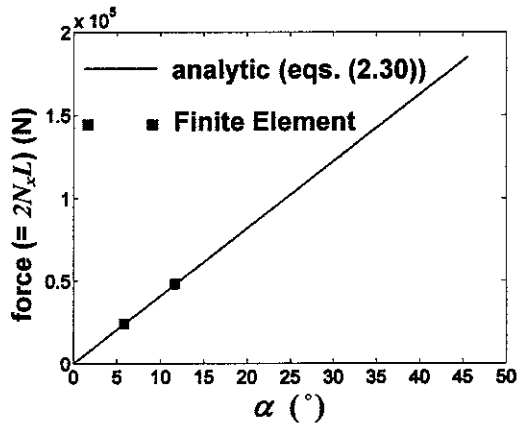

Figure 2.12: Edge force requirement for cross-section curvature for 2-layer cross-ply cross-section with $E_1, E_2 = 130, 10\,\text{GPa}$, $\upsilon_{12} = 0.3$, $2h = 2\times10^{-3}\,\text{m}$, $2L = 0.24\,\text{m}$.

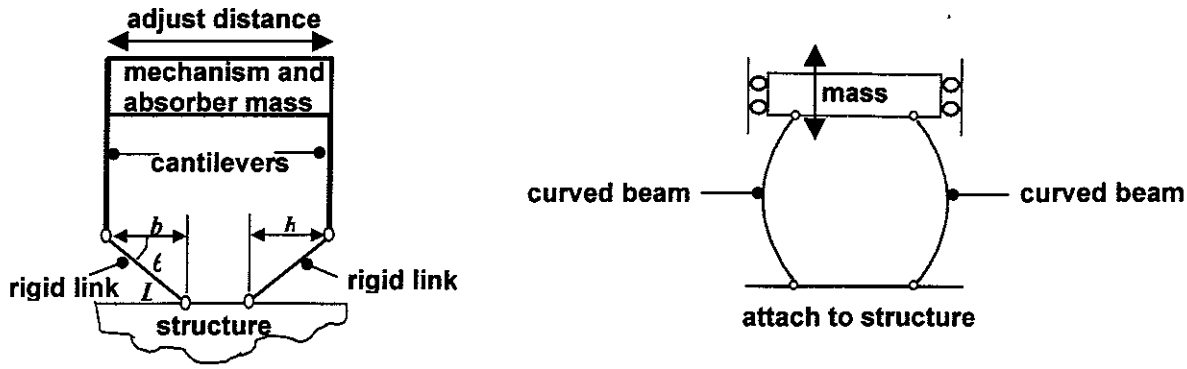

(a) ATVA linkage stiffness element

(b) ATVA with parallel curved beams as stiffness element

Figure 2.13: Designs of ATVA for stiffness adjustment by shape control with low actuator force

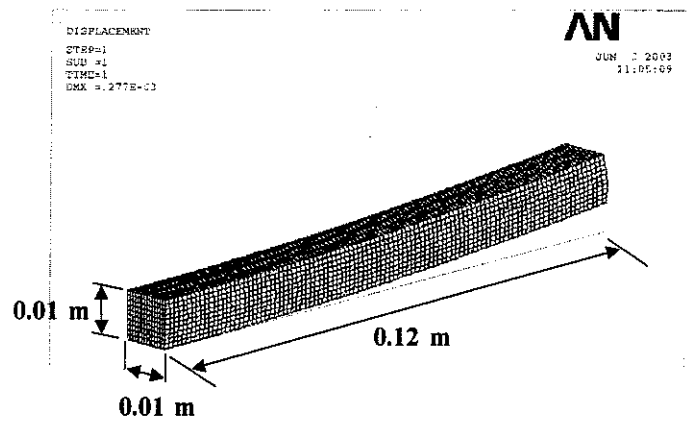

Figure 2.14: Finite Element model of clamped-free beam with a pressurised fluid-filled cavity separating a pair of laminae of orthotropic material with material axes at right angles to each other (thickness of each lamina is $0.25\,\mathrm{mm}$)

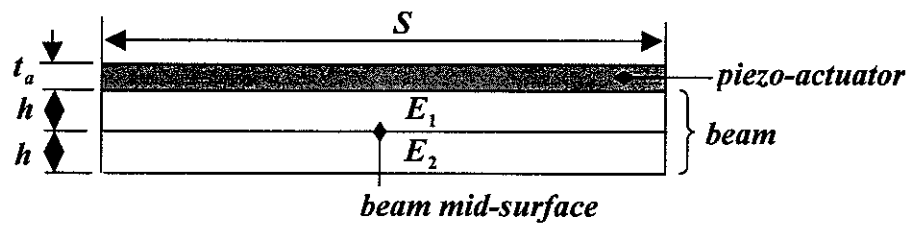

Figure 2.15: Beam with piezo-actuator

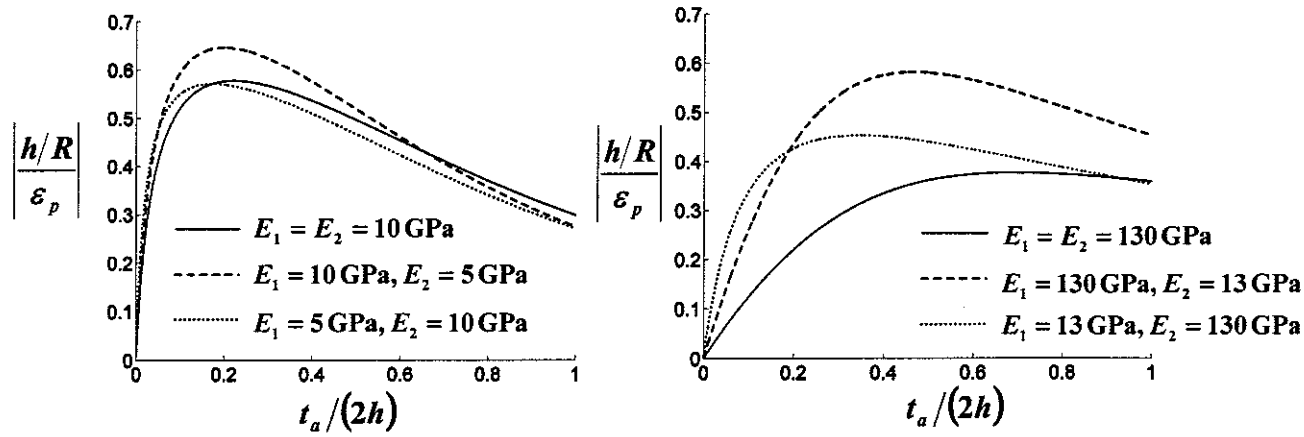

Figure 2.16: Variation of curvature to free strain ratio with actuator to beam thickness ratio for $b_a = b_b$ and $E_a = 59.5\,\text{GPa}$, $d_{31} = -212\times10^{-12}\,\text{m/V}$

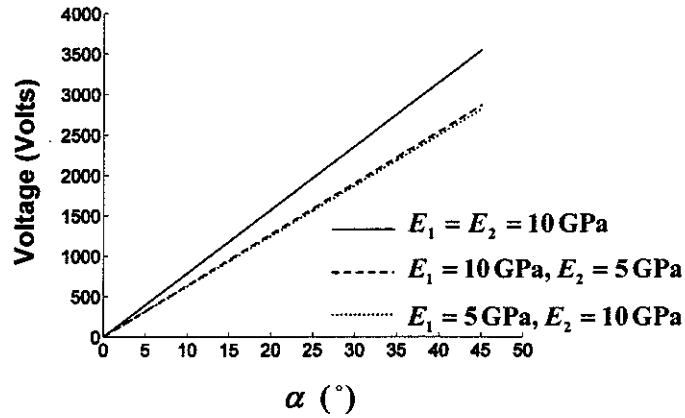

Figure 2.17: Minimum voltage versus subtended angle α for $b_a = b_b$ and $2h = 0.5\times10^{-3}\,\text{m}$, $S = 0.05\,\text{m}$, $E_a = 59.5\,\text{GPa}$, $d_{31} = -212\times10^{-12}\,\text{m/V}$

3 ATVA WITH LINKAGE STIFFNESS ELEMENT

This chapter discusses the use of a variable geometry linkage spring as the variable stiffness element in an adaptive tuned vibration absorber (ATVA). The theory is first presented and is subsequently validated by experiments.

3.1 Theory

Consider the hinged arch in Figure 3.1(a) where the rigid links AB, BC are pivoted at A, B and C and the cantilevers are of flexural stiffness k. The non-linear expression relating the applied static force F to y (Figure 3.1(b)) was derived in reference [20]:

$$\frac{F}{2kL} = \left\{ \frac{b}{L}\left[1-\left(\frac{y}{L}\right)^2\right]^{-\frac{1}{2}} - 1 \right\} \frac{y}{L} \tag{3.1}$$

From this expression, the non-dimensional linear stiffness for small deflections $\Delta y = y - y_0$ about the stable equilibrium position in Figure 3.1(a) can be derived:

$$\widetilde{K} \approx \frac{F/(2kL)}{\Delta y/L} = \frac{1}{(b/L)^2} - 1 \tag{3.2}$$

Hence, variable stiffness can be achieved by varying the distance $2b$ between the cantilevers. Figure 3.2(a) shows a schematic diagram of a self-tuning vibration absorber that uses this concept, its tuned frequency f_t being proportional to the square root of the stiffness given by equation (3.2). The actuating mechanism in Figure 3.2(a) is a redundant mass that degrades the vibration attenuation (eq.(2.6)). A better configuration that uses an identical spring element is shown in Figure 3.2(b) where the actuator is now part of the effective mass of the device. The tuning characteristic of either configuration in Figure 3.2 is shown in Figure 3.3, giving the percentage increase in f_t from a nominal configuration $b_{\text{nom}}/L = 0.8$ (i.e. $\theta_{0,\text{nom}} = 37°$ in Figure 3.2). The change in f_t per unit actuator movement is much less than that of the device in Figure 1.1 [4, 10]. However, whereas in that design the actuator acts against the flexural stiffness of each beam, the designs in Figure 3.2 require practically no actuator force to achieve shape change. Hence, a greater overall variation in f_t is possible.

The effectiveness of both devices in Figures 3.2 is limited to frequencies for which inertia effects of the components forming the linkage are negligible. For low values of θ_0 either device is prone to "snap through" to its lower stable equilibrium position at high amplitudes of vibration [20]. Moreover, for low values of θ_0, non-linearity is expected to be more pronounced, as shown in Figure 3.4, which compares the non-linear expression in eq. (3.1) with the linear (tangential)

relationship of eq. (3.2) for three different values of θ_0. It is also seen from Figure 3.4 that, for deflections from the stable equilibrium position of Figure 3.1(a), the spring hardens in tension ($F > 0$) and softens in compression ($F < 0$).

3.2 Experimental Testing

Figure 3.5 shows a demonstrator that was built in order to verify the tuning characteristic of Figure 3.3. The demonstrator is of the configuration shown in Figure 3.2(a) and $b_{\text{nom}}/L = 0.8$. The hinges were formed using miniature ball bearings (SKF 618/4). The distance between the cantilevers was manually adjusted by turning a screw. For each setting, the tuned frequency f_t and the damping loss factor η were measured by applying random excitation at the base of the device and measuring the transmissibility frequency response relating the acceleration at the base, $a_1(t)$, to that of the absorber mass $a_2(t)$. Assuming a linear relationship between these two signals and a single degree of freedom (SDOF) model for the effective part of the demonstrator:

$$T = \frac{A_2}{A_1} = \frac{1 + \mathrm{j}\eta}{1 - (f/f_t)^2 + \mathrm{j}\eta} \tag{3.3}$$

where η is the damping loss factor of the stiffness element, f is the frequency and A_1 and A_2 are the complex amplitudes of $a_1(t)$ and $a_2(t)$ for harmonic vibration i.e. when $a_r(t) = \mathrm{Re}\{A_r e^{\mathrm{j}2\pi ft}\}$, $r = 1, 2$. $|T|$ is maximum at $f = f_t$ and f_t and η were accurately located by considering that at this point, $\mathrm{Re}\{T\} = 1$ and $\mathrm{Im}\{T\} = -1/\eta$.

Figures 3.6(a, b) show the magnitude and phase of the transmissibility at low amplitude for the two extreme settings $\Delta b/L = 0.1$ and $\Delta b/L = -0.075$ for which the tuned frequencies are 70 Hz and 150 Hz respectively. It is seen that linear SDOF theory holds and that $\cos\phi \approx 0$ at $f = f_t$, in accordance with eq. (3.3). Figures 3.7(a,b) show that, at 10 times the amplitude, the linear theory still holds in the region of the tuned frequency and this frequency changes only slightly. In the case of the $\Delta b/L = 0.1$, harmonics appear, however these will have no effect on the operation of the an ATVA that uses such a spring. The damping estimate fluctuated considerably from one setting to the other (Figure 3.8). This is attributed to various factors relating to the construction and requires further investigation.

Figure 3.9 compares the predicted and measured tuning characteristics for the nominal configuration $b_{\text{nom}}/L = 0.8$, where the correlation between simulation and measurement is seen to remain reasonably good at high amplitude. The maximum variation in f_t is 70% for a total actuator movement of 1.6cm. The adjustment can be performed automatically in either

configuration in Figure 3.2 using a servomotor driving as screw, as was performed in [10] for the beam-like ATVA in Figure 1.1.

3.3 Conclusions

This chapter presented a novel design for an ATVA that uses a variable geometry linkage spring as the stiffness element. The advantages of this design are:

- Minimal actuating force is required to achieve shape change (70% for 1.6cm actuator movement);
- A wide tuning range is possible.

The disadvantages are:

- The design assumes no inertia effects in the spring. In reality these will limit the maximum frequency to which it can be used;
- The spring is fairly complex in construction, particularly the hinges.

Figures

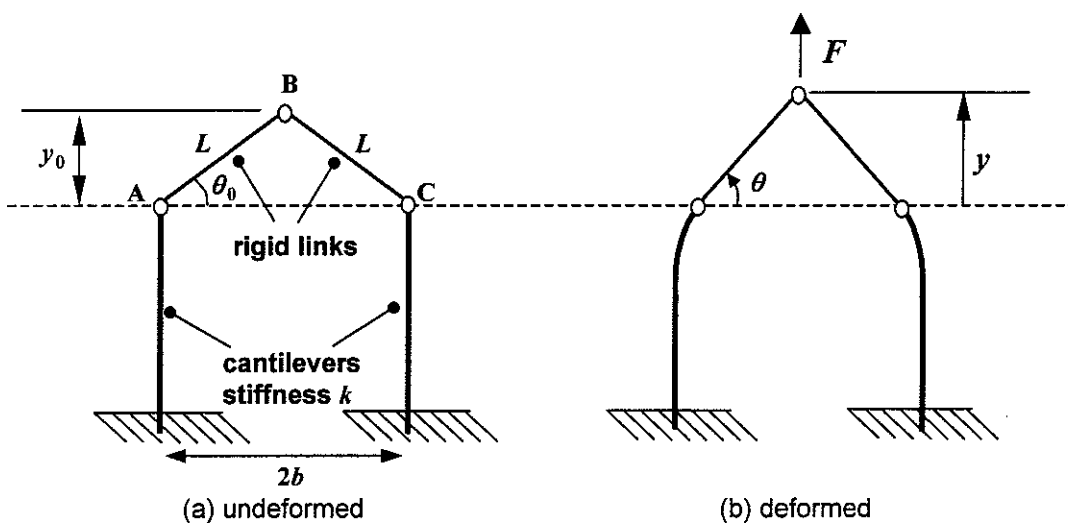

Figure 3.1: Linkage spring

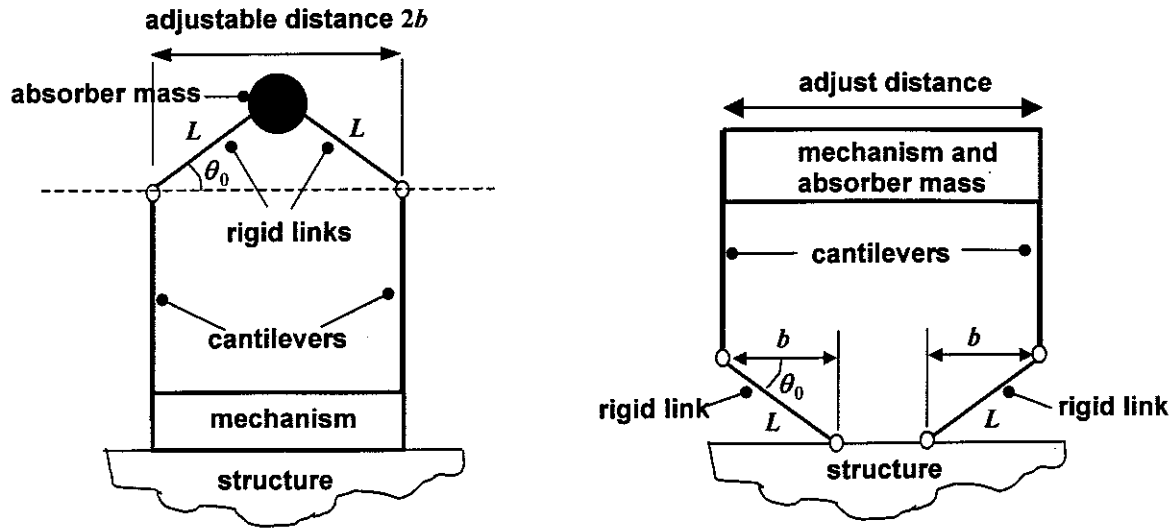

(a) (b)

Figure 3.2: Schematics of linkage spring ATVA

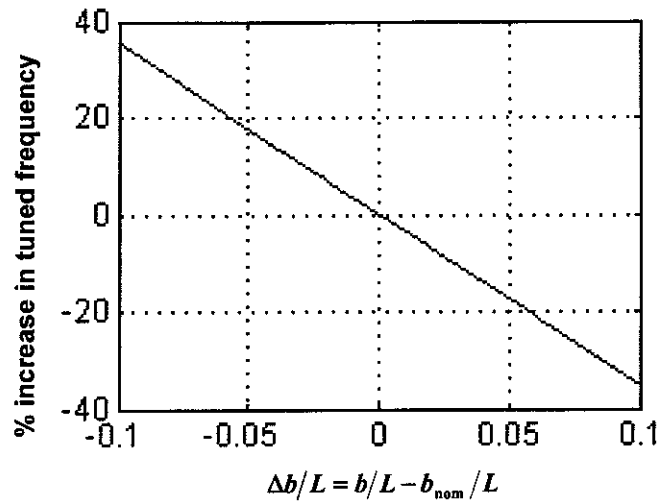

Figure 3.3: Tuning characteristic for $b_{\text{nom}}/L = 0.8$ (i.e. $\theta_{0,\text{nom}} = 37°$)

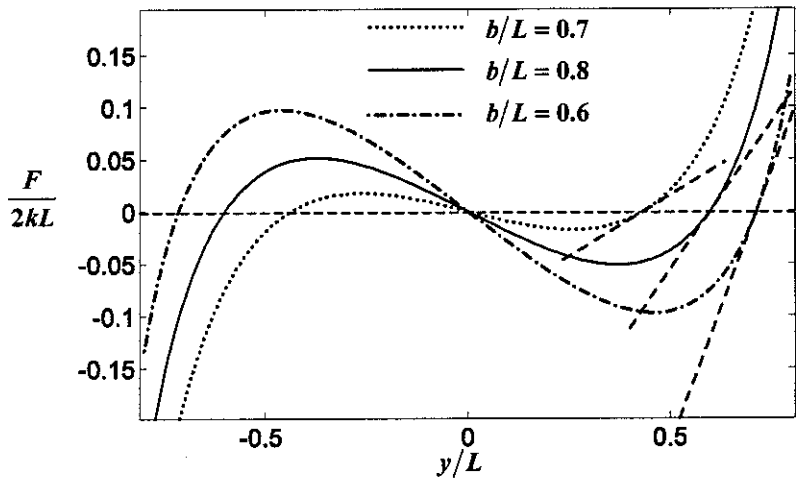

Figure 3.4: Non-linear relationship between F and y for various b/L values

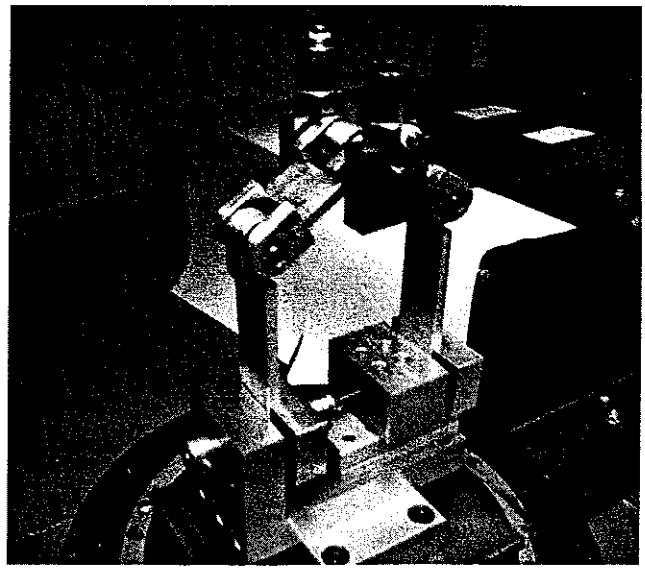

Figure 3.5: Demonstrator for manually tuned linkage spring device

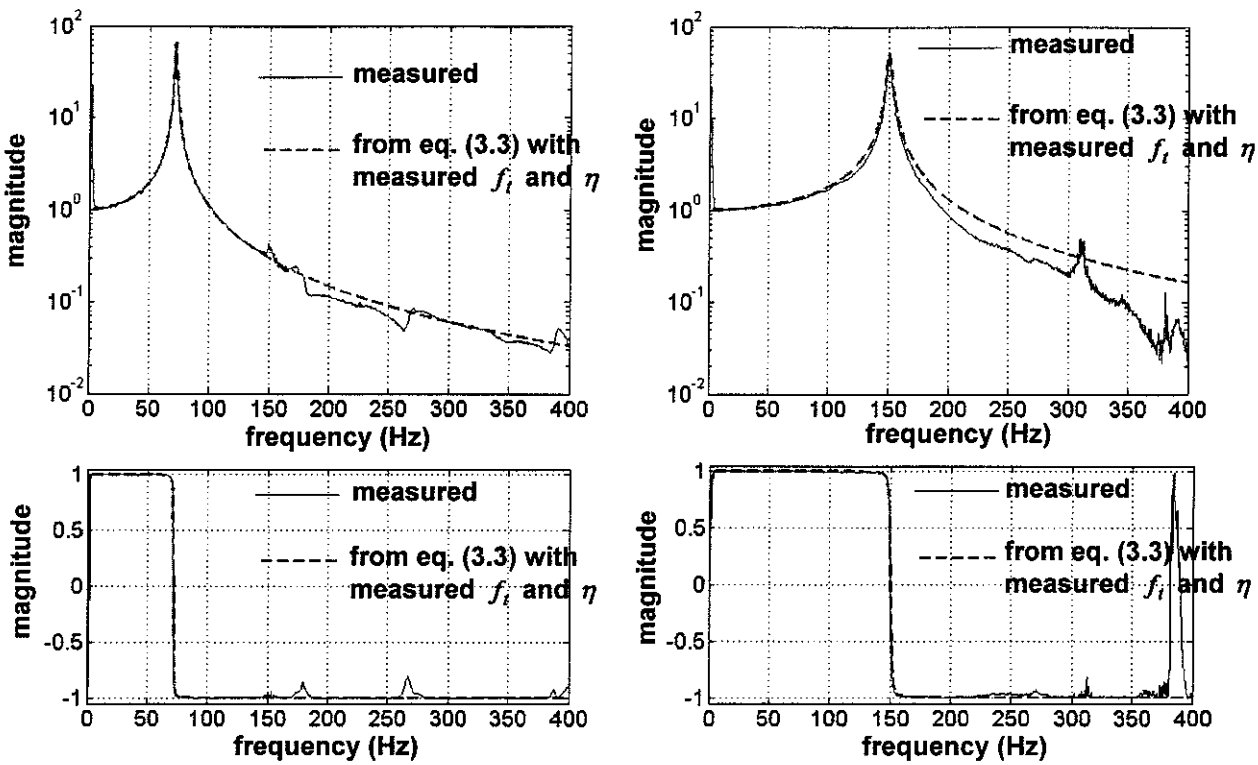

(a) $\Delta b/L = 0.1$ (b) $\Delta b/L = -0.075$

Figure 3.6: Transmissibility plots at low amplitude ($\Delta b/L = b/L - b_{\text{nom}}/L,\ b_{\text{nom}}/L = 0.8$)

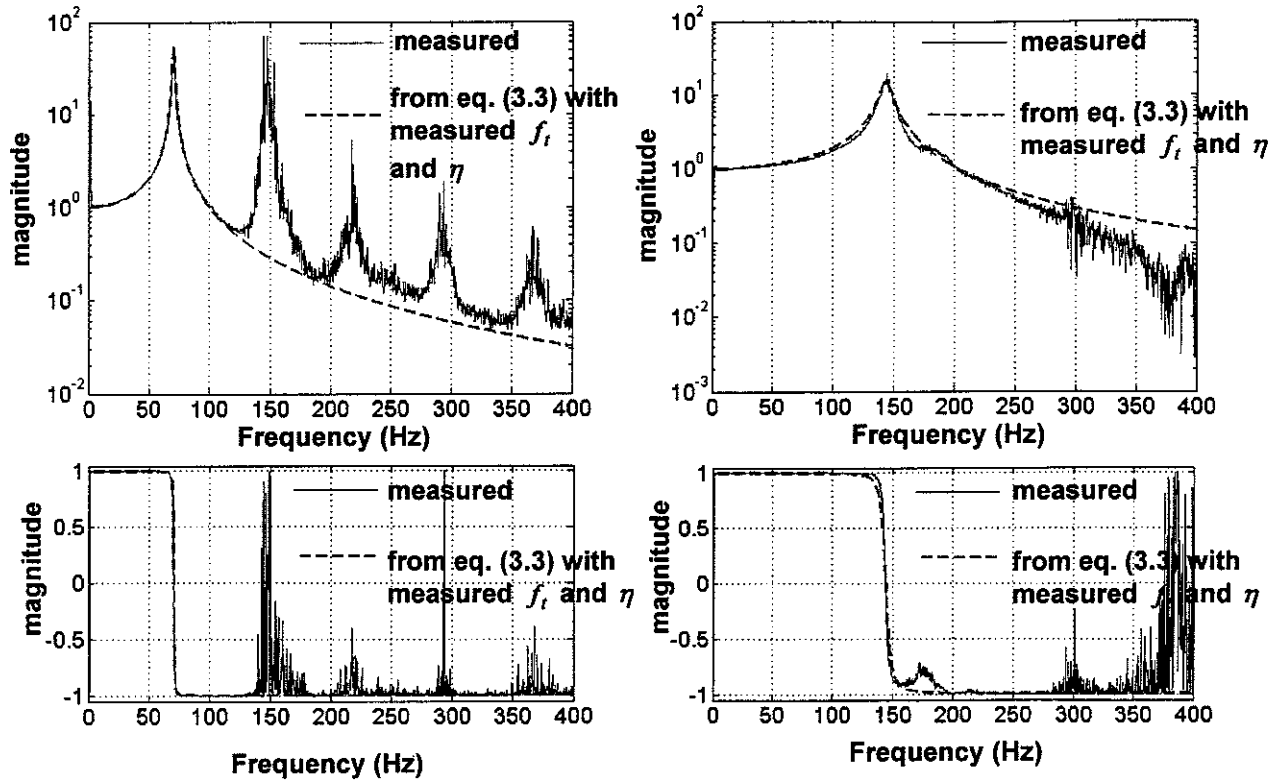

(a) $\Delta b/L = 0.1$ (b) $\Delta b/L = -0.075$

Figure 3.7: Transmissibility plots at 10 x amplitude ($\Delta b/L = b/L - b_{\text{nom}}/L,\ b_{\text{nom}}/L = 0.8$)

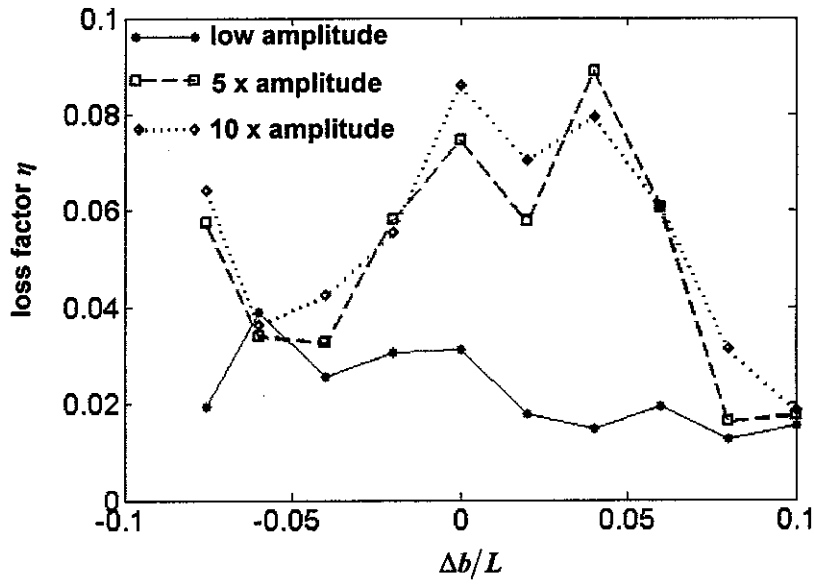

Figure 3.8: Measured loss factor estimates ($\Delta b/L = b/L - b_{\text{nom}}/L,\ b_{\text{nom}}/L = 0.8$)

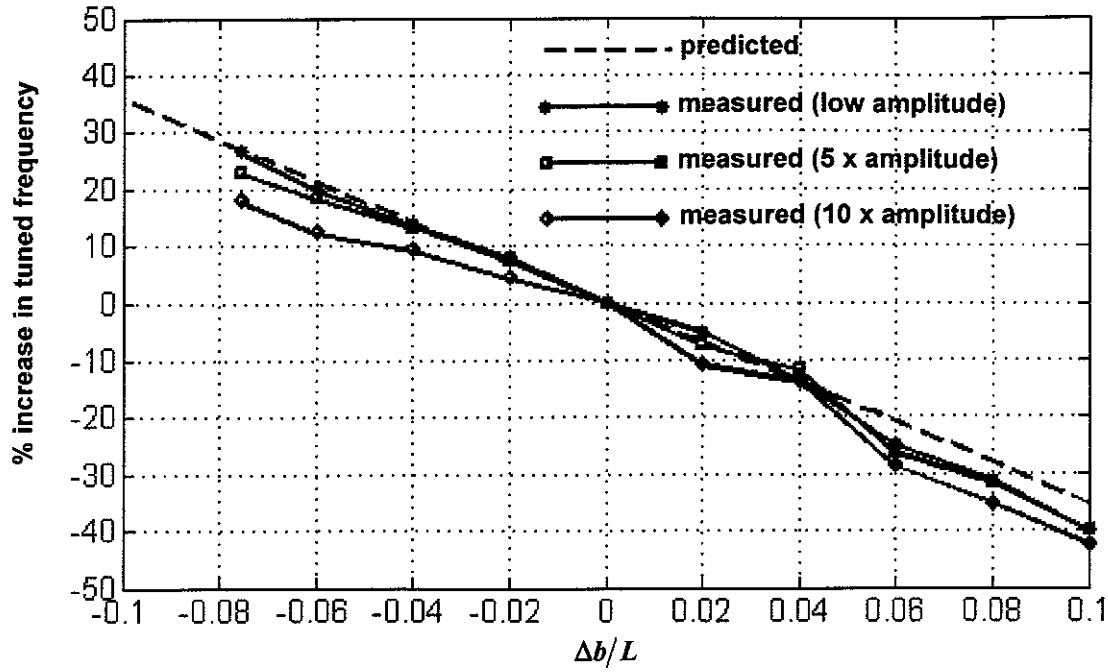

Figure 3.9: Tuning characteristic ($\Delta b/L = b/L - b_{\text{nom}}/L,\ b_{\text{nom}}/L = 0.8$)

4 ATVA WITH CURVED BEAMS AS STIFFNESS ELEMENT

In this chapter an ATVA with parallel identical beams of adjustable curvature vibrating longitudinally is proposed (see Figure 4.1). The advantage of this design is that, while the effective stiffness of the ATVA (in the direction of vibration) can be considerable, the curvature of each beam is relatively easy to adjust by flexure since it is pivoted at the ends and one end is free to move. One way of changing the curvature of the beams of such an ATVA is to bond a layer of piezoelectric ceramic to each beam and adjusting the level of dc voltage applied to these actuators. The proposed use of the beams in Figure 4.1 is totally different from that proposed in reference [21], despite the similarly looking set-up. In that work, the beams were post-buckled struts used as passive vibration isolators due to their very low stiffness in the direction of vibration and high load carrying capacity.

This chapter starts with an elementary analysis of the design. This is followed by a more detailed analysis, taking into account non-linearity and inertia effects in the stiffness element. A prototype ATVA of this design is then presented and its performance is illustrated with both simulated and experimental results.

4.1 Elementary Theory

Consider the beam in Figure 4.2(a), which is pivoted at its ends and has an initial curvature in the form of a circular arc of length S subtending an angle α at the centre. The beam is subjected to the compressive load P along its span and deforms as shown in Figure 4.2(b). The analysis in this section assumes that the deformation is so small as to have negligible effect on the geometry of the beam. Using Castigliano's theorem [12], assuming the beam is slender and considering bending deformation only, neglecting any deformation along the curved longitudinal axis of the beam (S constant), the non-dimensional static stiffness in the span-wise direction is given by (Appendix 3):

$$\widetilde{K} = \frac{2\alpha^3}{\pi^2\{2\alpha - 3\sin\alpha + \alpha\cos\alpha\}} \tag{4.1}$$

where

$$\widetilde{K} = \frac{P/P_E}{u/S} = \frac{\widetilde{P}}{\widetilde{u}} \tag{4.2}$$

and

$$P_E = \pi^2 EI/S^2 \tag{4.3}$$

i.e. P_E is the Euler buckling load of a straight beam of the same length S, Young's Modulus E and second moment of area of cross-section I as the beam. From eq. (4.2):

$$\widetilde{K} = (S/P_E)K \tag{4.4}$$

where $K = P/u$ is the stiffness. Since the crown height H is related to the curvature by the formula

$$H/S = \{1-\cos(\alpha/2)\}/\alpha \tag{4.5}$$

it can be shown graphically that:

$$\tilde{K} \approx \frac{2}{\pi^2 (H/S)^2} \tag{4.6}$$

The tuned frequency f_t of the TVA in Figure 4.1 is proportional to the square root of $\tilde{K}$, and so it is approximately inversely proportional to the crown height H of the beams (Figure 4.2).

Piezo-actuated beams used in the ATVA are composite beams. However, it is assumed that both the above and subsequent analyses still apply for this case since the deformation is mostly in bending and an equivalent cross-section of uniform material can always be found. This is not necessary, however, since the flexural rigidity EI does not feature in the non-dimensional analysis.

The above analysis neglects the non-linearity in the P-u relationship for finite deformations. Hence, if the TVA is oriented vertically, the static load of the absorber mass will influence the linear vibration characteristics about the static equilibrium position. Additionally, regardless of the static load, large amplitude vibrations will be non-linear, to some extent. The analysis in this section also neglects the effect of the inertia of the beam. The influence of each of these effects on the TVA performance is quantified separately in turn in the following sections.

4.2 Non-linearity, Effect of Static Load

The non-linear relationship between $\tilde{u}$ and $\tilde{P}$, $\tilde{u} = \tilde{u}(\tilde{P}, \alpha)$, for the curved beam is derived by two methods. Both analyses assume that the beam is slender and that S is constant.

The first method is "exact" in that it makes no assumptions regarding the degree of curvature. It is similar to the analysis in reference [22] for large deflections of an initially straight strut, but allows for the initial curvature. With reference to Figure 4.2(b), for each value of load $\tilde{P}$, the deflection $\tilde{u}$ is computed numerically as follows.

i. Find the end slope angle of the deformed beam, θ_0, by solving the equation

$$G(\theta_0, \tilde{P}, \alpha) = \int_0^{\theta_0} \frac{d\theta}{\sqrt{\{\alpha^2/(4\pi^2\tilde{P}) + \sin^2(\theta_0/2) - \sin^2(\theta/2)\}}} - \pi\tilde{P}^{\frac{1}{2}} = 0 \tag{4.7a}$$

ii. Compute $\tilde{u}$ from:

$$\tilde{u}(\tilde{P}, \alpha) = \frac{2}{\alpha}\sin(\alpha/2) - \frac{2}{\pi\tilde{P}^{\frac{1}{2}}} \int_0^{\theta_0} \frac{\cos^2(\theta/2)}{\sqrt{\{\alpha^2/(4\pi^2\tilde{P}) + \sin^2(\theta_0/2) - \sin^2(\theta/2)\}}}\, d\theta + 1 \tag{4.7b}$$

Equations (4.7) apply for $\widetilde{P} > 0$ (i.e. compression). For $\widetilde{P} < 0$ (i.e. tension), eqs. (4.7) are each modified by replacing the $\widetilde{P}^{1/2}$ term by $\left(-\widetilde{P}\right)^{1/2}$ and inverting the sign of the bracketed term under the radical. The derivation of these equations is given in the Appendix 4. For each given angle α within a range, eq. (4.7a) was solved numerically using Muller's algorithm [23] over a range of loads $\widetilde{P}$, enabling the evaluation of the corresponding values of $\widetilde{u}$ (eq. (4.7)).

The second method for the derivation of the relation $\widetilde{u} = \widetilde{u}\left(\widetilde{P}, \alpha\right)$ is an approximate analytical method that assumes that the arch in Figure 4.2 is initially shallow and remains so after deformation. Moreover, the undeformed circular profile of the arch is approximated by a sinusoidal function

$$w_i = H \sin(\pi x / L) \tag{4.8}$$

Then the deformed profile is given by [12]:

$$w = H\left[P_{EL}/\left(P_{EL} - P\right)\right]\sin(\pi x / L) \tag{4.9}$$

where

$$P_{EL} = \pi^2 EI / L^2 \tag{4.10}$$

If $\xi(x)$ is the displacement in the x direction of a point initially at x (Figure 4.2), then $(\delta s)^2 = (\delta w_i)^2 + (\delta x)^2 = (\delta w)^2 + (\delta x + \delta\xi)^2$. Neglecting $(d\xi/dx)^2$:

$$\frac{d\xi}{dx} \approx \frac{1}{2}\left\{\left(\frac{dw_i}{dx}\right)^2 - \left(\frac{dw}{dx}\right)^2\right\} \tag{4.11}$$

Substituting eqs. (4.8) and (4.9) in eq. (4.11) and integrating from $x = 0$ to $x = L$ and noting that $u = \xi(0) - \xi(L)$:

$$\frac{u}{L} = \frac{\pi^2}{4}\left(\frac{H}{L}\right)^2 \left\{\left(1 - P/P_{EL}\right)^{-2} - 1\right\} \tag{4.12}$$

The approximate value for $\widetilde{u}$ for given $\widetilde{P}$ and α can be obtained from eq. (4.12) using the following transformations:

$$P/P_{EL} = \widetilde{P}(L/S)^2, \quad H/L = (H/S)(S/L), \quad \widetilde{u} = (u/L)(L/S) \tag{4.13a,b,c}$$

where H/S is given by eq. (4.5) and, for the circular arch (Figure 4.2(a)):

$$L/S = (2/\alpha)\sin(\alpha/2) \tag{4.14}$$

Figure 4.3 shows the $\widetilde{P}$-$\widetilde{u}$ curves for three values of α. Reasonable agreement between the two methods is evident, particularly for compression ($\widetilde{P} > 0$). Figure 4.3 shows that the curved beam is neither a softening spring nor a hardening spring: in fact, it softens in compression and

hardens in tension. It is also seen from Figure 4.3 that the Castigliano stiffness $\widetilde{K}$, given by eqs. (4.1), (4.2), is the slope at the origin of the $\widetilde{P}$-$\widetilde{u}$ curve i.e.:

$$\widetilde{K} = \left.\frac{\partial \widetilde{P}}{\partial \widetilde{u}}\right|_{\widetilde{P}=0} \tag{4.15}$$

4.2.1 Effect of static load

This section examines the linear performance of the TVA under a static load. The effect of a compressive static load $\widetilde{P}_0$ is to reduce the tuned frequency by a factor:

$$\frac{f_{t,v}}{f_{t,h}} = \sqrt{\left.\frac{1}{\widetilde{K}}\frac{\partial \widetilde{P}}{\partial \widetilde{u}}\right|_{\widetilde{P}=\widetilde{P}_0}} \tag{4.16}$$

where $f_{t,v}$ is the tuned frequency under the static load $\widetilde{P}_0$ and $f_{t,h}$ that at no static load. For a fixed $\widetilde{P}_0$, the reduction factor in eq. (4.16) can be computed for a range of values of α, as shown in Figure 4.4, by evaluating the slope of the $\widetilde{P}$-$\widetilde{u}$ curve at the operating points $\left(\widetilde{u}_0, \widetilde{P}_0\right)$ where $\widetilde{u}_0 = \widetilde{u}\left(\widetilde{P}_0, \alpha\right)$. The tuning characteristic of the TVA under a fixed static load can then be obtained:

$$\frac{\Delta f_{t,v}}{f_{t,v,ref}} = \frac{f_{t,v} - f_{t,v,ref}}{f_{t,v,ref}} \tag{4.17}$$

where $f_{t,v,ref}$ is the tuned frequency under $\widetilde{P}_0$ at some reference value of α, α_{ref}, with $f_{t,h,ref}$ being the corresponding frequency at no static load. Eq. (4.17) can be written as

$$\frac{\Delta f_{t,v}}{f_{t,v,ref}} = \frac{f_{t,v}/f_{t,h}}{\left(f_{t,v,ref}/f_{t,h,ref}\right)\left(f_{t,h,ref}/f_{t,h}\right)} - 1 \tag{4.18}$$

where the ratios $f_{t,v}/f_{t,h}$ and $f_{t,v,ref}/f_{t,h,ref}$ are evaluated from eq. (4.16) and

$$f_{t,h,ref}/f_{t,h} = \sqrt{\widetilde{K}(\alpha_{ref})/\widetilde{K}(\alpha)} \tag{4.19}$$

The tuning characteristic of eq. (4.18) can be compared with that for no static load:

$$\Delta f_{t,h}/f_{t,h,ref} = \sqrt{\widetilde{K}(\alpha)/\widetilde{K}(\alpha_{ref})} - 1 \tag{4.20}$$

In this study, $\widetilde{P}_0$ is equal to the compressive static load of the absorber mass m_2 (TVA oriented vertically):

$$\widetilde{P}_0 = \widetilde{W} = m_2 g / P_E \tag{4.21}$$

Now

$$4\pi^2 f_{t,h}^2 = K/m_2 \tag{4.22}$$

Combining eqs. (4.21), (4.22) , and (4.4):

$$\widetilde{W} = g\widetilde{K}/\left(4\pi^2 f_{t,h}^2 S\right) \tag{4.23}$$

Since $\widetilde{K} = \widetilde{K}(\alpha)$, eq. (4.23) states that $\widetilde{W}$ is fully determined by specifying S and the reference values α_{ref} and $f_{t,h,ref}$. For the prototype tested in this report, $S = 0.083\,\text{m}$ and $\alpha_{ref} = 38(\pi/180)$, the angle value (in radians) at zero voltage applied to the piezo-actuated beams. $f_{t,h,ref}$ was determined by trial and error calculation, knowing the measured value of $f_{t,v,ref}$ (42 Hz). With $f_{t,h,ref}$ taken as 44.5 Hz, the reduction factor at $\alpha = \alpha_{ref}$ was 0.94 (eq. (4.16)), giving a value $f_{t,v,ref} = 42$ Hz, as measured. The predicted effect of the static load on the prototype was then determined, and is shown in Figure 4.5. Figure 4.5(a) shows the predicted variation of the non-linear static compression $\widetilde{u}_0$ with α. Figure 4.5(b) shows that the reduction factor $f_{t,v}/f_{t,h}$ is not only reasonably small, but it is practically constant. Hence, it has virtually no effect on the tuning characteristic (Figure 4.5(c)). This means that the tuning characteristic of the ATVA can be determined from eqs. (4.1) with virtually no loss in accuracy, as far as static loading is concerned.

4.2.2 Non-linear vibration

The degree of non-linearity of the vibration is next investigated. For simplicity, the host structure is assumed mass-like, as in Figure 4.6. The non-linear equations of motion can be written as:

$$m_2\ddot{x}_2 = P_E\widetilde{P}(\widetilde{u}) + C\dot{u} - P_E\widetilde{P}_0 \tag{4.24a}$$

$$m_1\ddot{x}_1 = -P_E\widetilde{P}(\widetilde{u}) + F(t) \tag{4.24b}$$

where $u = \widetilde{u}S = x_1 - x_2$ and C the equivalent viscous damping coefficient of the TVA stiffness element. The harmonic disturbance $F(t) = \text{Re}\left\{\underline{F}\text{e}^{\text{j}\omega t}\right\}$ can be expressed as:

$$F(t) = m_1\,\text{Re}\left\{\underline{a}_{1,free}\text{e}^{\text{j}\omega t}\right\} \tag{4.25}$$

where $a_{1,free}(t) = \text{Re}\left\{\underline{a}_{1,free}\text{e}^{\text{j}\omega t}\right\}$ is the "free acceleration" of m_1 (i.e. without TVA attached).

Let $\tau = \omega_{t,h}t$, where $\omega_{t,h} = 2\pi f_{t,h}$, and $(\,)' = d(\,)/d\tau$. Dividing eqs. (4.24a) and (4.24b) respectively by $m_2\omega_{t,h}^2 S$ and $m_1\omega_{t,h}^2 S$ and noting that $P_E/\left(m_2\omega_{t,h}^2 S\right) = P_E/(KS) = 1/\widetilde{K}$ (from eq. (4.4)) and $|\underline{F}|/\left(m_1\omega_{t,h}^2 S\right) = |\underline{a}_{1,free}|/\left(\omega_{t,h}^2 S\right) = |\underline{a}_{1,free}|\widetilde{W}/\left(g\widetilde{K}\right)$ (from eq. (4.23)), equations (4.24) can be written as:

$$\widetilde{x}_2'' = \widetilde{P}(\widetilde{u})/\widetilde{K} + 2\zeta\widetilde{u}' - \widetilde{P}_0/\widetilde{K} \tag{4.26a}$$

$$\widetilde{x}_1'' = -\mu\widetilde{P}(\widetilde{u})/\widetilde{K} + \left(\widetilde{W}/\widetilde{K}\right)|\underline{\widetilde{a}}_{1,free}|\cos\widetilde{\omega}_h\tau \tag{4.26b}$$

where $\widetilde{x}_i = x_i/S$, $i = 1, 2$, $\mu = m_2/m_1$, $\widetilde{\omega}_h = \omega/\omega_{t,h}$,

$$\left|\tilde{\underline{a}}_{1,free}\right| = \left|\underline{a}_{1,free}\right| / g \tag{4.27}$$

ξ is the equivalent viscous damping factor for TVA:

$$\zeta = C/\left(2m_2\omega_{t,h}\right) \tag{4.28}$$

and $\tilde{P}_0 = \tilde{W}$ for TVA oriented vertically.

For given μ, ζ, α and $\tilde{W}$ it is possible to predict the non-linear vibration response over a range of frequency $\tilde{\omega}_h$ for various levels of excitation, quantified by $\left|\tilde{\underline{a}}_{1,free}\right|$. From eq. (4.23), $\tilde{W}$ is determined by specifying S, α and $\omega_{t,h}$, the latter quantity being determined from the measured value of $\omega_{t,v} = 2\pi f_{t,v}$. Moreover, by multiplying $\tilde{x}_i$ $(i = 1, 2)$, $\tilde{x}_i'$ and $\tilde{x}_i''$ by S, $S\omega_{t,h}$ and $S\omega_{t,h}^2$ respectively, the actual magnitudes of the displacements, velocities and accelerations could be obtained. The parameters used in this analysis are $S = 0.083\,\text{m}$, $\alpha = 38\pi/180$, $f_{t,h} = 44.5$ Hz, $f_{t,v} = 42$ Hz.

Equations (4.26) were solved for the periodic response using the harmonic balance method [24], where five harmonics of the excitation frequency were included. Figure 4.7(a) shows the response at the host structure (m_1) for three different levels of excitation. The vertical axis shows the displacement amplitude, defined as one half the peak-to-peak value of $\tilde{x}_1$ over one cycle, and the horizontal axis shows the non-dimensional excitation frequency normalised by the tuned frequency of the vertically oriented TVA i.e. $\tilde{\omega}_v = \omega/\omega_{t,v}$. Figure 4.7(b) shows the corresponding variation of $\langle\cos\phi\rangle$, defined using eq. (2.5) as

$$\langle\cos\phi\rangle = \frac{\int_0^{\tilde{T}} \tilde{x}_1''\tilde{x}_2''\,d\tau}{\left\{\int_0^{\tilde{T}} \left(\tilde{x}_1''\right)^2\,d\tau\right\}^{\frac{1}{2}}\left\{\int_0^{\tilde{T}} \left(\tilde{x}_2''\right)^2\,d\tau\right\}^{\frac{1}{2}}} \tag{4.29}$$

where $\tilde{T} = 2\pi/\tilde{\omega}_h$. Hence, $\langle\cos\phi\rangle$ is an estimate for the cosine of the phase between the accelerations a_1 and a_2, taking into account the corruption of the signals due to the harmonics arising from the non-linearity. Figures 4.7(a,b) show that non-linearities do not significantly affect the TVA performance for free acceleration amplitudes of m_1 up to $2g$. In fact, an anti-resonance in the displacement response at m_1 still occurs approximately at the (linear) tuned frequency $\omega \approx \omega_{t,v}$ and $\langle\cos\phi\rangle$ is approximately zero in this condition. This will not be the case for higher free acceleration amplitudes (Figures 4.8(a,b)) due to strong harmonics. Figure 4.8(c) shows the corresponding variation of the maximum, mean and minimum values of the compression $\tilde{u}$ of the beams over one oscillation. It is clear that the beams experience tension ($\tilde{u} < 0$) as well as

compression, and the hardening effect due to the tension appears to predominate since the effective ("non-linear") tuned frequency in Figure 4.8(a) is greater than the linear value $\omega_{t,v}$. However, the conditions in Figure 4.8 are extreme and the free acceleration amplitude at m_1 is unlikely to exceed $2g$ for the parameters used. An indication of the actual magnitudes of the displacements and accelerations predicted for this level of excitation is given in Figure 4.9, which also compares the non-linear predictions with the linearised ones. It is seen that, at the tuned condition, the non-linearity affects the attenuation in acceleration more than the attenuation in displacement.

Based on the analysis in this section, it is concluded that non-linear effects do not significantly alter the performance of the prototype TVA and so need not be considered any further.

4.3 Inertia Effect of Curved Beam

An analysis of the linear vibrations of a curved beam, taking into account of its distributed inertia was performed by the dynamic stiffness method (DSM). The static load is ignored in the analysis. Damping is also ignored. The initial part of the analysis applies, strictly speaking, to a homogeneous beam. However, when it is specialised to the case of the TVA beams (Figure 4.1), which deform almost entirely by bending, it is reasonable to assume that the non-dimensional results are valid for composite beams, as explained in the penultimate paragraph of section 4.1.

Referring to Figure 4.10, the equations of the harmonic vibration of a beam that is curved in the form of an arc of a circle are obtained by specialising Flügge's equations for a cylindrical shell [25], and can be written as:

$$\frac{d^4\underline{\widetilde{w}}}{d\varsigma^4}+2\alpha^2\frac{d^2\underline{\widetilde{w}}}{d\varsigma^2}+\left[\alpha^4+\alpha^2\left(\frac{S}{r}\right)^2-\pi^4\widetilde{\omega}^2\right]\underline{\widetilde{w}}+\alpha\left(\frac{S}{r}\right)^2\frac{d\underline{\widetilde{v}}}{d\varsigma}=0 \tag{4.30a}$$

$$\frac{d^2\underline{\widetilde{v}}}{d\varsigma^2}+\pi^4\widetilde{\omega}^2\left(\frac{r}{S}\right)^2\underline{\widetilde{v}}+\alpha\frac{d\underline{\widetilde{w}}}{d\varsigma}=0 \tag{4.30b}$$

where $\widetilde{w}=\mathrm{Re}\{\underline{\widetilde{w}}\,e^{j\omega t}\}$, $\widetilde{v}=\mathrm{Re}\{\underline{\widetilde{v}}\,e^{j\omega t}\}$, $\widetilde{w}=w/S$, $\widetilde{v}=v/S$, $\varsigma=s/S$, r is the radius of gyration:

$$r=\sqrt{I/A} \tag{4.31}$$

A being the cross-sectional area, and $\widetilde{\omega}$ is the frequency ratio:

$$\widetilde{\omega}=\omega/\omega_s \tag{4.32}$$

where ω_s rad/s is the fundamental frequency of lateral vibrations of a straight beam of the same length, cross-section and material:

$$\omega_s=(\pi/S)^2\sqrt{(EI/\gamma)} \tag{4.33}$$

γ being the mass per unit length. Assuming plane wave solutions:

$$\underline{\tilde{w}} = A\mathrm{e}^{-\mathrm{j}\tilde{k}\varsigma}, \quad \underline{\tilde{v}} = B\mathrm{e}^{-\mathrm{j}\tilde{k}\varsigma} \tag{4.34a,b}$$

and substituting eqs. (4.34) in eqs. (4.30) and equating the determinant of the coefficient matrix of the resulting homogeneous equation to zero, the following polynomial equation is obtained:

$$\begin{aligned}&\tilde{k}^6 - \left[2\alpha^2 + \pi^4\left(\frac{r}{S}\right)^2\tilde{\omega}^2\right]\tilde{k}^4 + \left[\alpha^4 + 2\alpha^2\pi^4\left(\frac{r}{S}\right)^2\tilde{\omega}^2 - \pi^4\tilde{\omega}^2\right]\tilde{k}^2 \\ &+ \pi^4\left(\frac{r}{S}\right)^2\tilde{\omega}^2\left[\alpha^4 + \alpha^2\left(\frac{S}{r}\right)^2 - \pi^4\tilde{\omega}^2\right] = 0\end{aligned} \tag{4.35}$$

This equation gives six solutions for the non-dimensional wave number $\tilde{k}$,

$$\tilde{k} = \tilde{k}_1, \ldots, \tilde{k}_6 \tag{4.36}$$

Hence,

$$\underline{\tilde{w}} = \sum_{p=1}^{6} A_p \mathrm{e}^{-\mathrm{j}\tilde{k}_p\varsigma}, \quad \underline{\tilde{v}} = \sum_{p=1}^{6} R_p A_p \mathrm{e}^{-\mathrm{j}\tilde{k}_p\varsigma} \tag{4.37}$$

where

$$R_p = \frac{\mathrm{j}\alpha\tilde{k}_p}{\pi^4(r/S)^2\tilde{\omega}^2 - \tilde{k}_p^2} \tag{4.38}$$

Noting that the cross-section rotation $\psi = \partial\tilde{w}/\partial\varsigma$, and applying the displacement boundary conditions, the following equation is obtained:

$$\underline{\tilde{\mathbf{w}}} = \{E_{pq}\}\mathbf{a} \tag{4.39}$$

where $\underline{\tilde{\mathbf{w}}} = \left[\underline{\tilde{w}}_A \quad \underline{\tilde{v}}_A \quad \underline{\psi}_A \quad \underline{\tilde{w}}_B \quad \underline{\tilde{v}}_B \quad \underline{\psi}_B\right]^{\mathrm{T}}$, $\underline{\mathbf{a}} = \left[A_1 \quad \cdots \quad A_6\right]^{\mathrm{T}}$ and the element E_{pq} of the p^{th} row and q^{th} column of the matrix $\{E_{pq}\}$ is given by:

$$E_{1q} = 1, \quad E_{2q} = R_q, \quad E_{3q} = -\mathrm{j}\tilde{k}_q, \quad E_{pq} = \mathrm{e}^{-\mathrm{j}\tilde{k}_q}E_{(p-3)q} \qquad (p = 4,5,6, \quad q = 1\ldots6) \tag{4.40a-d}$$

Exact expressions relating the shear force Q, tensile force N and bending moment M to the deformation in a cylindrical shell are given by Flügge [25] and are specialised for the present case of a curved beam thus:

$$\frac{\tilde{M}}{\pi^2} = \frac{\partial^2\tilde{w}}{\partial\varsigma^2} + \alpha^2\tilde{w}, \qquad \frac{\tilde{Q}}{\pi^2} = \frac{\partial^3\tilde{w}}{\partial\varsigma^3} + \alpha^2\frac{\partial\tilde{w}}{\partial\varsigma} \tag{4.41a,b}$$

$$\frac{\tilde{N}}{\pi^2} = \left(\frac{S}{r}\right)^2\left(\frac{\partial\tilde{v}}{\partial\varsigma} + \alpha\tilde{w}\right) + \alpha\left(\alpha^2\tilde{w} + \frac{\partial^2\tilde{w}}{\partial\varsigma^2}\right) \tag{4.41c}$$

where the bending moment M and the general force F have been non-dimensionalised thus:

$$\tilde{M} = M/(P_E S), \quad \tilde{F} = F/P_E \tag{4.42a,b}$$

where $P_E = \pi^2 EI/S^2$. Applying the force/displacement boundary conditions using eqs. (4.41) and eqs. (4.37) yields:

$$\underline{\tilde{\mathbf{f}}}_w = \{G_{pq}\}\mathbf{a} \tag{4.43}$$

where $\underline{\tilde{\mathbf{f}}}_w = \left[\underline{\tilde{F}}_{wA} \quad \underline{\tilde{F}}_{vA} \quad \underline{\tilde{M}}_A \quad \underline{\tilde{F}}_{wB} \quad \underline{\tilde{F}}_{vB} \quad \underline{\tilde{M}}_B\right]^{\mathrm{T}}$ and

$$G_{1q}/\pi^2 = \mathrm{j}\left(\tilde{k}_q^3 - \alpha^2\tilde{k}_q\right) \qquad (q = 1\ldots6) \tag{4.44a}$$

$$G_{2q}/\pi^2 = \left(\mathrm{j}\tilde{k}_q R_q - \alpha\right)(S/r)^2 - \alpha^3 + \alpha\tilde{k}_q^2 \qquad (q = 1\ldots6) \tag{4.44b}$$

$$G_{3q}/\pi^2 = \tilde{k}_q^2 - \alpha^2 \qquad (q = 1\ldots6) \tag{4.44c}$$

$$G_{pq} = -\mathrm{e}^{-\mathrm{j}\tilde{k}_q} G_{(p-3)\,q} \qquad (p = 4,5,6, \quad q = 1\ldots6) \tag{4.44d}$$

Eliminating **a** from eqs. (4.39) and (4.43) and transforming from the local frame of reference in Figure 4.10(a) to the global frame of reference in Figure 4.10(b) yields the dynamic stiffness matrix $\tilde{\mathbf{D}}$ where

$$\underline{\tilde{\mathbf{f}}} = \tilde{\mathbf{D}}\underline{\tilde{\mathbf{x}}} \tag{4.45}$$

$\underline{\tilde{\mathbf{f}}} = \left[\underline{\tilde{F}}_{xA} \quad \underline{\tilde{F}}_{yA} \quad \underline{\tilde{M}}_A \quad \underline{\tilde{F}}_{xB} \quad \underline{\tilde{F}}_{yB} \quad \underline{\tilde{M}}_B\right]^{\mathrm{T}}$, $\underline{\tilde{\mathbf{x}}} = \left[\underline{\tilde{x}}_A \quad \underline{\tilde{y}}_A \quad \underline{\psi}_A \quad \underline{\tilde{x}}_B \quad \underline{\tilde{y}}_B \quad \underline{\psi}_B\right]^{\mathrm{T}}$ where $\tilde{x}_a = x_a/S, \ldots$etc., and

$$\tilde{\mathbf{D}} = \mathbf{T}\{G_{pq}\}\{E_{pq}\}^{-1}\mathbf{T}^{-1} \tag{4.46}$$

where

$$\mathbf{T} = \begin{bmatrix} -\sin\theta_A & \cos\theta_A & 0 & 0 & 0 & 0 \\ \cos\theta_A & \sin\theta_A & 0 & 0 & 0 & 0 \\ 0 & 0 & 1 & 0 & 0 & 0 \\ 0 & 0 & 0 & -\sin\theta_B & \cos\theta_B & 0 \\ 0 & 0 & 0 & \cos\theta_B & \sin\theta_B & 0 \\ 0 & 0 & 0 & 0 & 0 & 1 \end{bmatrix} \tag{4.47}$$

With reference to Figure 4.11, for a TVA beam with absorber mass m (per beam) attached, there are no moments at the ends and $\tilde{y}_A = \tilde{y}_B = 0$ and so the dynamic stiffness matrix of the TVA per beam, $\tilde{\mathbf{D}}_{TVA}$, is a 2×2 matrix given by:

$$\begin{bmatrix} \tilde{F}_{xA} \\ \tilde{F}_{yB} \end{bmatrix} = \tilde{\mathbf{D}}_{TVA} \begin{bmatrix} \tilde{x}_A \\ \tilde{y}_B \end{bmatrix} \tag{4.48}$$

where

$$\tilde{\mathbf{D}}_{TVA} = \tilde{\mathbf{D}}_{red} + \begin{bmatrix} 0 & 0 \\ 0 & -\pi^2\tilde{\omega}^2\tilde{m} \end{bmatrix} \tag{4.49}$$

where

$$\tilde{m} = (\text{attached absorber mass per beam})/(\text{mass of one beam}) = m/(\gamma S) \qquad (4.50)$$

and $\tilde{\mathbf{D}}_{red}$ is the reduced dynamic stiffness matrix of the TVA beam, obtained from $\tilde{\mathbf{D}}$ (eq. (4.46)) as follows:

i. Delete the third and sixth rows and columns from $\tilde{\mathbf{D}}^{-1}$

ii. Invert the resulting 4×4 matrix and delete the second and fourth rows and columns.

It is also noted that for the TVA beam in Figure 4.11, $\theta_A = -\theta_B = \alpha/2$ in eq. (4.46). The non-dimensional receptance matrix of the TVA per beam is then given by

$$\{\tilde{\alpha}_{pq}\} = \tilde{\mathbf{D}}_{TVA}^{-1} \qquad (4.51)$$

The dimensional receptances of the TVA per beam are given by:

$$\alpha_{pq} = (P_E/S)\tilde{\alpha}_{pq} \qquad (4.52)$$

and the receptances of the complete TVA are given by dividing eqs. (4.51) or (4.52) by the number of beams used. Note that the receptances $\tilde{\alpha}_{pq}$ are functions of $\tilde{\omega}$, α, S/r and $\tilde{m}$:

$$\tilde{\alpha}_{pq} = \tilde{\alpha}_{pq}(\tilde{\omega}, \alpha, S/r, \tilde{m}) \qquad (4.53)$$

The above theory was validated by comparing the results obtained for the input receptance $\tilde{\alpha}_{11}$ with those obtained by the Finite Element (FE) Method using shell elements (ANSYS® with SHELL 93 elements [15]). In Figure 4.12, the edges of the circular arch parallel to the z axis are constrained to move in the xz plane. In these calculations the attached mass $\tilde{m} = 0$. The actual dimensions shown in Figure 4.12 and the material properties (steel, $E = 200\,\text{GPa}$) were only required for the FE calculation (cf. eq. (4.53)). Figure 4.13 shows that there is very good agreement between the two methods.

If the last term in each of the expressions of eqs. (4.41) is dropped, Donnell's approximate expressions are obtained and eqs. (4.44a-c) are modified thus:

- eq. (4.44a): second term within brackets omitted
- eq. (4.44b): last two terms omitted
- eq. (4.44c): second term omitted

Donnell's expressions are quoted by Blevins [26] and are claimed to apply when $t/R >> 1$ (t, R being the shell thickness and radius of curvature respectively) or equivalently, $S/r >> \alpha$. The error introduced by Donnell's approximation for given S/r and increasing α is illustrated in Figure 4.14. The error results in the omission of the rigid body (0 Hz) resonance in $\tilde{\alpha}_{11}$ and its replacement by a spurious low frequency resonance which increases in frequency, becoming more prominent, as α is increased. Note the large error in Figure 4.14(b) despite the fact that α ($= \pi$) is still much smaller than S/r ($= 1438$).

The input receptance $\tilde{\alpha}_{11}$ is virtually insensitive to the value of S/r for no attached mass ($\tilde{m} = 0$), as seen in Figure 4.15. The attachment of mass results in $\tilde{\alpha}_{11}$ becoming sensitive to S/r at the higher frequencies, as shown in Figure 4.16, but the first anti-resonance, which defines the non-dimensional tuned frequency $\tilde{\omega}_t$ ($= \omega_t/\omega_s$) of the TVA, remains virtually unaffected by S/r i.e.

$$\tilde{\omega}_t = \tilde{\omega}_t(\alpha, \tilde{m}) \tag{4.54}$$

Of course, $\tilde{\omega}_t$ is equal to the non-dimensional natural frequency of the TVA with its base (i.e. point of attachment to structure) blocked, as shown in Figure 4.17, which compares $\tilde{\alpha}_{11}$ with the input receptance $\tilde{\beta}$ (per beam) of the TVA with its base blocked:

$$\beta = \left.\frac{x_B}{F_{xB}}\right|_{x_a=0} \tag{4.55}$$

(see Figure 4.11). $\tilde{\beta}$ is the reciprocal of the element in the second row, second column of $\tilde{\mathbf{D}}_{TVA}$ (eq. (4.49)). If the TVA beam inertia is excluded, it is not difficult to show that:

$$\tilde{\beta}_{BInEx} = \frac{1}{\tilde{K} - (\pi\tilde{\omega})^2 \tilde{m}} \tag{4.56}$$

where $\tilde{K}$ is given by eq. (4.1). Figure 4.18 compares $\tilde{\beta}$ with $\tilde{\beta}_{BInEx}$ for the prototype parameters $\alpha_{ref} = 38\pi/180$, $\tilde{m} = 15$. Figure 4.19 shows the effect of beam inertia on the tuning characteristic of the TVA. The tuned frequency of the fictitious massless beam TVA increases without bound as the beams straighten. The tuned frequency of the actual TVA has an upper limit of ω_s. Also included in Figure 4.19 is the tuning characteristic of the TVA without any absorber mass attached (i.e. TVA relying on beam inertia only). It is seen that the tuned frequency is virtually constant at ω_s. The dotted curve in Figure 4.19 is shown expanded in Figure 4.20 for a wider range of α. It is seen that considerable curvature is necessary to achieve some variation in the tuned frequency of the curved beam alone.

4.4 Tests on Prototype

This section describes a prototype ATVA based on the design concept of Figure 4.1 and a series of simulated and experimental tests of its performance. Figure 4.21 shows a picture of the prototype ATVA. Each curved beam is a piezoactuator (THUNDER® TH –7R) consisting of a piezoceramic layer 0.25 mm thick sandwiched between a 0.15 mm thick aluminium layer and a 0.2 mm thick steel plate. The beams are supported on miniature ball bearings (SKF 618/4) at their ends, allowing

freedom of rotation. The absorber mass is guided in the direction of vibration by a linear bearing running on the central column that is fixed to the base.

The piezoactuators can take between –300V to +600V dc [27], however the experiments described in this report were restricted to a voltage range of –280V to +480V dc. Figure 4.22 shows the estimated variation of the subtended angle α with applied dc voltage. This graph was derived from the experimental voltage-deflection characteristic provided by the manufacturer [27], which was obtained at 1 Hz ac from 0 to 600V peak-peak voltage. Hence, the angle-voltage characteristic of Figure 4.22 is restricted to the range –300V to +300V dc. The derivation of the data in Figure 4.22 is described in Appendix 5.

The fundamental frequency of lateral vibrations of each curved beam due to its own inertia alone, with boundary conditions as in Figure 4.21 and at zero applied voltage (subtended angle $\alpha = 38\pi/180$), is quoted in [27] as 100 Hz. According to Figure 4.19, this value can be taken for the frequency ω_s, defined in eq. (4.33), and marking the upper limit of operation of the ATVA.

4.4.1 Tuning characteristic and vibration control test parameters

Figure 4.23 shows the experimental set-up for the determination of the variation of the tuned frequency f_t with dc voltage applied to the actuators. For each voltage setting, random excitation was applied and the transmissibility T, relating the acceleration of the absorber mass $a_2(t)$ to the acceleration $a_1(t)$ at the TVA base, was measured. Assuming a linear relationship between these two signals:

$$T = \frac{A_2}{A_1} = \frac{1 + \mathrm{j}\eta}{1 - (f/f_t)^2 + \mathrm{j}\eta} \tag{4.57}$$

where η is the damping loss factor of the stiffness element, f is the frequency and A_1 and A_2 are the complex amplitudes of $a_1(t)$ and $a_2(t)$ for harmonic vibration i.e. when $a_r(t) = \mathrm{Re}\{A_r \mathrm{e}^{\mathrm{j}2\pi ft}\}$, $r = 1, 2$. $|T|$ is maximum at $f = f_t$ and f_t and η were accurately located by considering that at this point, $\mathrm{Re}\{T\} = 1$ and $\mathrm{Im}\{T\} = -1/\eta$. At low vibration amplitudes, the lowest measured value of f_t (at –280 V) was 36 Hz and the highest 56 Hz (at +480 V), with the value of f_t at 0 V being 42 Hz. The corresponding frequencies at seven times the vibration amplitude were only slightly changed (36, 55 and 41 Hz respectively). The transmissibility at this level of excitation remained described by eq. (4.57), as shown in Figure 4.24, where the solid line shows the measured T and the dashed line shows the function described by equation (4) using the measured values of f_t and η. The measured values of η ranged from 0.15 at very low amplitudes to 0.06 at high amplitudes. As

shown in Figure 4.24, the cosine of the phase ϕ between a_1 and a_2 is approximately zero at $f = f_t$. This agrees with eq. (4.57) and this condition is used as the tuning criterion by the adaptive control system discussed in the following section.

Figure 4.25 shows the percentage variation in f_t with applied voltage. The prediction that neglects the beam inertia effect was obtained by using eq. (4.20), the $\widetilde{K}$ - α relation of eq. (4.1) and the α-voltage graph of Figure 4.22. It had been established in section 4.2.1 that the static load due to absorber mass need not be considered in deriving this tuning characteristic. Figure 4.25 also shows the predicted tuning characteristic with the beam inertia effect included. This was obtained by computing the first resonance of the receptance $\widetilde{\beta}$ (eq.(4.55)) over a range of α. It should be noted that in this case, the extent of the influence of the static load on the tuned frequency was not quantified. Nonetheless, both methods show reasonably good agreement with measurement and it is seen that the maximum measured variation in f_t is almost 50%.

As shown in Figure 4.26, a hysteresis effect was observed when decreasing the voltage from +200V to -200V and back to +200V. This resulted in a reduced tuned frequency at zero voltage (38 Hz) on the return leg of the loop. The original value of the tuned frequency was only recoverable by exposure to a +200V voltage. Further experiments showed that exposure to voltages exceeding +450V had the effect of increasing the tuned frequency at zero voltage to as much as 45 Hz, which was restored to 41 Hz after exposure to a negative voltage of around -200V. The increase (decrease) in the tuned frequency at zero voltage, f_{t0}, as a result of exposure to positive (negative) voltage of high magnitude is referred to in this report as "residual stiffening" ("softening"). The negative voltage part of the measured tuning characteristic in Figure 4.25 was obtained by measuring the transmissibility for decreasing voltages from zero. The tuned frequency at zero voltage was then reset and the positive voltage part of the graph obtained by measuring the transmissibility for voltages increasing from zero.

Figure 4.27 shows a linear two degree-of-freedom model of the TVA-shaker combination. In this figure, m_2 is the effective absorber mass, m_1 is the "host structure" mass, comprising the effective armature mass and the redundant TVA mass and K_{Sh} and η_{Sh} are the armature suspension stiffness and damping loss factor respectively. The excitation force $F(t)$ is the electro-magnetic force on the armature. This was proportional to the current signal $I_{Sh}(t)$ supplied to the shaker, which was verified to be proportional to the voltage signal ("excitation signal") $V_S(t)$ from the signal generator. The accelerance function relating $a_1(t)$ to $F(t)$ was therefore proportional to the frequency response function (FRF) relating the acceleration $a_1(t)$ to $V_S(t)$ or $I_{Sh}(t)$. Figure 4.28

shows the latter FRF, $A_{a_1 I_{Sh}}$, for zero voltage applied to the piezo-actuators. By measuring this FRF in addition to T and using the method described in the Appendix 6, it was possible to estimate the mass ratio $\mu = m_2/m_1$ and the armature parameters $\omega_{Sh} = \sqrt{K_{Sh}/m_{Sh}}$ and η_{Sh}. The TVA-shaker combination parameters are given in Table 4.1, where the TVA parameters f_{t0}, η_0 are the TVA tuned frequency and loss factor for zero voltage applied to the piezo-actuators and at the higher level of excitation referred to in Figure 4.25.

μ	0.32
$f_{t0} = \omega_{t0}/(2\pi)$	41 Hz
η_0	0.06
$\omega_{Sh}/(2\pi) = \left(\sqrt{K_{Sh}/m_{Sh}}\right)/(2\pi)$	26 Hz
η_{Sh}	0.1

Table 4.1: Parameters of 2-degree-of-freedom model of Figure

4.4.2 Vibration control tests - overview

Figure 4.29 shows the ATVA set up for vibration control tests. In these tests, the system was subjected to a harmonic excitation of time-varying frequency f and the ability of the ATVA to maintain the tuned condition $f_t = f$ in real time was assessed. The frequency variation was given by:

$$f = \begin{cases} f_i & t \le t_i \\ f_i + \left[\left(f_f - f_i\right)/\left(t_f - t_i\right)\right]\left(t - t_i\right) & t_i < t < t_f \\ f_f & t \ge t_f \end{cases} \tag{4.58}$$

The excitation signal $V_S(t)$ was:

$$V_S(t) = A_S \sin\theta \tag{4.59}$$

where A_S is constant and

$$2\pi f = \frac{d\theta}{dt} \tag{4.60}$$

and, by substituting for f from eq. (4.58) into eq. (4.60) and integrating:

$$\frac{\theta}{2\pi}=\begin{cases} f_i t & t \le t_i \\ 0.5\left[\left(f_f - f_i\right)/\left(t_f - t_i\right)\right]\left(t - t_i\right)^2 + f_i t & t_i < t < t_f \\ f_f t - 0.5\left[\left(f_f - f_i\right)/\left(t_f + t_i\right)\right] & t \ge t_f \end{cases} \tag{4.61}$$

The inputs to the controller were the signals a_1, a_2 from the accelerometers. The instantaneous error signal $e(t)=\cos\phi$ was continuously evaluated from a_1, a_2 by integrating their normalised product over a sliding interval of fixed length T_c, according to the following formula, which is based on eq. (2.7):

$$e(t)=\cos\phi=\begin{cases} \dfrac{I_{12}(t)}{\{I_{11}(t)\}^{0.5}\{I_{22}(t)\}^{0.5}} & (t \le T_c) \\ \dfrac{I_{12}(t)-I_{12}(t-T_c)}{\{I_{11}(t)-I_{11}(t-T_c)\}^{0.5}\{I_{22}(t)-I_{22}(t-T_c)\}^{0.5}} & (t > T_c) \end{cases} \tag{4.62}$$

where

$$I_{ij}(t)=\int_0^t a_i(\tau)\,a_j(\tau)\,d\tau\,,\quad i,j=1,2 \tag{4.63}$$

Since the difference $f-f_t$ is non-linearly related to $e(t)$, a non-linear control law is necessary. The voltage V applied to the piezoactuators was updated at the sample times t_n $(n=0,1,2.....)$ according to the rule:

$$V_{n+1}=\begin{cases} V_{\min} & V_n-\left[P\left(e_n+e_n^3+e_n^5\right)+D\dot{e}_n\right] \le V_{\min} \\ V_n-\left[P\left(e_n+e_n^3+e_n^5\right)+D\dot{e}_n\right] & V_{\min} < V_n-\left[P\left(e_n+e_n^3+e_n^5\right)+D\dot{e}_n\right] < V_{\max} \\ V_{\max} & V_n-\left[P\left(e_n+e_n^3+e_n^5\right)+D\dot{e}_n\right] \ge V_{\max} \end{cases} \tag{4.64}$$

where $V_n=V(t_n)$, $e_n=e(t_n)$, $\dot{e}_n=\dot{e}(t_n)$, P and D are constants, $V_{\max}$, $V_{\min}$ are the maximum and minimum voltage limits and $t_0=0$, $V_0=0$.

The following sections describe simulated and experimental vibration control tests. In either case the sample time interval was constant at $\Delta=t_{n+1}-t_n=10^{-3}$ (1 kHz sampling frequency) and the interval $T_c=0.1$. All tests were conducted at a fixed amplitude of excitation roughly equal to half the peak-to-peak of the higher level of random excitation referred to in the measurements of Figure 4.25.

4.4.3 Simulated vibration control tests

The purpose of these simulations was to get a feel for suitable values of the control constants P and D. The simulation made use of the linear two degree-of-freedom model for the TVA-shaker combination (Figure 4.27), whose equations of motion are:

$$(1/\mu)\ddot{x}_1 + 2\zeta_0\omega_{t0}(\dot{x}_1 - \dot{x}_2) + \omega_t^2(V)(x_1 - x_2) + (2\zeta_{Sh}\omega_{Sh}/\mu)\dot{x}_1 + (\omega_{Sh}^2/\mu)x_1 = F(t)/m_2 \quad (4.65a)$$

$$\ddot{x}_2 + 2\zeta_0\omega_{t0}(\dot{x}_2 - \dot{x}_1) + \omega_t^2(V)(x_2 - x_1) = 0 \quad (4.65b)$$

where the excitation is given by

$$F(t)/m_2 = A_F \sin\theta \quad (4.66)$$

A_F is a constant and θ is given by eq. (4.61). In the above equations, the structural damping in both TVA and shaker armature suspension was accounted for by using equivalent damping factors $\zeta_0 = \eta_0/2$ and $\zeta_{Sh} = \eta_{Sh}/2$. Strictly speaking, these apply only for harmonic vibrations at circular frequencies $\omega = \omega_{t0}$, $\omega = \omega_{Sh}$ respectively, but, for simplicity, they are assumed to apply over the entire frequency range considered. The square of the circular tuned frequency as a function of actuator voltage, $\omega_t^2(V)$, was obtained from the experimentally determined characteristic of Figure 4.25. The control system was implemented in MATLAB® with SIMULINK® and is illustrated in Figures 4.30(a,b), which respectively show the overall system and the controller. In order to enhance the performance, the signals e and $\dot{e}$ were smoothened by filtering out frequencies in excess of 20 Hz (Figure 4.30(b)). This upper limit was deemed reasonable since the imposed rate of change of the excitation frequency did not exceed 10 Hz/s.

The excitation frequency was varied as shown in Figure 4.31(a). The amplitude A_F of the excitation $F(t)/m_2$ was chosen to give the same amplitude of $a_1(t)$ at 38 Hz with actuator applied voltage $V = 0$ as that measured under similar conditions. Figure 4.31(b) shows the vibration a_1 if no control is applied and with zero voltage applied to the piezoactuators. The vibration reaches a minimum as the excitation frequency sweeps through the tuned frequency at 0 V (f_{t0}) and $\cos\phi$ is very nearly zero at this instant (Figure 4.31(c)). Figure 4.31(d) shows the corresponding vibration with the control applied. It is seen that the vibration minimum of Figure 4.31(b) is maintained approximately at all times by maintaining $\cos\phi$ as close as possible to zero (Figure 4.31(c)). Figure 4.31(e) shows the voltage applied to the actuators being adjusted in real time. Figure 4.31(f) shows that the vibration of the absorber mass, a_2, which minimises the vibration of the host structure, a_1, by continuously absorbing it.

The tests in Figure 4.31 indicate that $P = 4\times10^{-2}$, $D = 2\times10^{-3}$ are suitable values for the control constants. As shown in Figure 4.32, the omission of D resulted only in a slightly increased

settling time for the controller to tune the ATVA from its initial tuned frequency $f_{t0} = 41$ Hz to the initial value of the excitation frequency $f_i = 38$ Hz. This is attributed to the significant amount of damping in the system. On the other hand, higher values of D resulted in oscillations about the tuned condition. It should be noted, however, that since the control is non-linear, the effect of D in this study is different from that in a linear P-D system. Figure 4.32 also shows that the value of D had negligible effect on the amplitude of a_1.

4.4.4 Experimental vibration control tests

The control system for the experimental set up of Figure 4.29 was implemented in MATLAB® with SIMULINK® using the Real Time Workshop® and Real Time Windows Target® toolboxes and is illustrated in Figure 4.33. The same controller in Figure 4.30(b) was used.

In the preliminary tests, the excitation frequency was restricted to a narrower range than used in the simulations, in order to avoid any potential residual softening or stiffening of the piezoactuators due to exposure to voltage of excessive magnitude (section 4.4.1). For the first test, the frequency was varied as in Figure 4.34(a). The response at a_1 without any control and the piezos at 0V is shown in Figure 4.34(b). The minimum in a_1 coincides with $\cos\phi \approx 0$ (dashed line in Figure 4.34(c)) and occurs when the excitation frequency f is close to f_{t0}. It is seen in Figure 4.34(a) that this frequency is close to the 41 Hz estimate determined from the transmissibility measurements (Table 4.1). Figure 4.34(d) shows the controlled vibration a_1, which is maintained at the minimum of Figure 4.34(b) by keeping $\cos\phi$ as close as possible to zero at all times (Figure 4.34(c)). Figure 4.34(e) shows the voltage applied to the piezos being adjusted in real time to maintain the tuned condition. All experimental control tests presented used empirically obtained optimal values $P = 4\times10^{-2}$ and $D = 8\times10^{-3}$. The optimal P value agrees with the simulation. The D value is higher but of the same order of magnitude. Moreover, oscillation about the tuned condition was observed for high values of D, as was depicted in the simulations of Figure 4.32(a).

Figure 4.35 shows that the ATVA performance remained satisfactory when the frequency gradient was raised to 3.5 Hz/s.

The test results in Figure 4.36 refer to the forcing frequency variation that was used in the simulations (see Figure 4.31(a)), covering almost the entire measured tuning range. Figure 4.36 shows that the performance is satisfactory and the measurements in Figure 4.36(a-e) compare favourably with the simulations in Figures 4.31(b-f). However, by comparing the positions of the zero crossings of the dashed curves in Figure 4.36(b) and Figure 4.31(c) (or the positions of the corresponding minima in a_1), it is seen that the tuned frequency at zero voltage f_{t0} is higher in the

measurement than in the simulation (which used the measured tuning characteristic of Figure 4.25, for which f_{t0} was 41 Hz). The reason for this is that exposure to a voltage in excess of +400V in a previous test resulted in residual stiffening of the beams. This stiffening made it somewhat harder for the ATVA to retune itself from f_{t0} to the initial value f_i of the excitation frequency (38 Hz) as can be seen by comparing the first 5 seconds of the solid curve in Figure 4.36(b) with the corresponding measurement in Figure 4.34(c). This effect became more pronounced when the tests were conducted after prolonged exposure of the piezos to highly positive voltage, as was the case for the tests illustrated in Figure 4.37. With reference to the first 5 seconds of the solid curves in Figures 4.37(c,e) it is evident that, due to the residual stiffening, a negative voltage of magnitude higher than normal was necessary to tune the ATVA from f_{t0} to f_i. This voltage was in fact below the allowable minimum (-280V) and so was clipped (Figure 4.37(e)). However, exposure to this highly negative voltage tended to neutralise the residual stiffening, as discussed in section 4.4.1, so that finally, at $t = 3$, the tuned condition was achieved at a negative voltage of lower magnitude. Despite this phenomenon, the overall performance of the ATVA in Figure 4.37 was still satisfactory, particularly with respect to its response to the very steep frequency gradient (7 Hz/s): the controlled vibration a_1 during the 2 s transient interval was still well below that which would have developed had no retuning been applied. Moreover, the residual stiffening phenomenon was only a problem when the ATVA was required to tune *suddenly* from f_{t0} to the forcing frequency of 38 Hz at the start of the control test. The ATVA had no problem tuning to this frequency when it was applied through a gradient after exposure to a highly positive voltage (Figure 4.38). In Figure 4.38, the ATVA is slightly residually softened at the start of the control test but still manages to retune itself from f_{t0} to $f_i = 52$ Hz fairly rapidly, taking about 1s to suppress the high vibration that would have developed without retuning (cf. Figures 4.38(b,d)).

4.4.5 Improvements to prototype

The vibration attenuation provided by the ATVA could be improved if the damping is reduced, resulting in a smaller vibration minimum in Figure 4.31(b). The transmissibility measurements of section 4.4.1 revealed that the loss factor varied from 0.15 at a very low level of excitation to 0.06 at seven times that level. The damping in the experimental vibration control tests was observed to be considerably lower than the latter estimate, as can be seen by comparing the minima of Figures 4.31(b) and 4.36(a), explaining the differing values in optimal value for derivative control constant D for simulation and measurement. The lower damping was due to fact that, although the peak-to-peak level of excitation was chosen to be similar for both vibration control tests and transmissibility

tests, the root mean square value of the former (sine) was much higher than the latter (random). The dependency of the damping on the level of excitation indicated that it was mostly of a Coulomb nature, originating from the linear bearing guiding the absorber mass (Figure 4.21). As far as practical usage is concerned, the highest recorded damping value (0.15) could be ignored since there is no point of using the ATVA to attenuate already miniscule levels of vibration. However, there is scope for reducing the lower damping loss factor of 0.06. Attempts were made at replacing the linear bearing by an alternative form of location with less damping. One such alternative was a flat slotted spring in the form of a disc that had negligible stiffness in the direction of vibration and high stiffness in the orthogonal direction, laterally locating the absorber mass (Figure 4.39). However, since the spring had no rotational stiffness in the plane of the vibration, the ATVA ended up with two interfering tuned frequencies that significantly degraded the performance.

One way of reducing the damping without altering the design in Figure 4.21 is to actively remove it by counteracting it, using the piezos to exert force proportional either to $\dot{x}_1 - \dot{x}_2$ or to $\dot{x}_2$ (Figure 4.27). The voltage supplied to the piezos will then have two components: an ac component at the vibration frequency (counteracting the damping) and a dc component that adjusts the tuned frequency. A similar technique was employed in [2] with respect to a beam-like ATVA.

4.5 Conclusions

This chapter described the design, development and testing of a novel adaptive tuned vibration absorber (ATVA) having a variable stiffness element formed from parallel beams of adjustable curvature vibrating longitudinally. The design principle was first illustrated using elementary analysis that neglected non-linearity and the effect of the inertia of the beams. A method was then developed to quantify the effects of the static load and non-linear vibration in any given application using non-dimensional parameters that are easily accessible to the designer. The dynamic stiffness method was used to analyse the effect of the inertia of curved beams and it was shown that the upper limit to the tuned frequency is the natural frequency of lateral vibrations of each of the straightened beams. The application of these analytical methods to the prototype ATVA with piezo-actuated beams predicted that the elementary analysis would be sufficient to determine the tuning characteristic, and a linear model would be adequate to predict its performance in the control of vibration. The vibration control tests used a non-linear *P-D* controller which tuned the ATVA continuously (i.e. at the sample frequency).

The predictions were validated by the experimental results. These tests additionally revealed residual stiffening or softening when the piezo-actuators were exposed to voltages of high magnitude. This only affected the ATVA performance adversely when it was required to tune

suddenly to a forcing frequency close to the limits of tuning imposed by the voltage restrictions. The tests demonstrated the efficacy of the proposed ATVA design in vibration control, particularly with respect to its agility in tracking rapidly varying forcing frequencies. The damping in the device was mostly due to the linear bearing used for guidance of the absorber mass. For most practical applications, this damping is deemed sufficiently small as not to adversely affect the vibration attenuation. However, if improved attenuation is required, it is proposed to use the piezo-actuators to actively remove the damping.

Figures

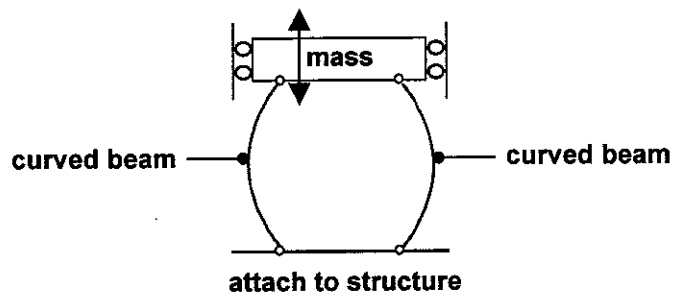

Figure 4.1: Vibration absorber with stiffness element formed from parallel curved beams

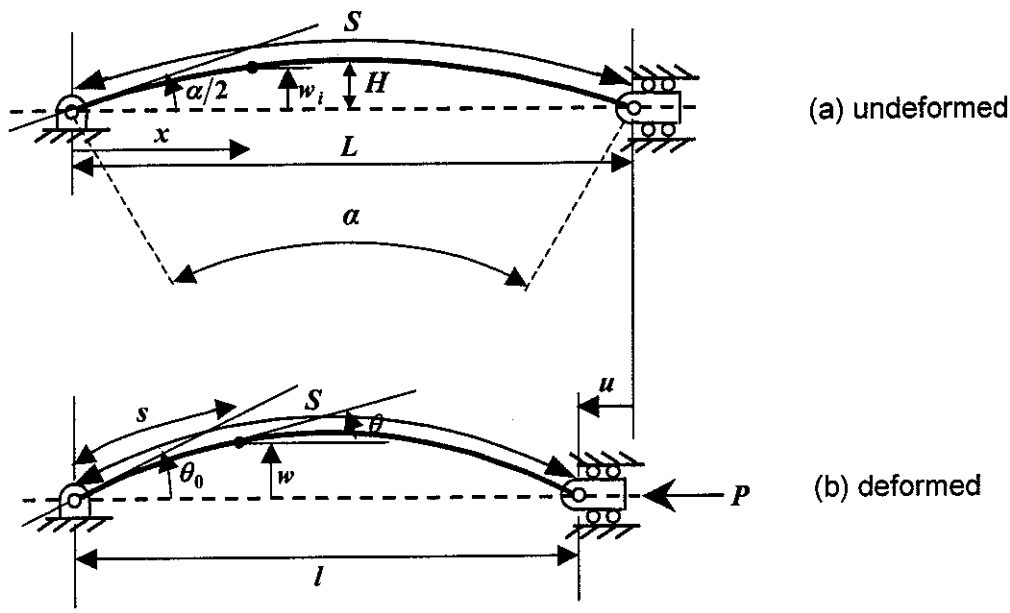

Figure 4.2: Curved beam loaded along its span

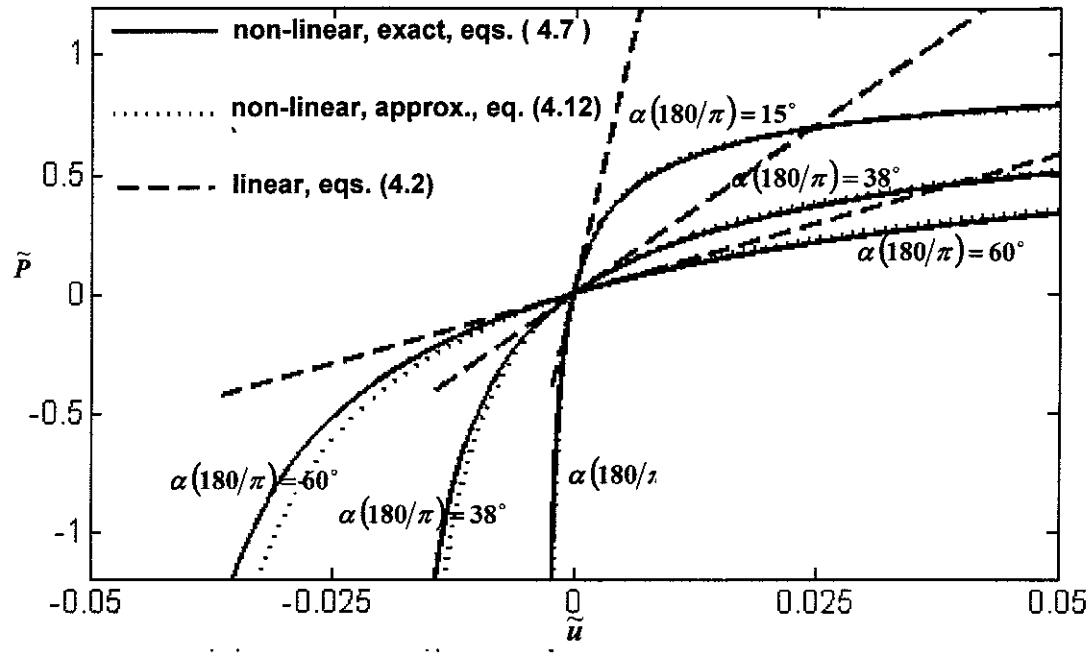

Figure 4.3: Non-linear $\tilde{P}-\tilde{u}$ characteristics

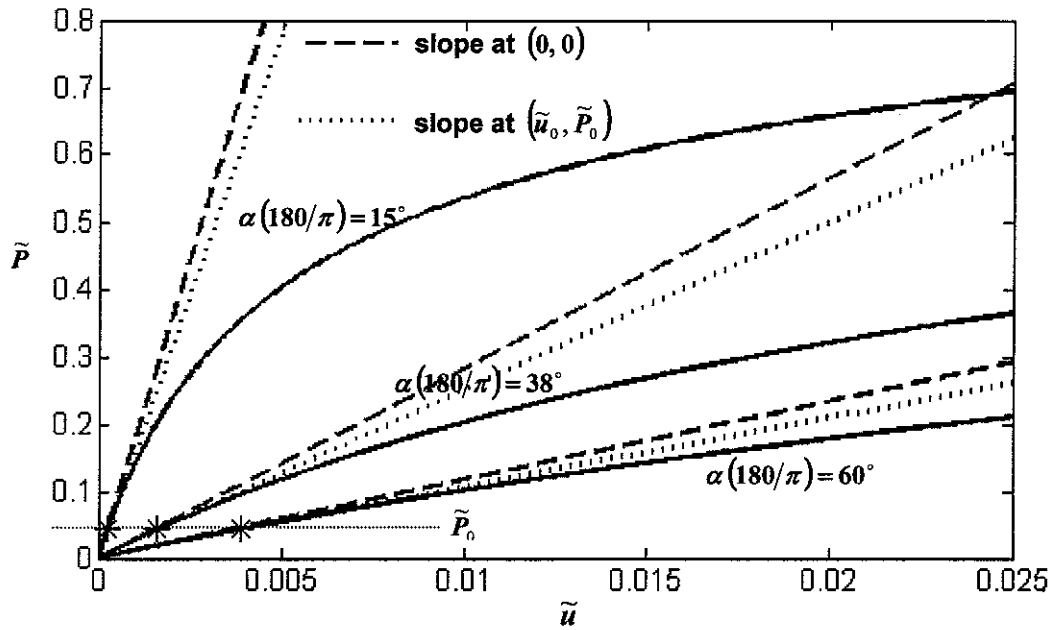

Figure 4.4: Effect of static load on stiffness

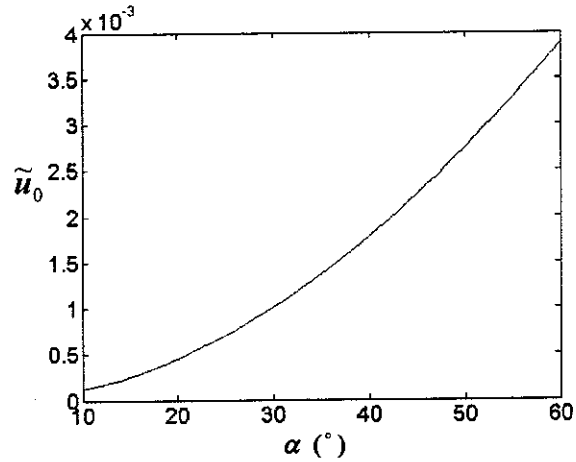

(a) static compression

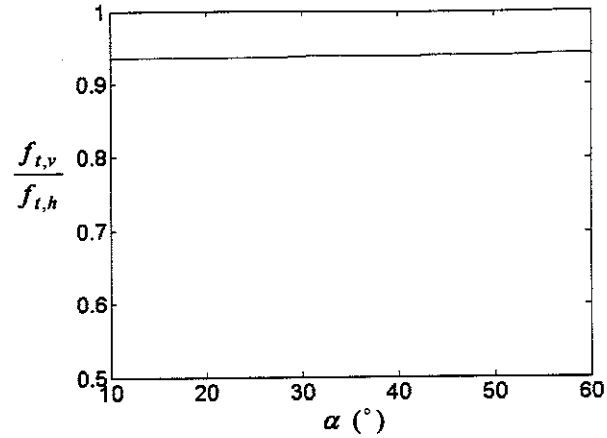

(b) reduction factor in tuned frequency

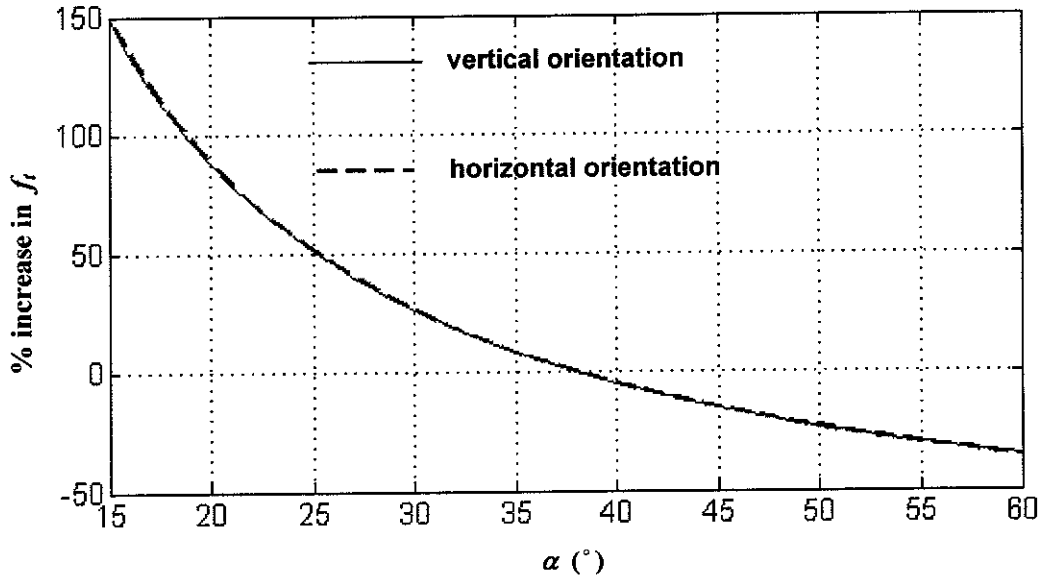

(c) tuning characteristic

Figure 4.5: Effect of static load on prototype ATVA

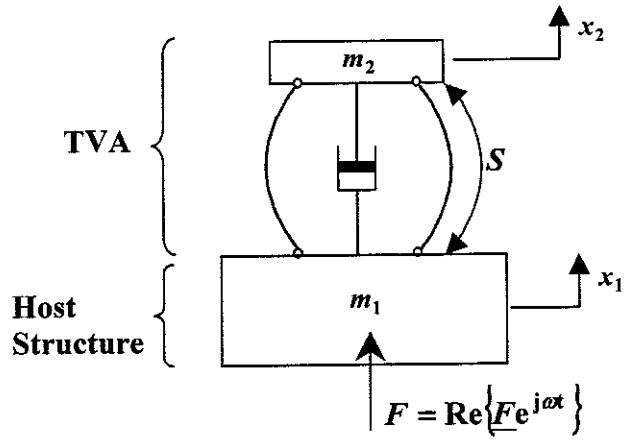

Figure 4.6:
TVA with mass-like host structure

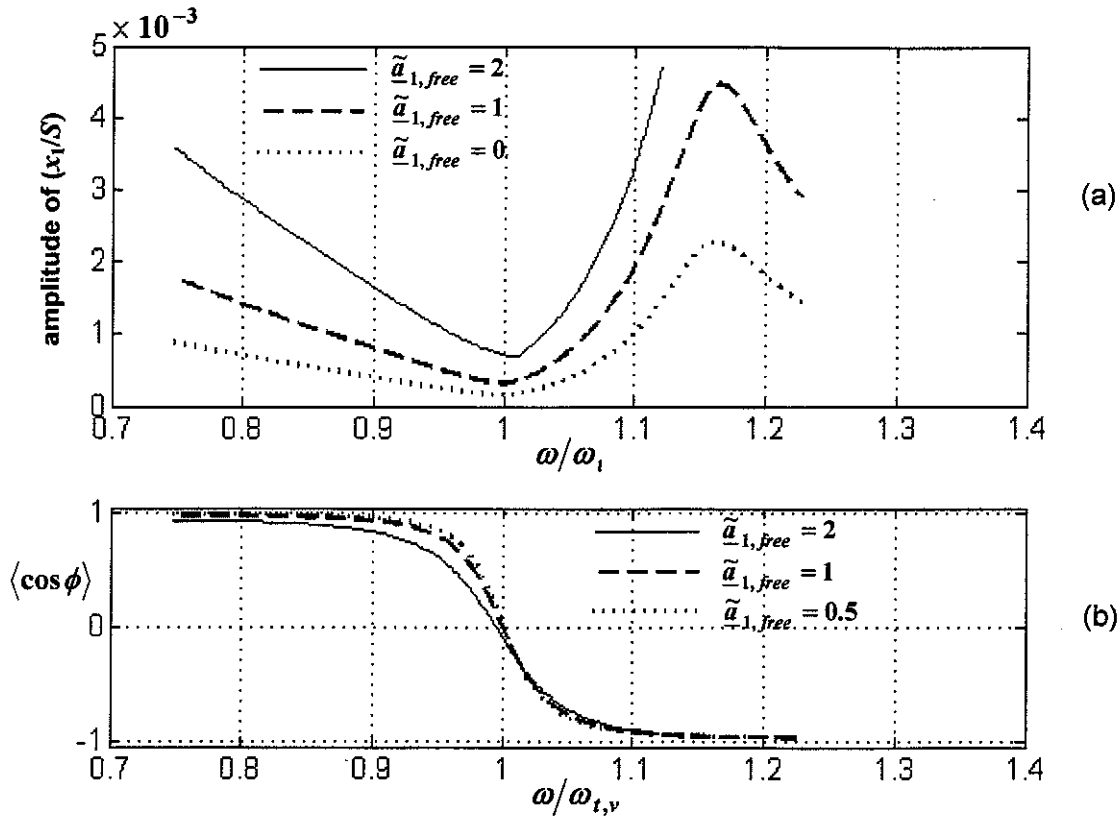

Figure 4.7: Non-linear vibration response for different levels of excitation of mass-like host structure: (a) amplitude; (b) "cosine of phase"

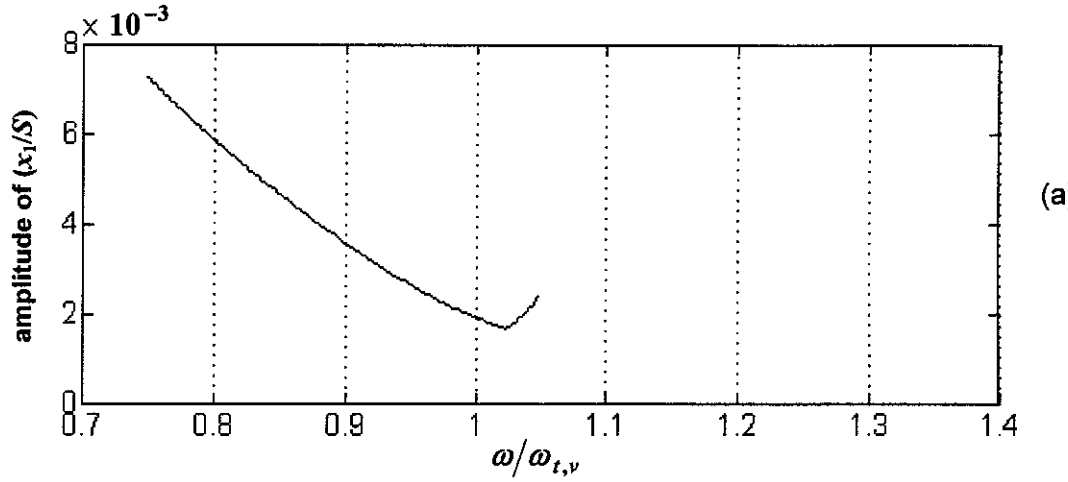

Figure 4.8: Non-linear vibration response of mass-like host structure for $\tilde{a}_{1,free} = 4$: (a) amplitude

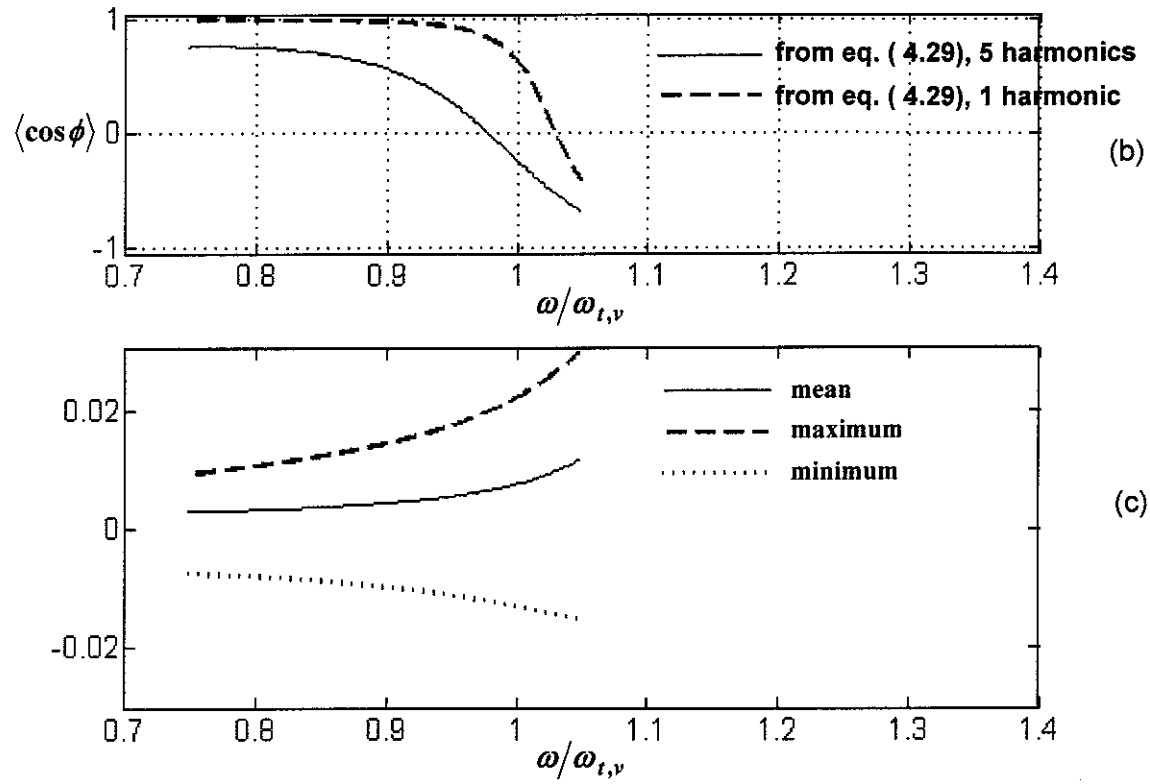

Figure 4.8 (cont'd.): Non-linear vibration response of mass-like host structure for $\tilde{a}_{1,free}=4$: (b) "cosine of phase"; (c) compression of stiffness element

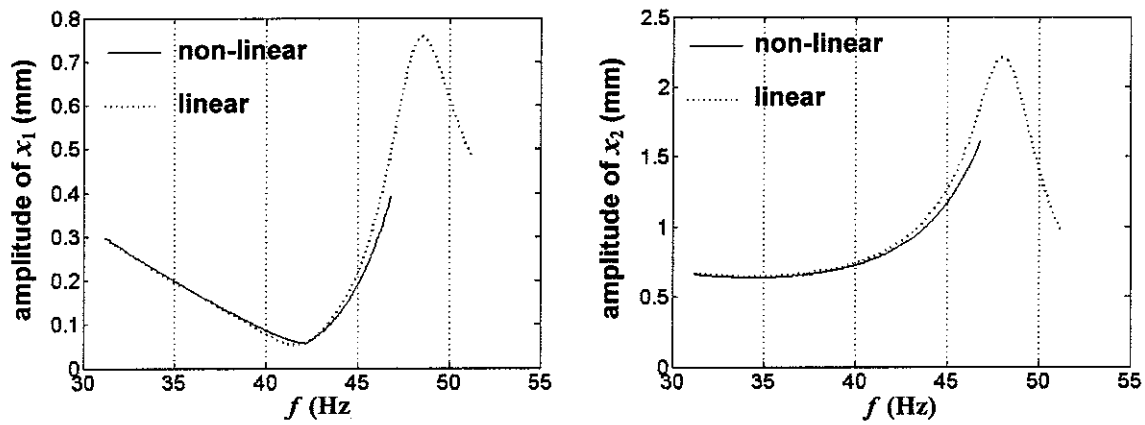

Figure 4.9: Dimensional displacement (x_1, x_2) and acceleration (a_1, a_2) amplitudes for $\tilde{a}_{1,free}=2$

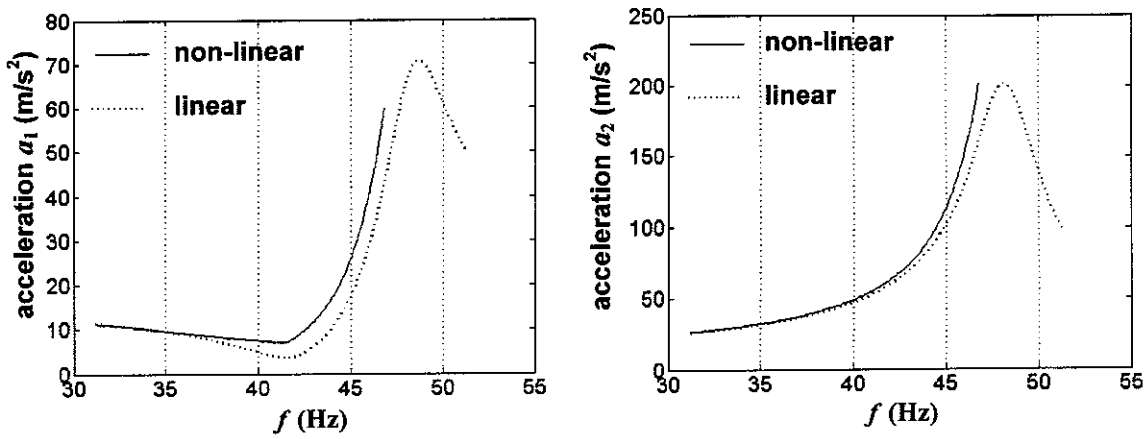

Figure 4.9 (cont'd.): Dimensional displacement (x_1, x_2) and acceleration (a_1, a_2) amplitudes for $\tilde{a}_{1,free} = 2$

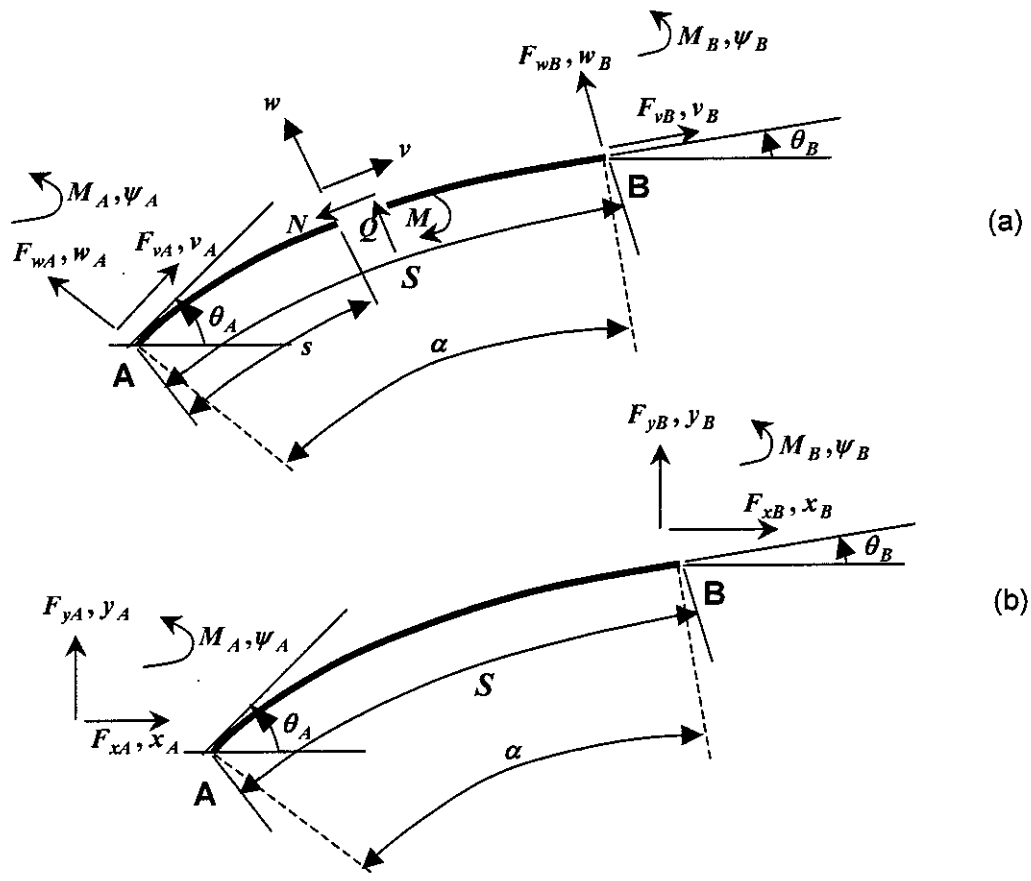

Figure 4.10: Dynamic stiffness analysis of segment of curved beam: (a) local frame of reference; (b) global frame of reference

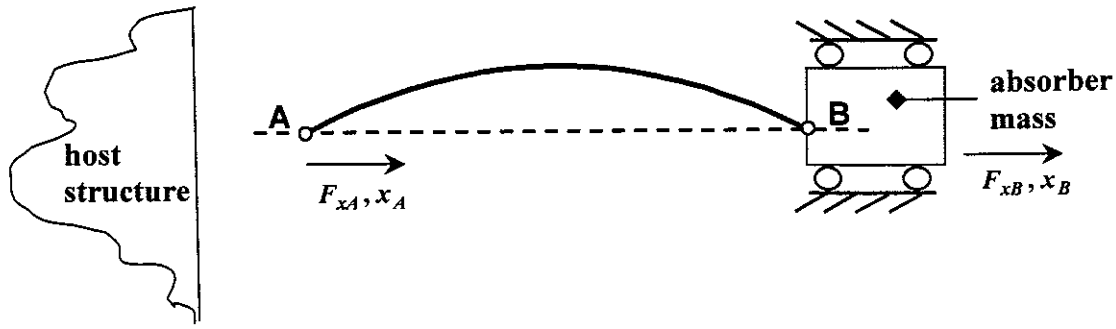

Figure 4.11: Dynamic stiffness analysis of TVA including inertia of beam

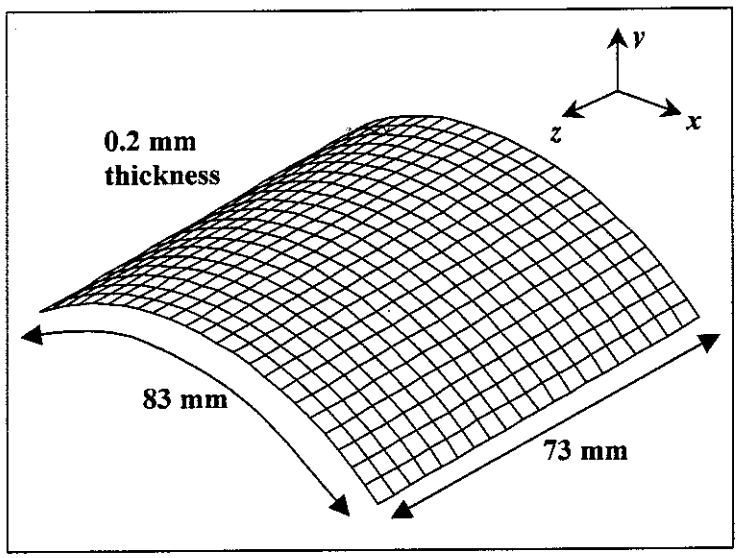

Figure 4.12:
Finite Element (FE) model of circular arch with no mass attached

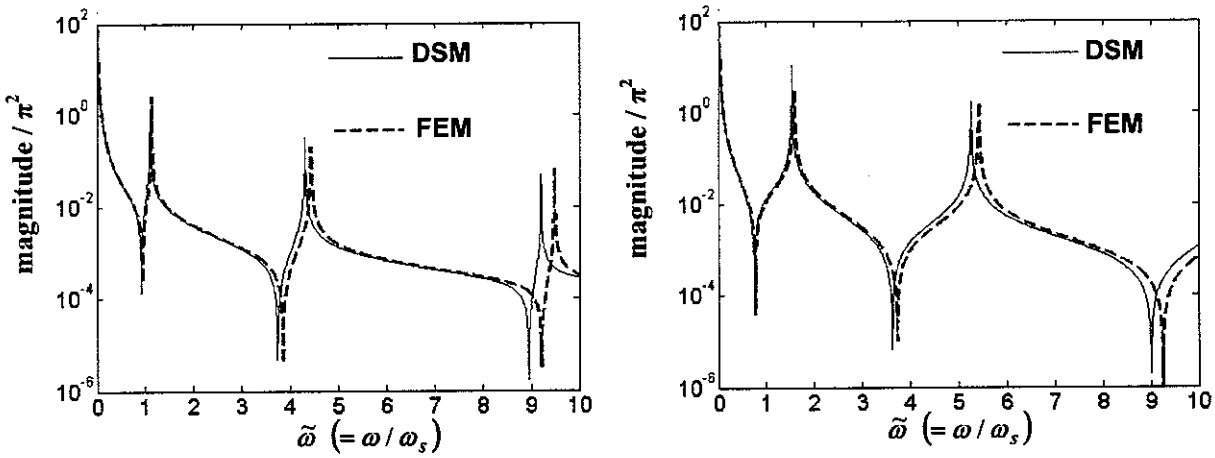

Figure 4.13: Comparison of $\tilde{\alpha}_{11}$ computation for arch in Figure 4.12 by dynamic stiffness method (DSM) and the Finite Element (FE) method

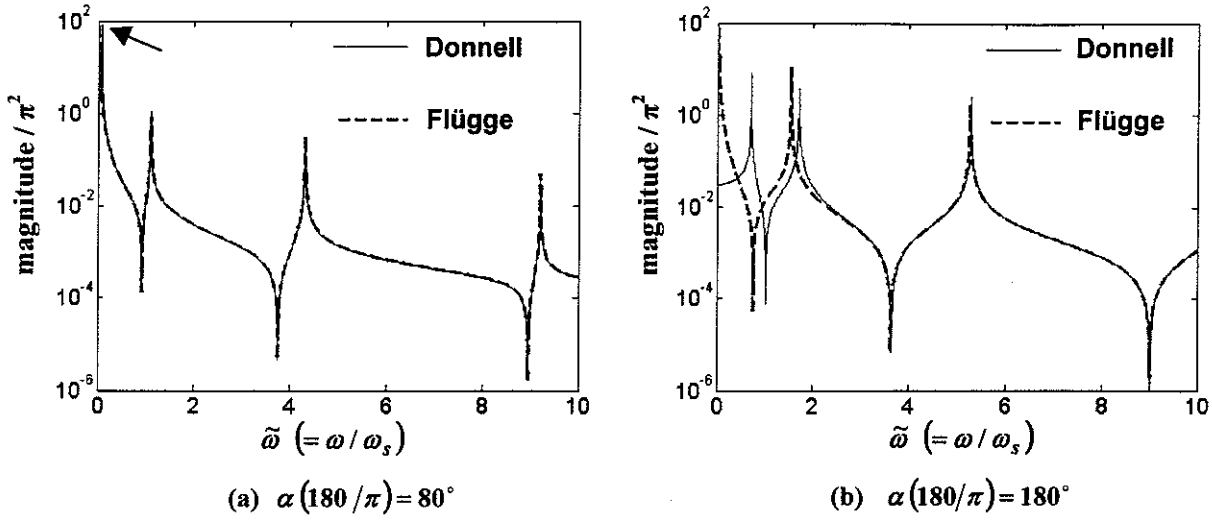

Figure 4.14: Comparison of dynamic stiffness computation of $\tilde{\alpha}_{11}$ for arch in Figure 4.12 by Flügge and Donnell's theories

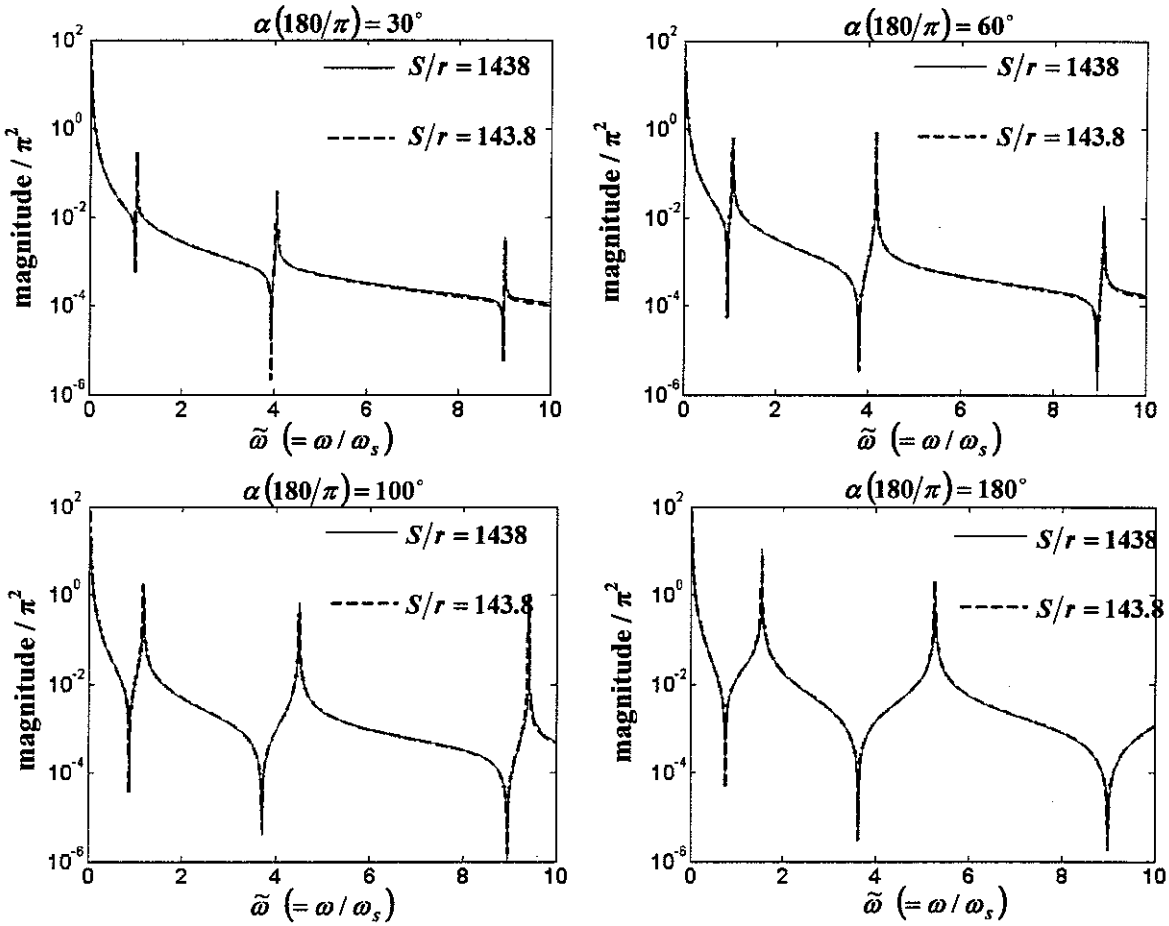

Figure 4.15: Influence of S/r on $\tilde{\alpha}_{11}$ for various angles α and $\tilde{m}=0$

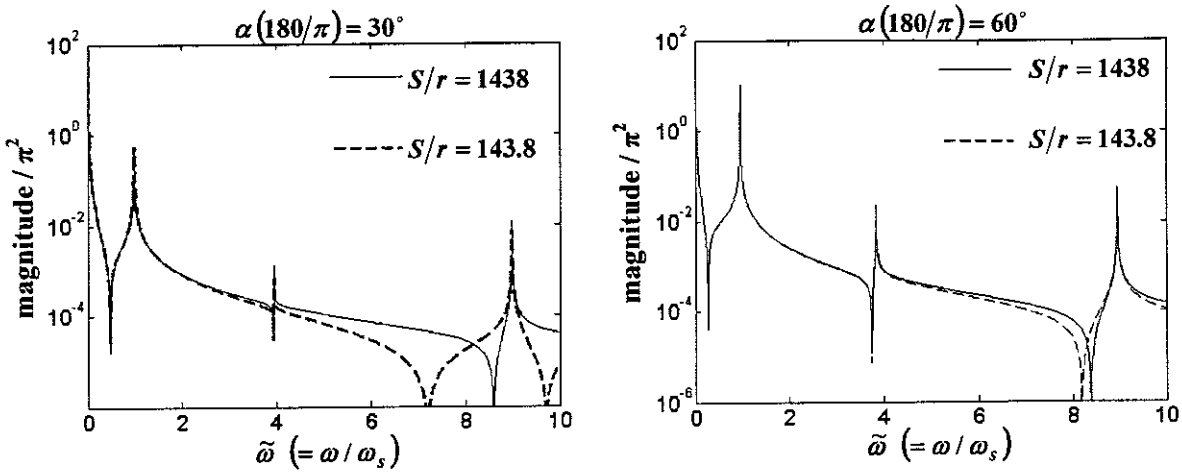

Figure 4.16: Influence of S/r on $\tilde{\alpha}_{11}$ for various angles α and $\tilde{m}=15$

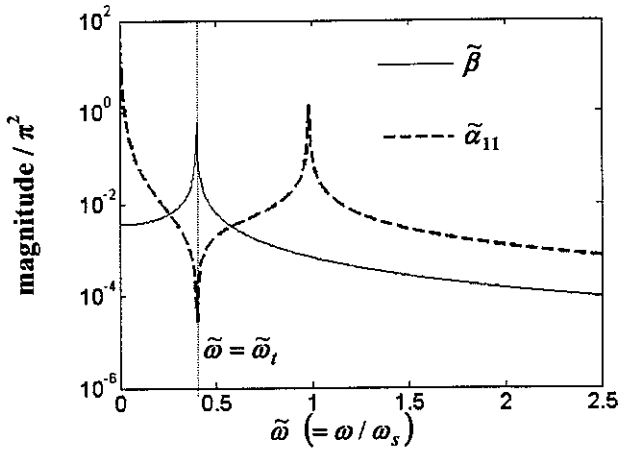

Figure 4.17: Input receptances of TVA $\tilde{\alpha}_{11}$ (base free to vibrate), $\tilde{\beta}$ (base blocked) $(\alpha(180/\pi)=38°,\ \tilde{m}=15)$

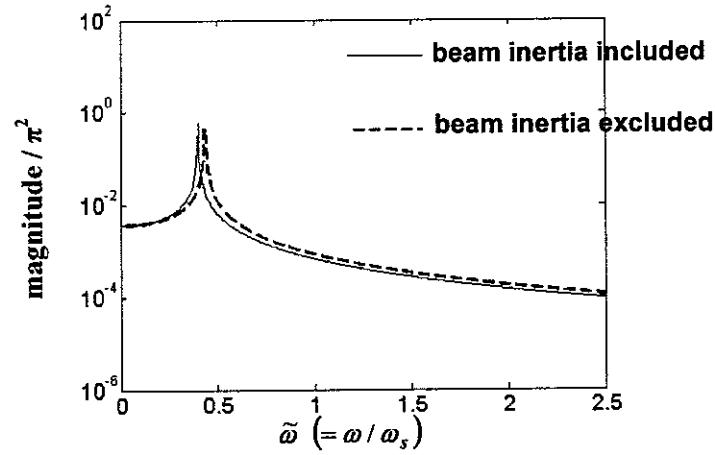

Figure 4.18: Effect of beam inertia on $\tilde{\beta}$ $(\alpha(180/\pi)=38°,\ \tilde{m}=15)$

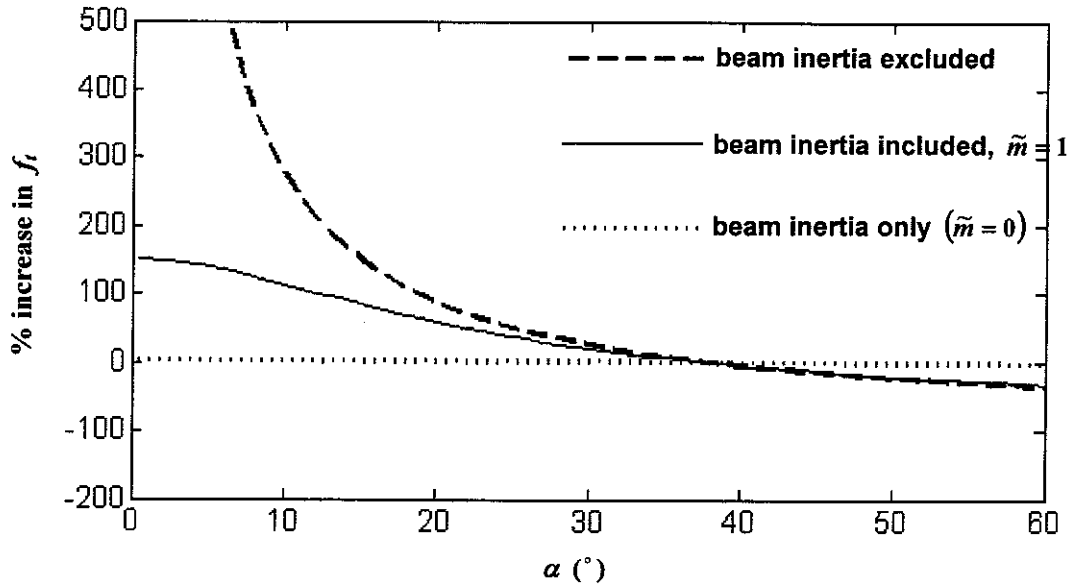

Figure 4.19: Effect of beam inertia on tuning characteristic

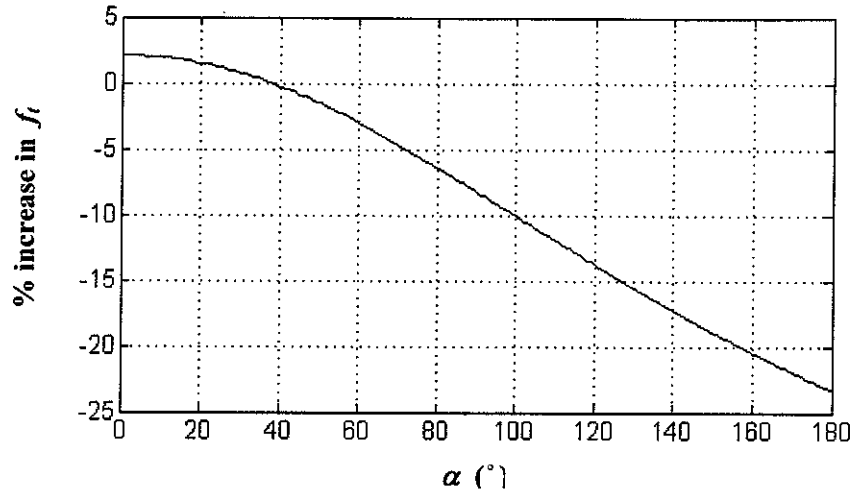

Figure 4.20: Tuning characteristic of TVA for no mass attached at end B, Figure 4.11 (i.e. $\tilde{m} = 0$)

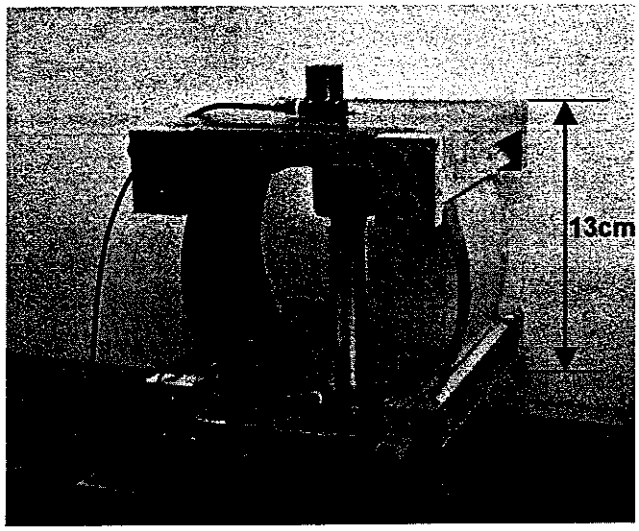

Figure 4.21: Prototype ATVA with variable curvature beams as stiffness element

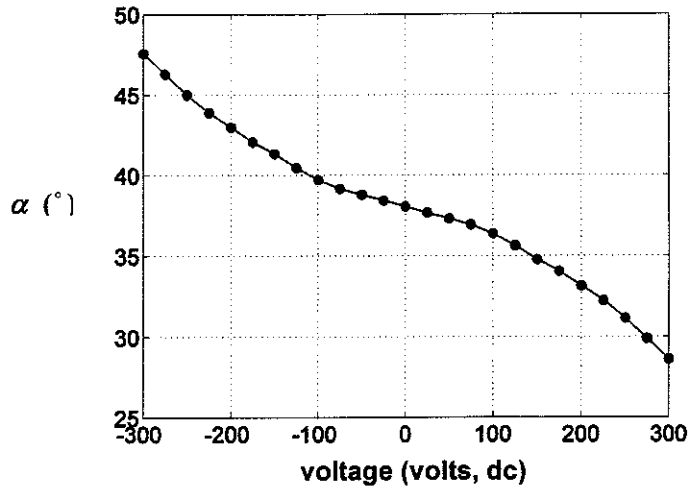

Figure 4.22: Estimated variation of subtended angle α with voltage applied to piezos

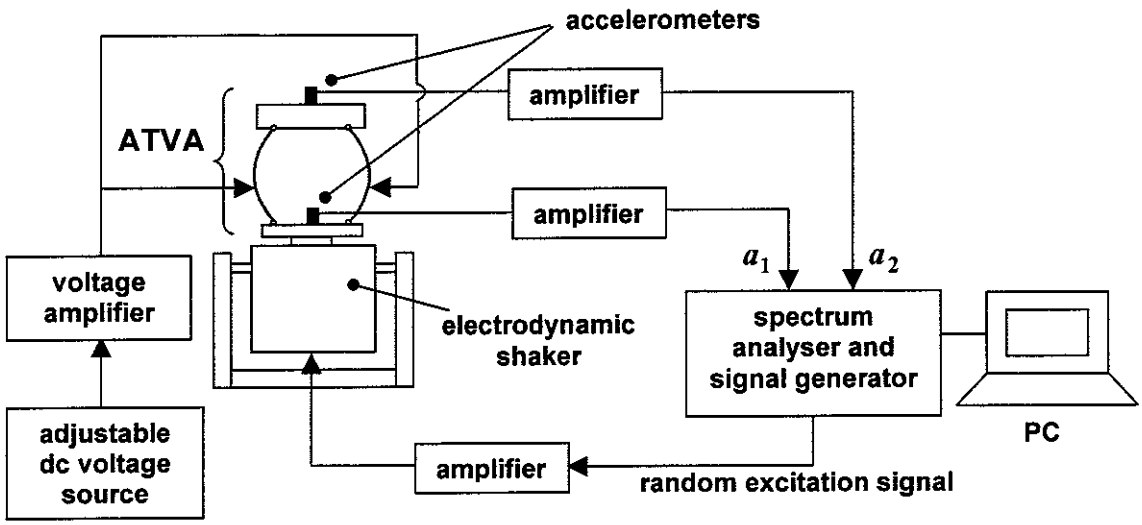

Figure 4.23: Experimental set-up for determination of tuning frequency characteristic of ATVA

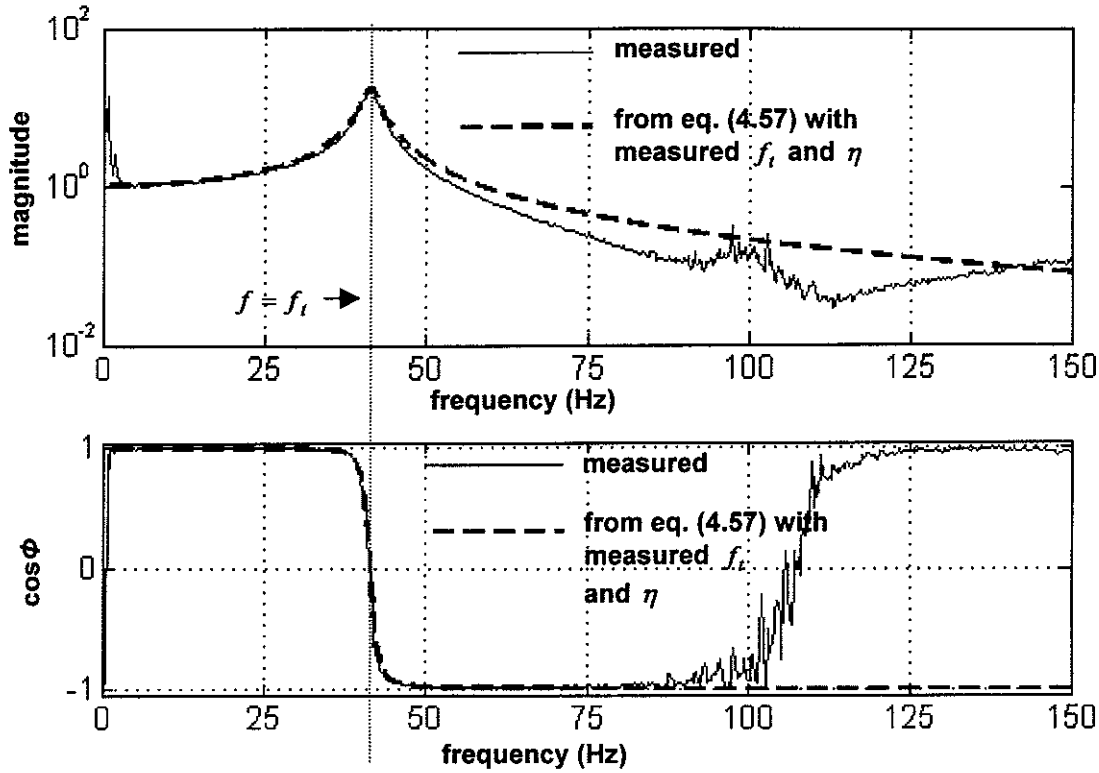

Figure 4.24: Typical transmissimility plot

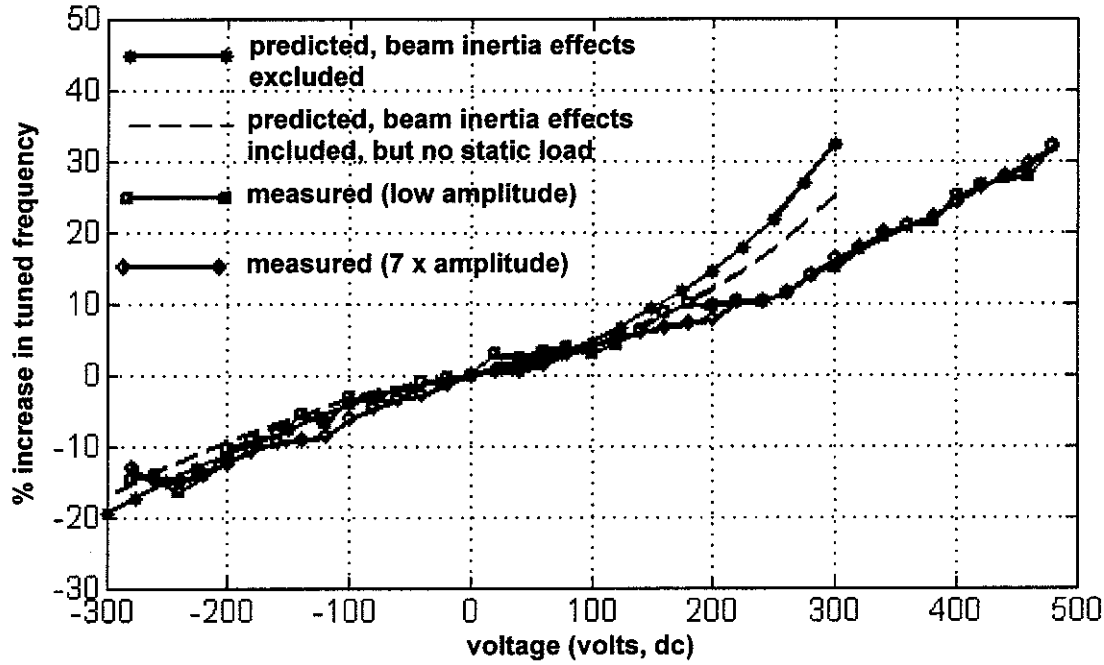

Figure 4.25: Tuning characteristic for prototype ATVA

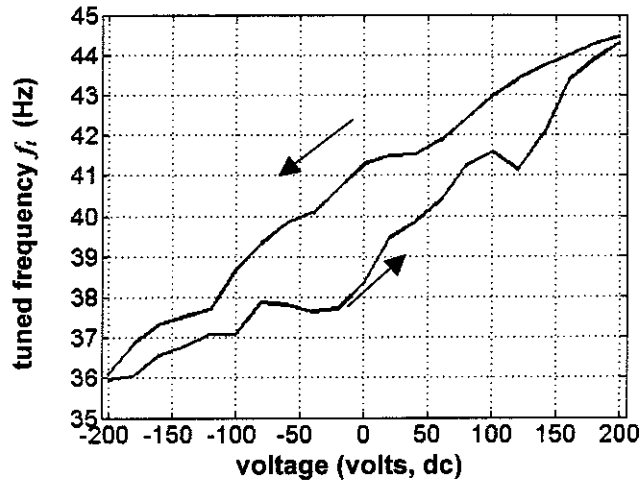

Figure 4.26: Observed hysterisis effect in piezoactuators

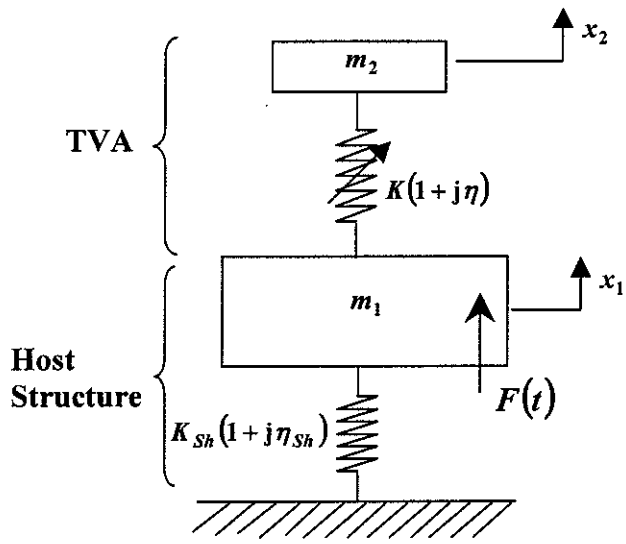

Figure 4.27:
Two degree of freedom model of TVA-shaker combination

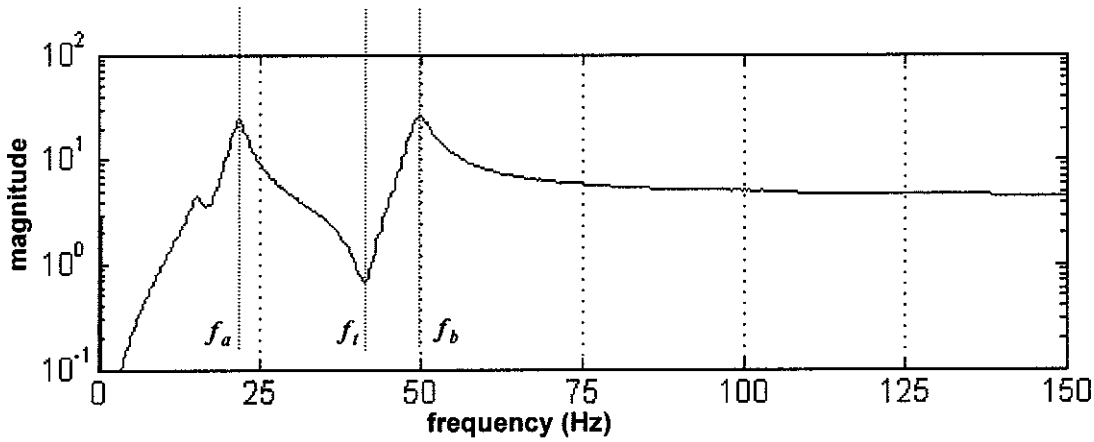

Figure 4.28: Frequency response function $A_{a_1 I_{Sh}}$ relating $a_1(t)$ to shaker current $I_{Sh}(t)$

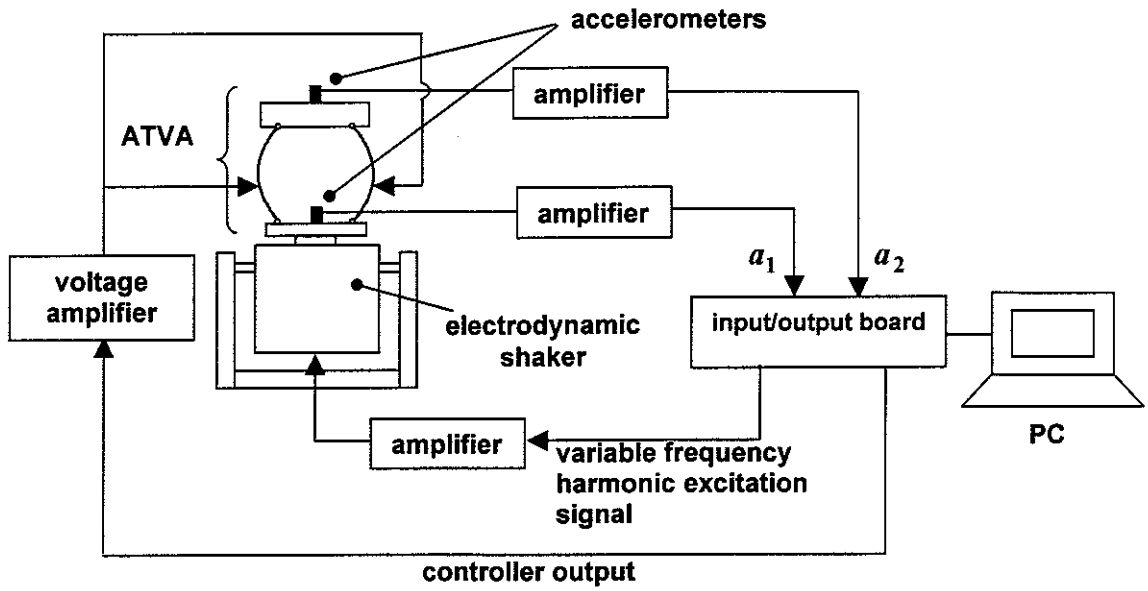

Figure 4.29: Experimental set-up of vibration control tests

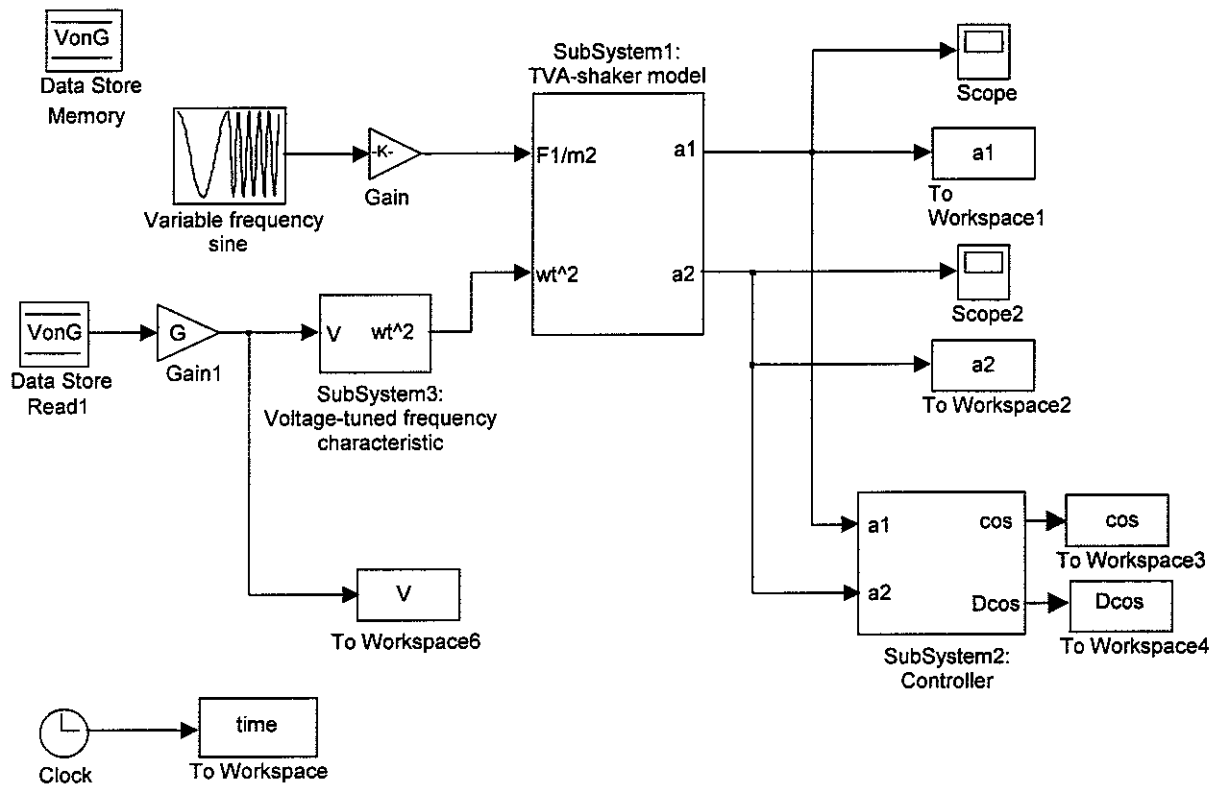

Figure 4.30(a): SIMULINK® model for simulated vibration control tests: overall system

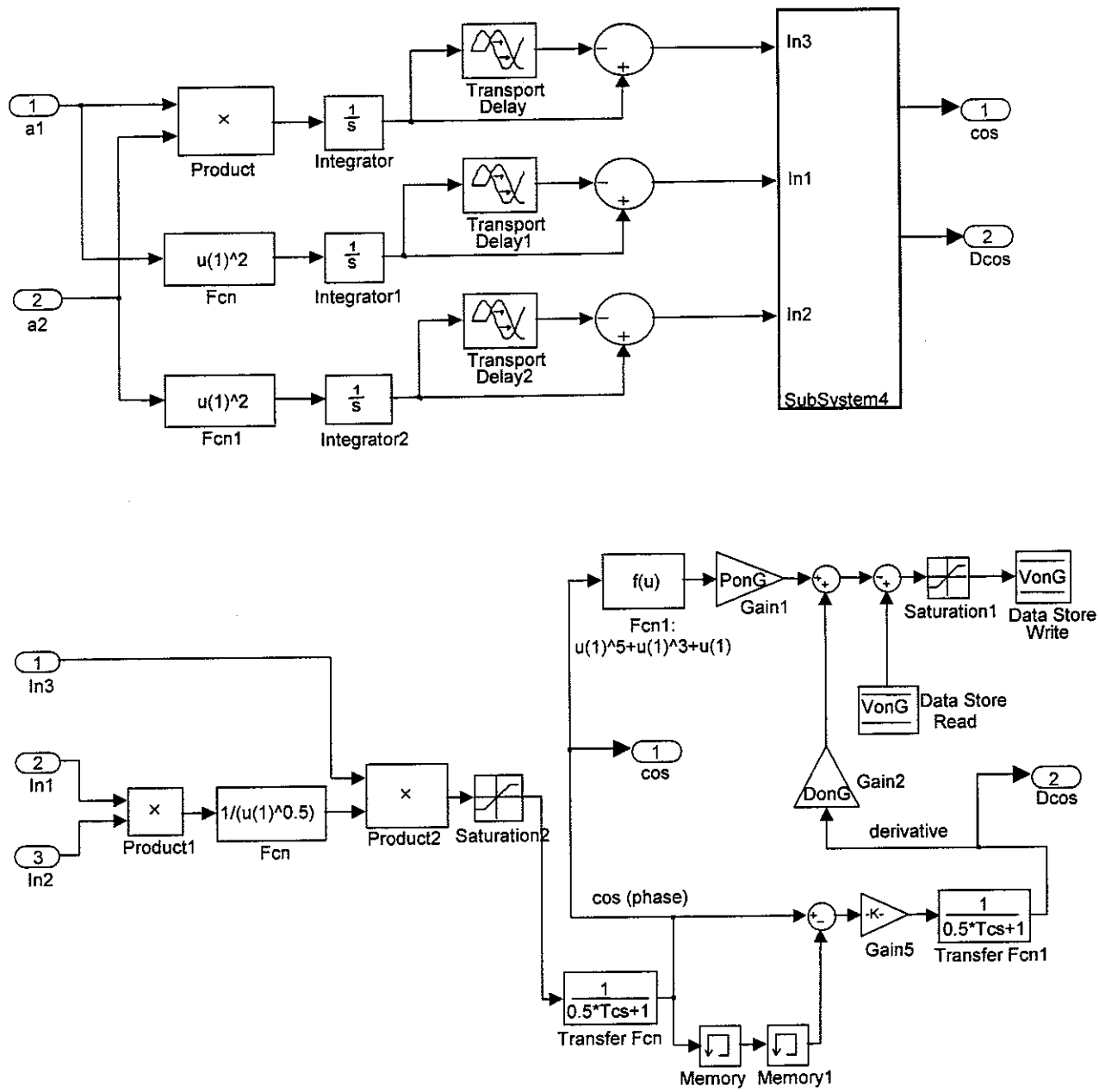

Figure 4.30(b): SIMULINK® model for simulated vibration control tests: controller

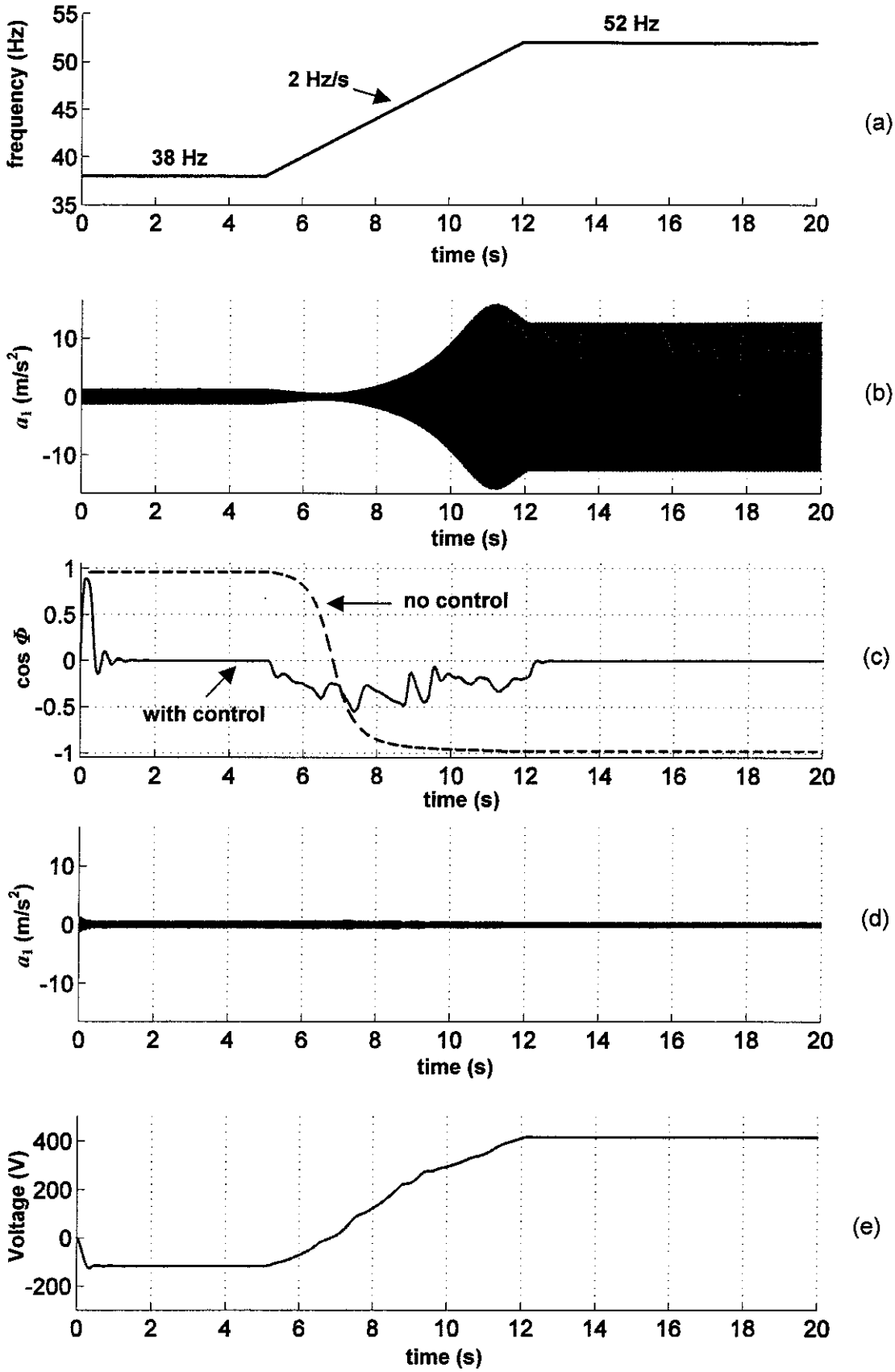

Figure 4.31: Predicted results for variable frequency harmonic excitation ((a) frequency variation; (b) vibration a_1 without control, piezos at 0 V; (c) cosine of ϕ; (d) controlled vibration a_1; (e) variation of controlled voltage applied to piezos; for control results $P = 4\times10^{-2}$, $D = 2\times10^{-3}$)

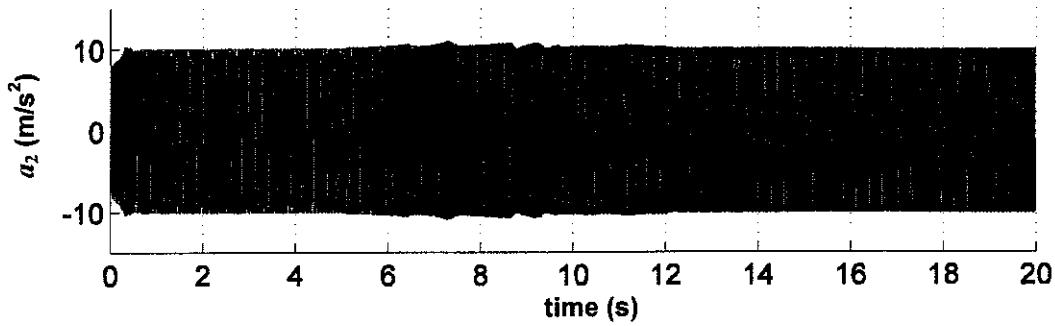

(f)

Figure 4.31 (cont'd): (f) absorber mass vibration a_2 for controlled a_1

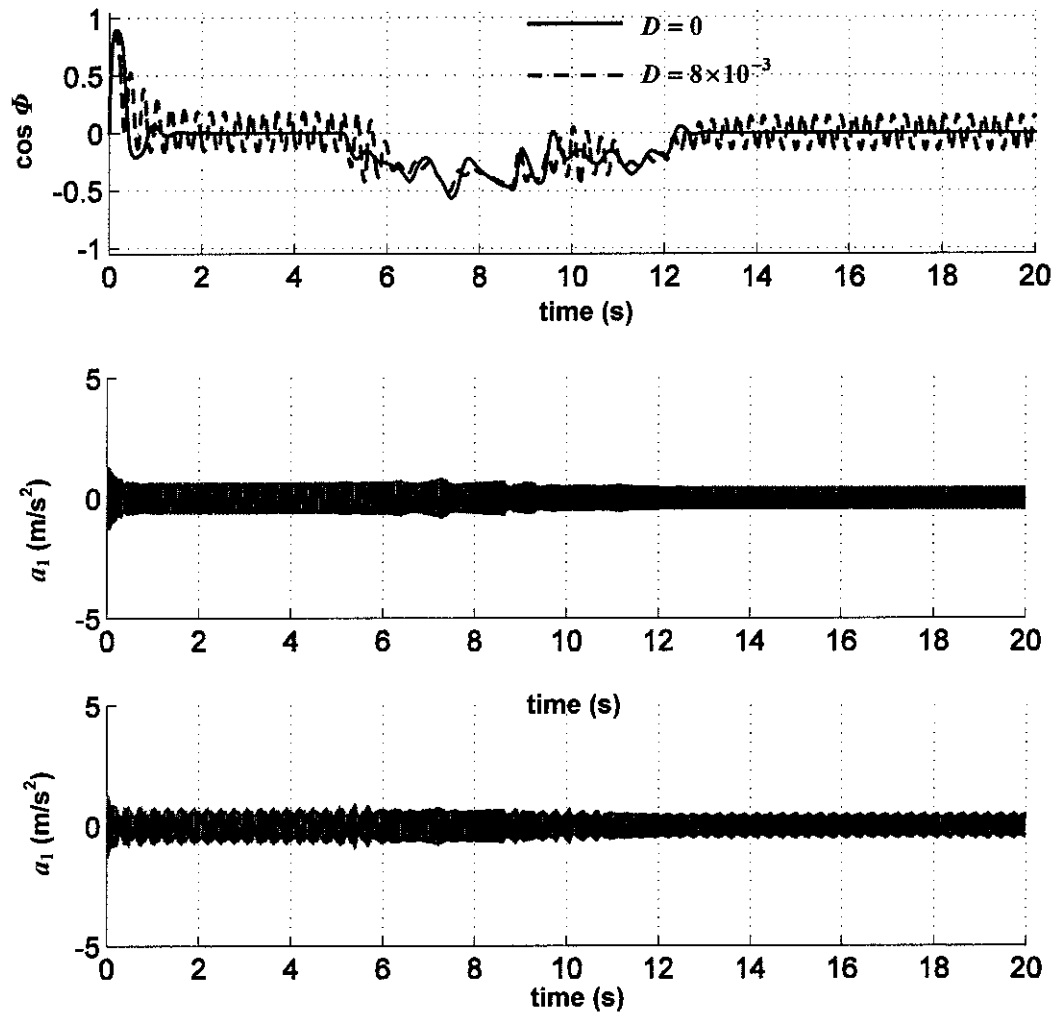

(a)

(b)

(c)

Figure 4.32: Effect of derivative term on predicted controlled vibration results for $P = 4\times10^{-2}$ (forcing frequency variation as in Figure 4.29(a)): (a) cosine of ϕ; (b) controlled vibration a_1 ($D = 0$); (c) controlled vibration a_1 ($D = 8\times10^{-3}$)

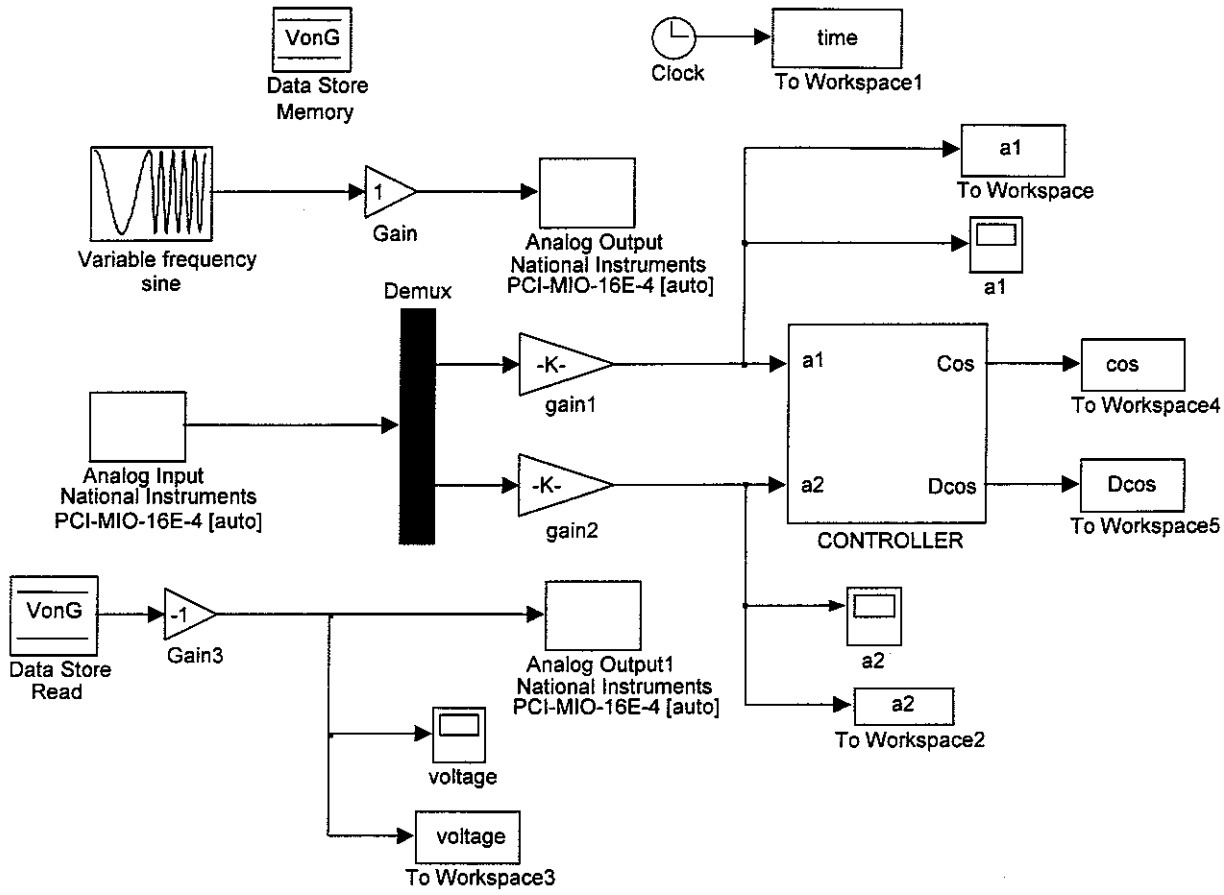

Figure 4.33: SIMULINK® model for experimental vibration control tests (controller as in Figure 4.30(b)

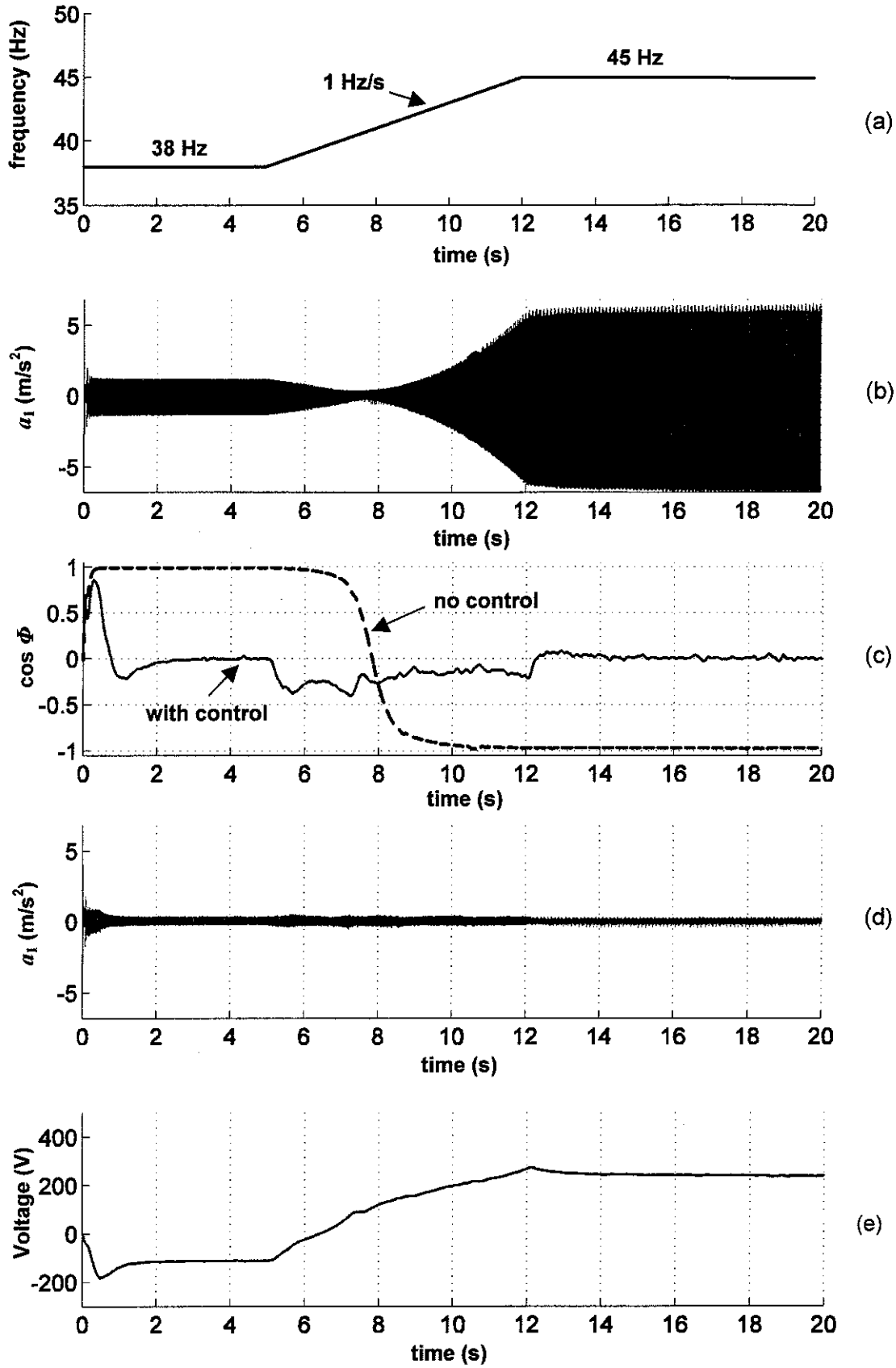

Figure 4.34: Experimental results for variable frequency harmonic excitation ((a) frequency variation; (b) vibration a_1 without control, piezos at 0 V; (c) cosine of ϕ; (d) controlled vibration a_1; (e) variation of controlled voltage applied to piezos; for control results $P = 4\times10^{-2}$, $D = 8\times10^{-3}$)

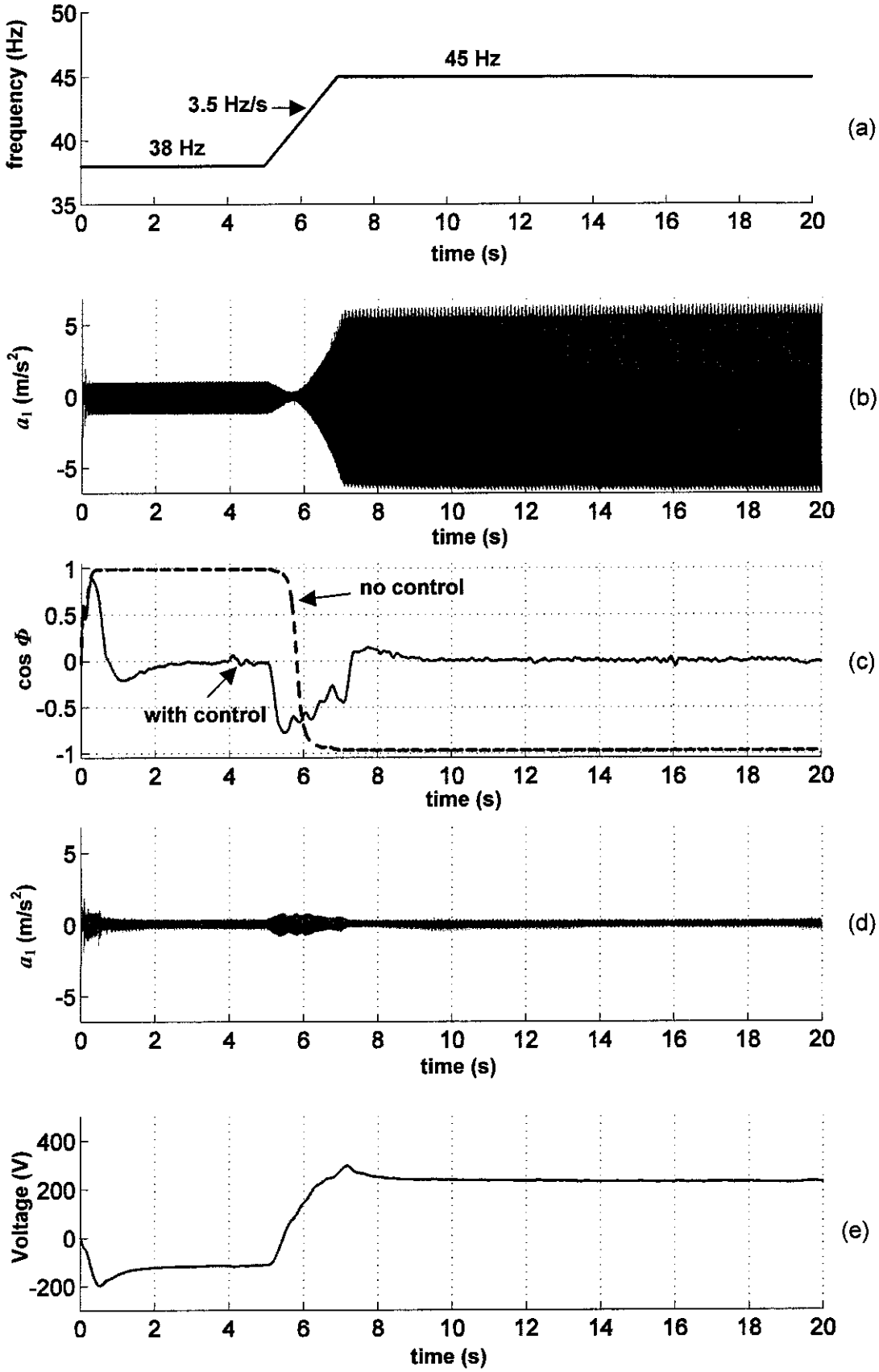

Figure 4.35: Experimental results for variable frequency harmonic excitation ((a) frequency variation; (b) vibration a_1 without control, piezos at 0 V; (c) cosine of ϕ; (d) controlled vibration a_1; (e) variation of controlled voltage applied to piezos; for control results $P = 4\times10^{-2}$, $D = 2\times10^{-3}$)

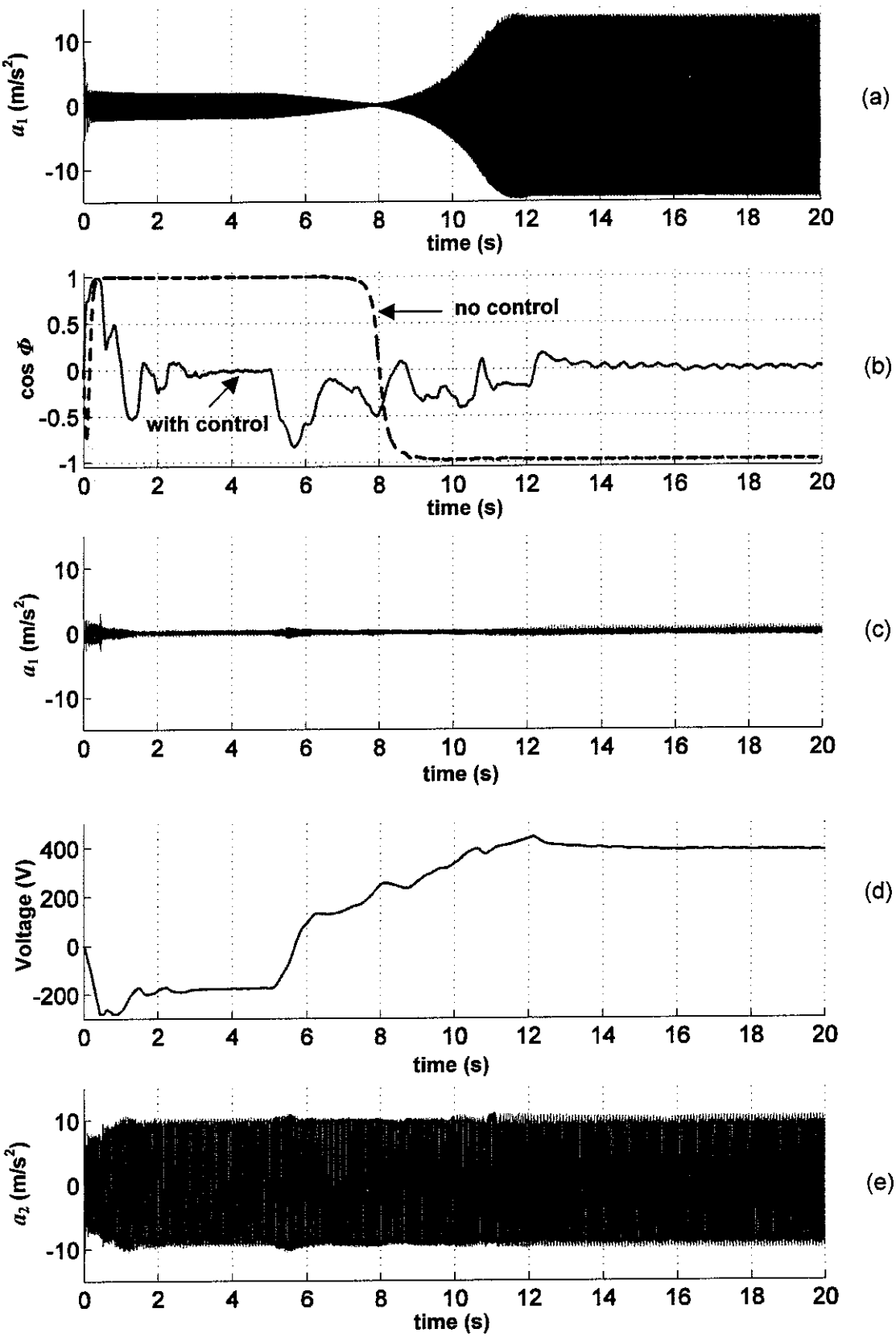

Figure 4.36: Experimental results for variable frequency harmonic excitation, frequency variation as in Figure 4.31(a): (a) vibration a_1 without control, piezos at 0 V; (b) cosine of ϕ; (c) controlled vibration a_1; (d) variation of controlled voltage applied to piezos; (e) absorber mass vibration a_2 for controlled a_1; for control results $P = 4\times10^{-2}$, $D = 2\times10^{-3}$)

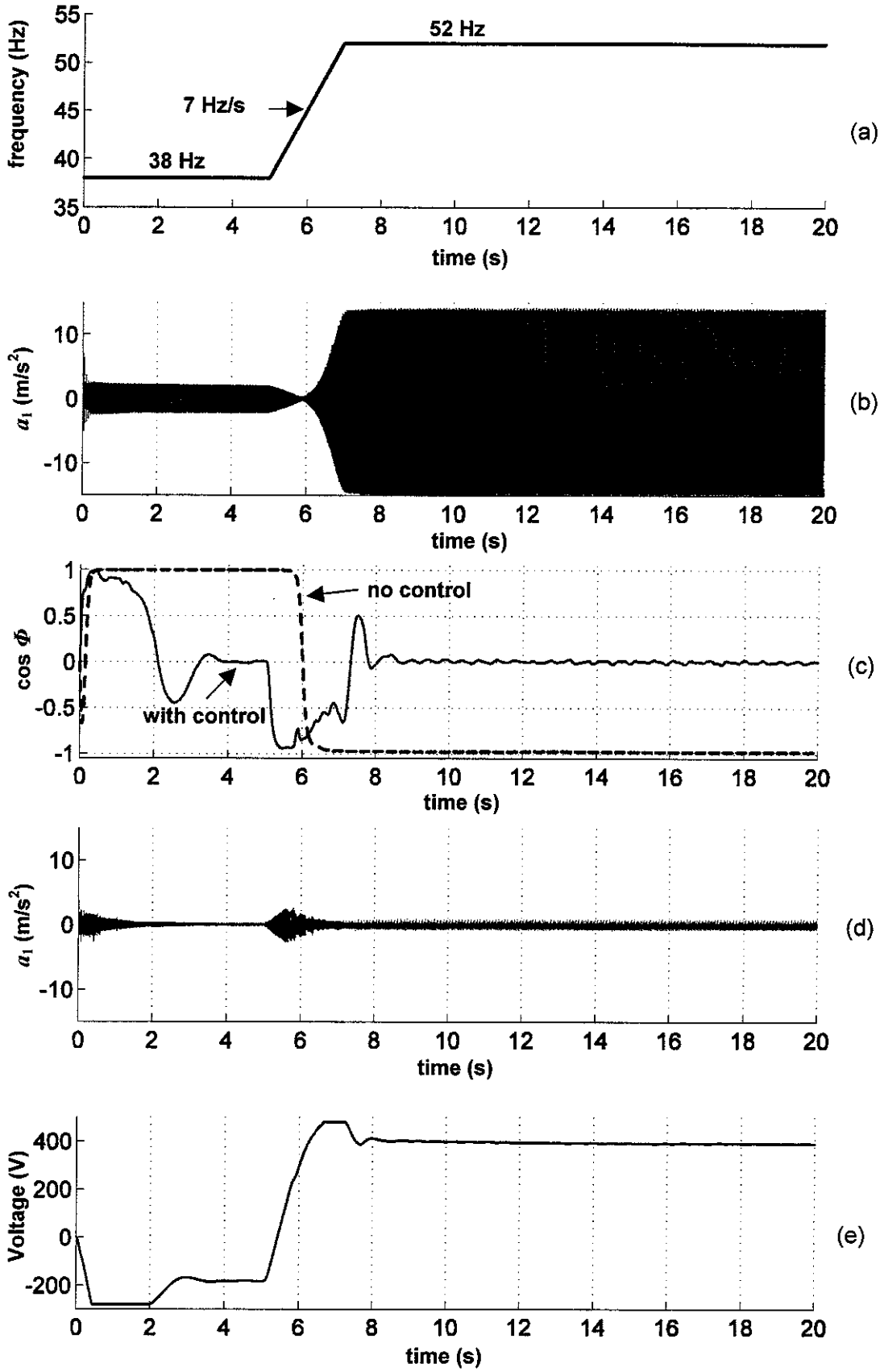

Figure 4.37: Experimental results for variable frequency harmonic excitation ((a) frequency variation; (b) vibration a_1 without control, piezos at 0 V; (c) cosine of ϕ; (d) controlled vibration a_1; (e) variation of controlled voltage applied to piezos; for control results $P = 4\times10^{-2}$, $D = 2\times10^{-3}$)

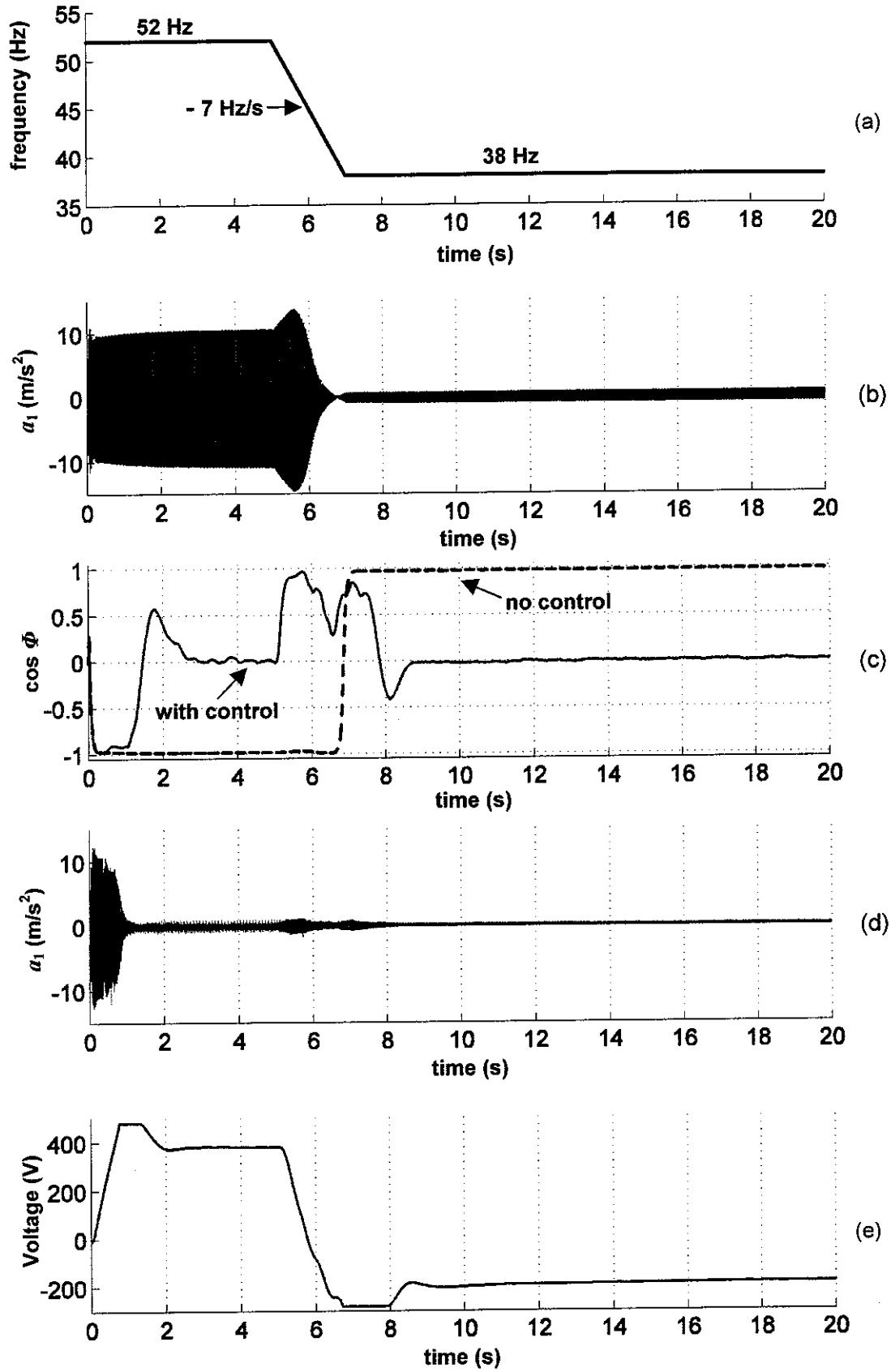

Figure 4.38: Experimental results for variable frequency harmonic excitation ((a) frequency variation; (b) vibration a_1 without control, piezos at 0 V; (c) cosine of ϕ; (d) controlled vibration a_1; (e) variation of controlled voltage applied to piezos; for control results $P = 4\times10^{-2}$, $D = 2\times10^{-3}$)

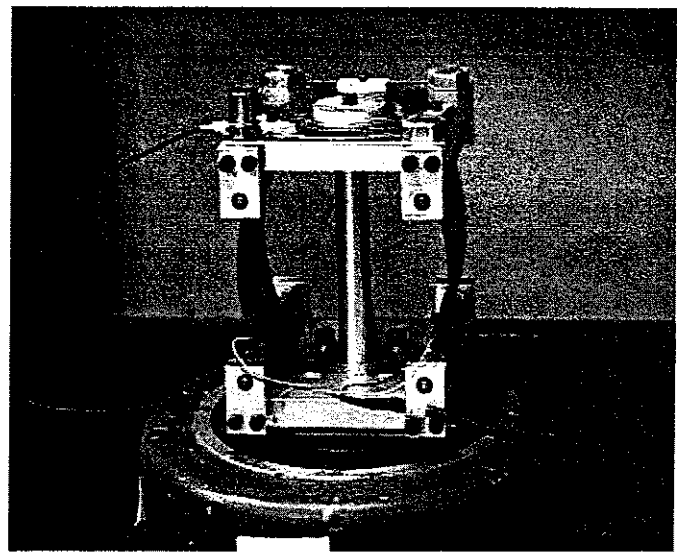

Figure 4.39: Modified prototype with linear bearing in Figure 4.21 replaced by flat spring

5 CONCLUSIONS AND FUTURE RESEARCH

This report presented research into novel methods of achieving variable stiffness in an adaptive tuned vibration absorber (ATVA) by changing shape. Following a brief outline on the basic theory of the ATVA, a study on the feasibility of the shape change concept was presented. This study concluded that considerable variation in the tuned frequency can be achieved by actuating a shape change, provided that this is within the limits of the actuator. A feasible design for such an ATVA is one in which the device offers low resistance to the required shape change actuation while not being restricted to low values of the effective stiffness of the vibration absorber. Hence, the best designs are those in which the actuator force is uncoupled as much as possible from the effective stiffness of the absorber. Three such original designs were identified: (i) A pinned-pinned arch beam with fixed profile of slight curvature and variable preload through an adjustable natural curvature; (ii) A vibration absorber with a variable geometry linkage as stiffness element; (iii) A vibration absorber with a stiffness element formed from curved beams of adjustable curvature in parallel vibrating longitudinally. The latter two designs were considered in greater detail in the subsequent two chapters, where the performances of a demonstrator and a prototype ATVA based on designs (ii) and (iii) respectively are analysed. Good correlation was achieved between theoretical and experimental results and reference is made to the specific conclusions of Chapters 3 and 4. The tests on the prototype ATVA with piezo-actuated parallel curved beams demonstrated the efficacy of this design in vibration control, particularly with respect to its agility in tracking rapidly varying forcing frequencies. The effectiveness of both designs tested was limited to frequencies for which inertia effects of the components forming the stiffness element were not significant.

As regards future research, three interesting projects would be: (a) To further enhance the performance of design (iii) above by reducing the damping either by design or actively, using the piezo-actuators; (b) To test a prototype for design (i); (c) to use techniques inspired by biomimetics to achieve curvature/shape change in the ATVA, as in the fluid-filled beam example of Figure 2.14.

REFERENCES

[1] A.H. von Flotow, A.H. Beard and D. Bailey, 'Adaptive tuned vibration absorbers: tuning laws, tracking agility, sizing and physical implementation', Proc. Noise-Con 94, 81-101. Florida (1994).

[2] M.R.F. Kidner and M.J. Brennan, 'Improving the performance of a vibration neutraliser by actively removing damping', J. Sound and Vibration 221(4) 587-606. (1999).

[3] M.J. Brennan, 'Vibration control using a tunable vibration neutraliser', Proceedings of the Institution of Mechanical Engineers Part C, 211 91-108. (1997).

[4] M.J. Brennan, 'Actuators for active control – tunable resonant devices', J. Applied Mech. and Eng. 5(1) 63-74. (2000).

[5] C.J. Longbottom, M.J. Day and E. Rider, 'A self tuning vibration absorber', UK Patent No. GB 218957B. (1990).

[6] M.A. Franchek, M.W. Ryan and R.J. Bernhard, 'Adaptive-passive vibration control', J. Sound and Vibration 189(5) 565-585. (1995).

[7] D.P. Hong and Y.S. Ryu, 'Automatically controlled vibration absorber', US Patent No. 4935651. (1985).

[8] J.P. Carneal, F. Charette and C.R. Fuller, 'Minimization of sound radiation from a plate using adaptive tuned vibration absorbers', J. Sound and Vibration (in press).

[9] E. Rustighi, M.J. Brennan and B.R. Mace, 'Design of an adaptive vibration absorber using shape memory alloy', ISVR Technical Memorandum No. 920. (2003).

[10] M.R.F. Kidner and M.J. Brennan, 'Variable stiffness of a beam-like neutraliser under fuzzy logic control', Trans. of the ASME, J. Vibration and Acoustics 124 90-99. (2002).

[11] T. Long, M.J. Brennan and S.J. Elliott, 'Design of smart machinery installations to reduce transmitted vibrations by adaptive modifications of internal forces', Proceedings of the Institution of Mechanical Engineers Part I, 12 215-228. (1997).

[12] G.H. Ryder. Strength of Materials, 3rd ed, Basingstoke, Hants: Macmillan (1986).

[13] E. Reissner, 'Note on the problem of vibrations of slightly curved bars', Trans. of the ASME, J. Applied Mechanics, June 1954, 195-196.

[14] S.S. Rao. Mechanical Vibrations, 3rd ed, Wokingham: Addison-Wesley (1995).

[15] ANSYS, Inc. ANSYS® 8.1.

[16] R.M. Jones. Mechanics of Composite Materials, New York: Hemisphere (1975).

[17] J.F.V Vincent and G. Jeronimidis, 'The Mechanical Design of Fossil Plants', Biomechanics and Evolution, JMV Rayner and RJ Wootton Eds., 21-36. CUP (1991).

[18] A.V. Srinivasan and D. Michael McFarland. Smart Structures: Analysis and Design, Cambridge: Cambridge University Press (2001).

[19] M.J. Brennan, M.J. Day, S.J. Elliott and R.J. Pinnington, 'Piezoelectric actuators and sensors', IUTAM 94, 263-274 (1994).

[20] M.J. Brennan, S.J. Elliott, P. Bonello and J.F.V. Vincent, 'The "click" mechanism in dipteran flight: if it exists, then what effect does it have?', J. Theoretical Biology 224 205-213. (2003).

[21] L.N. Virgin and R.B. Davis, 'Vibration isolation using buckled struts', J. Sound and Vibration 260, 965-973. (2003).

[22] Z.P. Bazant and L. Cedolin. Stability of Structures: Elastic, Inelastic, Fracture and Damage Theories, New York: Oxford University Press (1991).

[23] S.D. Conte and C. De Boor. Elementary Numerical Analysis: An Algorithmic Approach, New York: McGraw-Hill Book Company (1972).

[24] K.B. Blair, C.M. Krousgrill and T.N. Farris, 'Harmonic balance and continuation techniques in the dynamic analysis of Duffing's equation', J. Sound and Vibration 202(5), 717-731. (1997).

[25] W. Flügge. Stresses in Shells, Berlin: Springer (1973).

[26] R. D. Blevins. Formulas for Natural Frequency and Mode Shape, Malabar, Florida: R.E. Krieger (1984).

[27] THUNDER® Data Sheet for model TH 7-R. Face International Corporation, Norfolk, VA USA (1998).

APPENDIX 1: Derivation of eq. (2.13)

With reference to Figure 2.4:

$$(\delta s)^2 = (\delta\xi + \delta x)^2 + (\delta w)^2, \quad (\delta s_{P_0})^2 = (\delta x)^2 + (\delta w_{P_0})^2 \qquad \text{(A1.1a,b)}$$

ξ and $v = w - w_{P_0}$ are the dynamic displacements in the x and w directions respectively of a point from its position on the preloaded profile (Figure 2.4(c)). From eqs. (A1), neglecting $(\xi')^2$, it can be shown that the dynamic strain at the mid-surface is:

$$(\delta s - \delta s_{P_0})/\delta x \approx \xi' + (1/2)\{(w')^2 - (w'_{P_0})^2\} \qquad \text{(A1.2)}$$

where $(\,)' = d(\,)/dx$. Substituting $v = w - w_{P_0}$ in eq. (A1.2) and assuming $v' << w'_{P_0}$, the dynamic strain is approximately given by:

$$(\delta s - \delta s_{P_0})/\delta x \approx \xi' + w'_{P_0} v' \qquad \text{(A1.3)}$$

The equations of motion of an element of the beam of mass per unit length γ can be written as

$$N' = \gamma\ddot{\xi}, \qquad \gamma\ddot{v} = -M'' + (w'N)' \qquad \text{(A1.4a,b)}$$

where M is the bending moment and N is the instantaneous axial load (tensile positive). By substituting the expression for M [12]:

$$M = EI(w - w_i)'' \qquad \text{(A1.5)}$$

eq. (A1.4b) becomes

$$\gamma\ddot{v} = -EI(w - w_i)^{iv} + (w'N)' \qquad \text{(A1.6)}$$

By substituting $w = v + w_{P_0}$ and $N = N_d - P_0$ and noting that, for static equilibrium:

$$0 = -EI(w_{P_0} - w_i)^{iv} - w''_{P_0} P_0 \qquad \text{(A1.7)}$$

eq. (A1.6) becomes:

$$\gamma\ddot{v} = -EIv^{iv} - v''P_0 + \{(w_{P_0} + v)' N_d\}' \qquad \text{(A1.8)}$$

where N_d is the dynamic tensile load. Since $v' << w'_{P_0}$, eq. (A1.8) reduces to

$$EIv^{iv} + v''P_0 - \{w'_{P_0} N_d\}' + \gamma\ddot{v} = 0 \qquad \text{(A1.9)}$$

Neglecting the longitudinal inertia effect (i.e. $\ddot{\xi} << \ddot{v}$), the integration of eq. (A1.4a) yields a uniform dynamic load (independent of position), N_{d0}:

$$N' = N'_d = 0 \;\Rightarrow\; N_d = N_{d0} \qquad \text{(A1.10)}$$

Hence, from eq. (A1.3)

$$N_{d0}/(EA) = \xi' + w'_{P_0} v' \tag{A1.11}$$

Integrating eq. (A1.11), noting that, for symmetry about the mid-section, $\xi(0,t) = -\xi(L,t)$ and $N_{d0} = K_S \xi(0,t)$, eq. (A1.11) yields:

$$N_{d0} = \frac{\int_0^L w'_{P_0} v' \, dx}{2\{1/(2K_B) + 1/K_S\}} \tag{A1.12}$$

where $K_B = EA/L$. Substituting for $N_d = N_{d0}$ from eq. (A1.12) into eq. (A1.9) yields the required equation of motion, eq. (2.13).

APPENDIX 2: Derivation of eqs. (2.27)

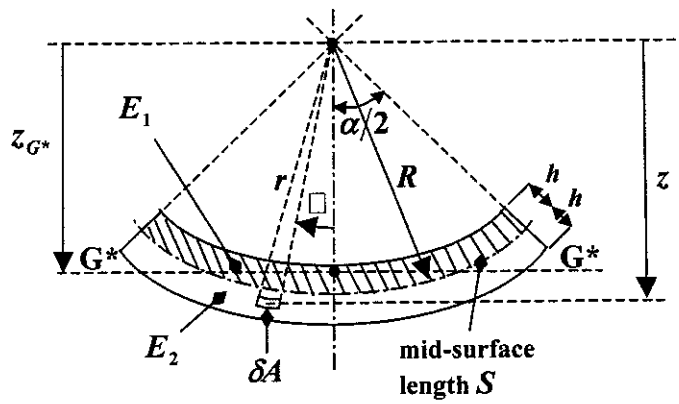

Figure A2.1: Composite curved section

With reference to Figure A2.1, using the theory of composites [16], the position of the neutral surface of the composite beam is given by:

$$z_{G^*} = \frac{\sum_1 z\delta A + C\sum_2 z\delta A}{\sum_1 \delta A + C\sum_2 \delta A} \tag{A2.1}$$

where the suffixes 1 and 2 refer to the individual layers of cross-sectional areas $A_1 = \sum_1 \delta A$, $A_2 = \sum_2 \delta A$ respectively and $C = E_2/E_1$. Now

$$z = r\cos\theta, \quad \delta A = r\delta\theta\delta r \tag{A2.2a,b}$$

Hence:

$$\sum_1 \delta A = \int_{R-h}^{R} \int_{-\alpha/2}^{\alpha/2} r\,d\theta\,dr = \alpha(R - h/2)h, \quad \sum_2 \delta A = \int_{R}^{R+h} \int_{-\alpha/2}^{\alpha/2} r\,d\theta\,dr = \alpha(R + h/2)h \tag{A2.3a,b}$$

and

$$\sum_1 z\delta A = \int_{R-h}^{R}\int_{-\alpha/2}^{\alpha/2} r^2\cos\theta\, dr d\theta\,, \quad \sum_2 z\delta A = \int_{R}^{R+h}\int_{-\alpha/2}^{\alpha/2} r^2\cos\theta\, dr d\theta \tag{A2.4a,b}$$

Substituting eqs. (A2.3) and (A2.4) in eq. (A2.1) and integrating, yields:

$$z_{G^*} = (4/3)(1/\alpha)\left[(3R^2 + h^2 - 3DRh)/(2R - Dh)\right]\sin(\alpha/2) \tag{A2.5}$$

where $D = (1-C)/(1+C)$. Now

$$(I_{G^*G^*})_i = \sum_i (z - z_{G^*})^2\,\delta A \tag{A2.6}$$

where $i = 1, 2$. Hence,

$$(I_{G^*G^*})_1 = \int_{R-h}^{R}\int_{-\alpha/2}^{\alpha/2} r(r\cos\theta - z_{G^*})^2\, dr d\theta\,, \quad (I_{G^*G^*})_2 = \int_{R}^{R+h}\int_{-\alpha/2}^{\alpha/2} r(r\cos\theta - z_{G^*})^2\, dr d\theta \tag{A2.7a,b}$$

Substituting for z_{G^*} from eq. (A2.5) into eqs. (A2.7), integrating, and substituting $R = S/\alpha$ yields the expressions in eqs. (2.27).

APPENDIX 3: Derivation of eq. (4.1)

If U is the strain energy due to deformation, Castigliano's theorem states that:

$$u = \frac{\partial U}{\partial P}$$

Now

$$U = \int_{-\alpha/2}^{\alpha/2} \frac{M^2}{2EI} R\, d\theta \text{ and } M = -PR\left(\cos\theta - \cos\frac{\alpha}{2}\right)$$

where R is the radius of curvature and M is the bending moment. Hence,

$$u = \frac{R}{EI}\int_{-\alpha/2}^{\alpha/2} M\frac{\partial M}{\partial P}\, d\theta = \frac{PR^3}{EI}\int_{-\alpha/2}^{\alpha/2}\left(\cos^2\theta - 2\cos\theta\cos\frac{\alpha}{2} + \cos^2\frac{\alpha}{2}\right) d\theta$$

Integrating, gives

$$K = \frac{P}{u} = \frac{EI}{R^3\{2\alpha - 3\sin\alpha + \alpha\cos\alpha\}}$$

Substituting, $R = S/\alpha$, $P_E = \pi^2\, EI/S^2$ in above equation and using eq. (4.2), gives the expression for $\tilde{K}$ in eq. (4.1).

APPENDIX 4: Derivation of eqs. (4.7a,b)

With reference to Figure 4.2, if M is the bending moment, R_i is the initial radius of curvature and R is the deformed radius of curvature, then from [12]:

$$M = EI(1/R - 1/R_i) \tag{A4.1}$$

Since $1/R = d\theta/ds = \theta'$:

$$M = EI(\theta' - 1/R_i) \tag{A4.2}$$

Since beam is initially in the shape of a circular arc, R_i is not a function of s. Now $M = -Pw$ and $w' = \sin\theta$, hence, by differentiating eq.(A4.2) with respect to s:

$$EI\theta'' = -P\sin\theta \tag{A4.3}$$

From eq. (A4.3) it can be deduced that [22]:

$$[EI/(4P)](\theta')^2 = -\sin^2(\theta/2) + C \tag{A4.4}$$

where C is an integration constant. Noting that $\tilde{P} = P/P_E$ and $P_E = \pi^2 EI/S^2$, eq. (A4.4) is rewritten as:

$$[S^2/(4\pi^2\tilde{P})](\theta')^2 = -\sin^2(\theta/2) + C \tag{A4.5}$$

At $s = 0$, $\theta = \theta_0$ and $M = 0$, hence, from eq. (A4.2):

$$\theta'|_{s=0} = 1/R_i = \alpha/S \tag{A4.6}$$

Substituting in eq. (A4.5) at $s = 0$ yields:

$$C = \alpha^2/(4\pi^2\tilde{P}) + \sin^2(\theta_0/2) \tag{A4.7}$$

Hence, substituting in eq. (A4.5):

$$[S^2/(4\pi^2\tilde{P})](\theta')^2 = \alpha^2/(4\pi^2\tilde{P}) + \sin^2(\theta_0/2) - \sin^2(\theta/2) \tag{A4.8}$$

Assuming $P > 0$, taking the square root of both sides of eq. (A4.8) and integrating, yields

$$-\int_{\theta_0}^{0} \frac{d\theta}{\sqrt{\{\alpha^2/(4\pi^2\tilde{P}) + \sin^2(\theta_0/2) - \sin^2(\theta/2)\}}} = \frac{2\pi}{S}\int_0^{S/2} \tilde{P}^{\frac{1}{2}} ds \tag{A4.9}$$

which yields eq. (4.7a) upon integration. If both sides of eq. (A4.9) are multiplied by $1 + \cos\theta$ under the integral sign and the resulting equation integrated, then the following equation results:

$$\int_0^{\theta_0} \frac{2\cos^2(\theta/2)}{\sqrt{\{\alpha^2/(4\pi^2\tilde{P}) + \sin^2(\theta_0/2) - \sin^2(\theta/2)\}}} d\theta = \pi\tilde{P}^{\frac{1}{2}} + \pi\tilde{P}^{\frac{1}{2}}(l/S) \tag{A4.10}$$

where l is defined in Figure 4.2(b). Now

$$\tilde{u} = u/S = L/S - l/S \tag{A4.11}$$

Noting that L/S is given by eq. (4.14), one obtains from eqs. (A4.11) and (A4.10) the expression for $\tilde{u}$ in eq. (4.7b).

For $P < 0$, multiply both sides of eq. (A4.8) by -1 before taking the square root and proceed as above.

APPENDIX 5: Estimation of angle-voltage characteristic of piezo-actuators

The THUNDER® TH -7R piezo-actuator has the geometry and end conditions shown in Figure 4.2(a). The data in Figure A5.1 refer to peak-to-peak displacement produced at the crown due to a 1 Hz unbiased ac voltage [27]. For these experiments, $S = 73\times10^{-3}$ m and, at zero applied voltage, $H = H_0 = 5.3\times10^{-3}$ m.

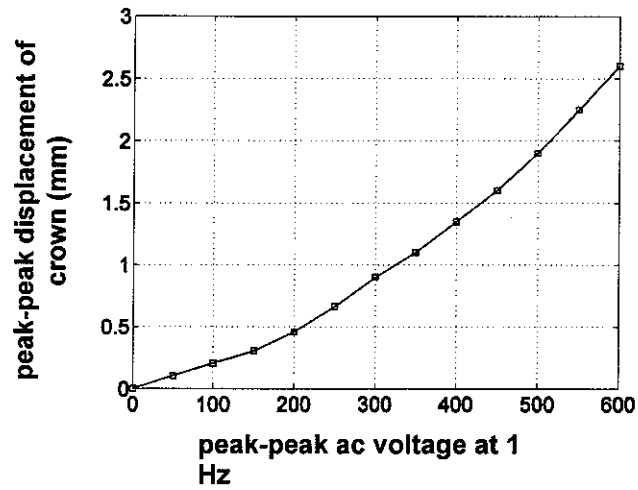

Figure A5.1: Experimental voltage-displacement characteristic of Thunder TH -7R [27]

Assuming, the displacement was symmetrical about the zero voltage position, the extreme values of H are $H = H_0 \pm \Delta H$, where the values of ΔH are half the peak-to-peak displacements. The negative sign applies for the positive voltage peak and the positive sign for the negative voltage peak [27]. Since S is fixed, the value of α corresponding to each such value of H could be found by solving the equation:

$$\{1-\cos(\alpha/2)\}/\alpha - H/S = 0 \qquad \text{(A5.1)}$$

(from eq. (4.5)). By expanding the cosine function in eq. (A5.1) in a power series, an initial approximation to the root of eq. (A5.1) was given by the only real root of the cubic equation:

$$(1/384)\alpha^3 + (1/8)\alpha - H/S \approx 0 \qquad \text{(A5.2)}$$

The resulting variation of α with negative and positive voltage peaks at 1 Hz was taken to be the same as the required variation of α with negative and positive dc voltage. In the prototype shown

in Figure 4.21, the location of the end pivots of the piezo-actuators was such that the relevant value of S was 83 mm rather than 73 mm. Hence, the α estimates obtained above were increased by a factor of 83/73. The final angle-voltage characteristic is shown in Figure 4.22.

APPENDIX 6: Estimation of parameters of shaker armature suspension

The method used for the determination of the natural frequency and damping of the shaker suspension assumes that the tuned frequency and damping loss factor of the TVA stiffness element, ω_t and η, respectively have been determined from the transmissibility measurement. With reference to Figure 4.27, using elementary analysis, the two undamped natural frequencies of the system (shown in Figure 4.26) are given by:

$$\omega_a^2, \omega_b^2 = \frac{1}{2}\left\{\omega_{Sh}^2 + (1+\mu)\omega_t^2\right\} \pm \frac{1}{2}\sqrt{\left\{\omega_{Sh}^2 + (1+\mu)\omega_t^2\right\}^2 - 4\omega_{Sh}^2\omega_t^2} \qquad \text{(A6.1a,b)}$$

From eqs. (A6.1):

$$\omega_{Sh}^2 = \left\{\left(\omega_a^2 + \omega_b^2\right)^2 - \left(\omega_a^2 - \omega_b^2\right)^2\right\}\Big/\left(4\omega_t^2\right), \qquad \mu = \left(\omega_a^2 + \omega_b^2 - \omega_{Sh}^2\right)\Big/\omega_t^2 - 1 \qquad \text{(A6.2a,b)}$$

Hence, knowing ω_t, the parameters ω_{Sh} and μ can be determined. For harmonic excitation $F(t) = \mathrm{Re}\left(\underline{F}\mathrm{e}^{\mathrm{j}\omega t}\right)$, $a_1(t) = \mathrm{Re}\left(\underline{a}_1\mathrm{e}^{\mathrm{j}\omega t}\right)$, it can be shown that

$$\eta_{Sh} = \left\{R - \frac{U_1}{U_2}\right\}\frac{U_2}{\omega_{Sh}^2} \qquad \text{(A6.3)}$$

where:

$$R = \mathrm{Im}\left\{\frac{\underline{F}}{\underline{a}_1 m_1}\right\}\Big/\mathrm{Re}\left\{\frac{\underline{F}}{\underline{a}_1 m_1}\right\} \qquad \text{(A6.4)}$$

$$U_1 = \frac{\mu\omega_t^6\left(\eta - \eta^3\right) - 2\mu\omega_t^4\eta\left(\omega_t^2 - \omega^2\right)}{\left(\omega_t^2 - \omega^2\right)^2 + \omega_t^4\eta^2} + \mu\omega_t^2\eta \qquad \text{(A6.5a)}$$

$$U_2 = -\omega^2 + \mu\omega_t^2 + \omega_{Sh}^2 - \left\{\frac{2\mu\omega_t^6\eta^2 + \mu\omega_t^4\left(\omega_t^2 - \omega^2\right)\left(1-\eta^2\right)}{\left(\omega_t^2 - \omega^2\right)^2 + \omega_t^4\eta^2}\right\} \qquad \text{(A6.5b)}$$

The excitation force $F(t)$ was proportional to the current supplied to the shaker, $I_{Sh}(t)$. Hence, if $A_{a_1 I_{Sh}}$ is the frequency response function relating $a_1(t)$ to $I_{Sh}(t)$ (Figure 4.26):

$$R = \frac{\mathrm{Im}\left(A^{-1}_{a_1 I_{Sh}}\right)}{\mathrm{Re}\left(A^{-1}_{a_1 I_{Sh}}\right)} \tag{A6.6}$$

Hence, the shaker suspension damping η_{Sh} can be determined as a function of frequency from eq. (A6.3) using the measurement of R (eq. A6.6) and the known estimates of ω_{Sh} and U_1, U_2 (eqs. (A6.5)). Alternatively, the value of η_{Sh} that gives best fit over the frequency range can be found. From eq. (A6.3):

$$R = \frac{U_1 + \omega_{Sh}^2 \eta_{Sh}}{U_2} \tag{A6.7}$$

Figure A6.1 compares the measured R (eq. A6.6) with that estimated from eq. (A6.7) using three different constant values of η_{Sh}. It is seen that a value of $\eta_{Sh} = 0.1$ gives the best fit.

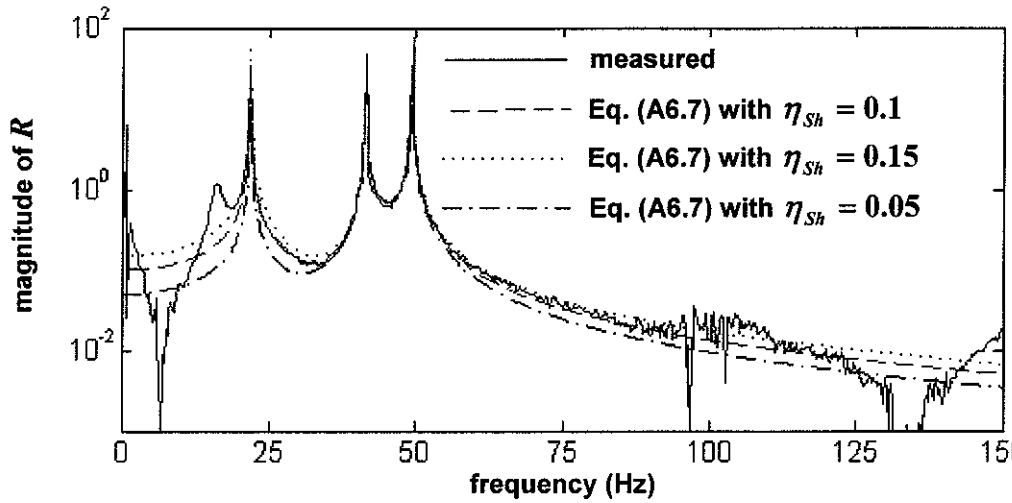

Figure A6.1: The ratio R

APPENDIX 7: List of instrumentation used in experiments.

The instrumentation details are given in Tables A7.1, A7.2.

instrument	make	serial number
spectrum analyser	Hewlett Packard 35650	2911A02485
shaker	Derriton Vibrator® Type VP4	325
power amplifier	AVL Instrumentation, Model 790A01	202
voltage amplifier for piezo-actuators	PI , E-507 HVPZT Amplifier	N/A
accelerometer 1	Bruel & Kjaer, type 4383	1230366
charge amplifier 1	Bruel & Kjaer, type 2635	1690255
accelerometer 2	Bruel & Kjaer, type 4383	1230368
charge amplifier 2	Bruel & Kjaer, type 2635	1690271

Table A7.1: List of instrumentation for transmissibility tests (sections 3.2, 4.4.1)

instrument	make	serial number
data acquisition system	National Instruments PCI-MIO-16E-4 multi-function I/O and NI-DAQ board with BNC-2110 connector block	N/A
shaker	Derriton Vibrator® Type VP4	325
power amplifier	AVL Instrumentation, Model 790A01	202
voltage amplifier for piezo-actuators	PI , E-507 HVPZT Amplifier	N/A
accelerometer 1	Bruel & Kjaer, type 4383	1230366
charge amplifier 1	Bruel & Kjaer, type 2635	1690255
accelerometer 2	Bruel & Kjaer, type 4383	1230368
charge amplifier 2	Bruel & Kjaer, type 2635	1690271

Table A7.2: List of instrumentation for vibration control tests (section 4.4.2)